



Scuola Dottorale di Ingegneria
Sezione di Ingegneria dell'Elettronica Biomedica,
dell'Elettromagnetismo e delle Telecomunicazioni
XXVIII ciclo

Next Generation Optical High-Speed Network

Tesi sottomessa
all'Università degli studi Roma Tre
per il conseguimento del titolo
DOTTORE DI RICERCA
Giugno 2016

Dottorando: Julian Hoxha

Docente Guida: Prof. Gabriella Cincotti

Coordinatore: Prof. Alessandro Salvini

To my father

ABSTRACT

The research ‘*Next generation optical high speed networks*’ considers new paradigms for optical access and long-haul (1000 km and above) communications, to satisfy the increasing demand for capacity, spectral efficiency and quality of service in telecom networks. In long-haul transmissions, digital signal processing (DSP), with high-order modulation and coherent detection, has revolutionized optical systems, thanks to its effectiveness to digitally mitigate chromatic dispersion and polarization mode dispersion, with an increase in transmission length. However, the drastic increase in system complexity creates a severe challenges for real-time implementation, related also to limited bandwidth of digital to analog converters (DAC), high power consumption of electronic devices, massive use of hardware parallelization and pipeline, making the system intolerant to any feedback path. On the other hand, future access optical passive networks (PON) need to increase per-user bandwidth, evolving towards wavelength-division multiplexing (WDM) systems, with colourless (wavelength independent) low-cost transmitters at the user’s side, also allowing different operators to share the same infrastructure. For both core and access networks, orthogonal frequency division multiplexing (OFDM) is proposed to overcome the electronic bottleneck, reduce power consumption and increase the spectral efficiency, satisfying current large bandwidth requests.

During the three-year research work, within the EU ASTRON and the Italian ROAD-NGN projects, new optical network architectures, systems and subsystems have been proposed and their performances have been analytically, numerically and experimentally evaluated.

In particular, new digital OFDM systems for unbundling the local loop (ULL) in access networks have been investigated for ultra-high speed PONs, along with

discrete multitoned (DMT) approaches, based on reflective semiconductor optical amplifier (RSOA).

All optical OFDM (AO-OFDM) systems have been experimentally tested during a 6-month staying at the National Institute of Information and Communications Technology (NICT) in Japan, using both coherent and direct detection receivers. The performance of two different optical devices, able to demultiplex the AO-OFDM signal, have been experimentally compared, without optical dispersion compensation or time gating.

For long haul transmissions, AO-OFDM can also reduce the power consumption in case of superchannels, with a high number of sub-channels. Analytically formula have been found for performance evaluation, in terms of maximum number of spans, frequency offset, phase noise and equalization enhancement phase noise (EENP), supported and validated by numerical simulation.

Finally, a novel transmission system is proposed, based on the digital fractional Fourier transform, to generate *sinc*-shaped time domain pulse at the receiver side, reducing the DSP complexity for real time implementation at high data rates.

SOMARIO

Il tema di ricerca ‘Reti ottiche di nuova generazione ad alta velocità’ considera nuovi paradigmi sia per l'accesso ottico che per le trasmissioni a lungo raggio (più di 1000 km), per soddisfare la crescente richiesta di capacità, efficienza spettrale e qualità del servizio nelle reti di telecomunicazione. Nelle trasmissioni a lungo raggio, il processamento del segnale nel dominio digitale, l'utilizzo delle modulazioni complesse e la rivelazione coerente, hanno rivoluzionato i sistemi ottici grazie alla loro efficacia di compensare digitalmente la dispersione cromatica e da polarizzazione, con un aumento della lunghezza di trasmissione. Tuttavia, il drastico aumento della complessità crea delle difficoltà per l'implementazione in tempo reale. Questo è dovuto alla banda limitata dei convertitori digitale analogico (DAC), ad un elevato consumo energetico dei dispositivi elettronici, a un uso massiccio di parallelizzazione hardware, rendendo il sistema intollerante a qualsiasi percorso di controreazione.

D'altra parte, le future rete d'accesso ottiche passive devono aumentare la velocità di cifra per utente, evolvendo verso sistemi di multiplexazione a divisione di lunghezza d'onda, utilizzando trasmettitori economici e indipendenti dalla lunghezza d'onda al lato dell'utente, consentendo anche ai diversi operatori di condividere la stessa infrastruttura.

Per entrambe le reti di trasporto e di accesso, la multiplexazione ortogonale a divisione di frequenza ortogonale (OFDM), permette di superare il ‘collo di bottiglia’ dovuto all'elettronica, ridurre il consumo energetico e aumentare l'efficienza spettrale, soddisfacendo le richieste di banda.

Durante il lavoro di ricerca di tre anni, nell'ambito dei progetti ROAD-NGN e ASTRON, sono state proposte nuove architetture, sistemi e sottosistemi in una rete ottica, valutando le loro prestazioni, analiticamente, numericamente e anche sperimentalmente.

In particolare, i nuovi sistemi OFDM digitali per la disaggregazione dell'ultimo tratto nelle reti di accesso sono stati accuratamente studiati ad alta velocità di cifra utilizzando la tecnica DMT e un amplificatore ottico a semiconduttore riflettente (RSOA).

I sistemi tutto-ottici OFDM (AO-OFDM) sono stati valutati sperimentalmente presso National Institute of Information and Communications Technology (NICT) in Giappone

utilizzando ricevitori coerenti e diretti. Sono state valutate sperimentalmente le prestazioni di due dispositivi ottici in grado di demoltiplicare il segnale AO-OFDM senza compensazione della dispersione ottica o campionando otticamente.

AO-OFDM può ridurre il consumo di energia nelle reti di trasporto utilizzando dei ‘Supercanali’ costituito da un elevato numero di sottoportanti. Sono state trovate formule analitiche per la valutazione delle prestazioni, in termini di numero massimo di span (1 span è lungo 80km di fibra), offset di frequenza, rumore di fase e rumore di fase originato dalla dispersione cromatica non-equalizzata. I risultati ottenuti sono stati validati da simulazioni numeriche.

Infine, è stato proposto un nuovo sistema di trasmissione multi-portante basato sulla trasformata frazionaria di Fourier digitale in grado di generare degli impulsi *sinc* nel tempo al lato ricevente sfruttando l’effetto della dispersione cromatica. La complessità degli algoritmi al lato ricevente è stato ridotto drasticamente rendendo così possibile l’implementazione in tempo reale del sistema a una velocità di cifra elevata.

TABLE OF CONTENTS

ABSTRACT.....	iii
SOMARIO	v
ACKNOWLEDGEMENTS.....	xi
LIST OF FIGURES	xiii
CHAPTER 1	1
EVOLUTION OF OPTICAL FIBER COMMUNICATION	1
1.1 Motivations	1
1.2 Evolution of optical transport networks.....	2
1.3 Evolution of optical access networks.....	5
1.4 High-speed single carrier and multicarrier transmission	6
1.4.1 Single carrier trasmission.....	7
1.4.2 Multicarrier transmission	8
1.5 Thesis outline and contributions	11
1.5.1 List of publications	13
References.....	15
CHAPTER 2	17
OPTICAL ACCESS NETWORKS BASED ON ELECTRICAL OFDM	17
2.1 Introduction.....	17
2.1.1 Electrical OFDM with optical modulation	18
2.1.1.1 IM/DD	18
2.1.1.2 CO detection	20

2.2	OFDM.....	20
2.3	Electrical OFDM for PONs	24
2.3.1	Unbundling the local loop.....	25
2.3.2	OFDM-PON based on IM/DD for ULL	26
2.3.3	Performance evaluation	29
2.4	Access networks based on RSOA.....	31
2.4.1	RSOA model.....	34
2.4.2	Bit and power loading.....	37
2.4.2.1	Water filling algorithm	39
2.4.2.2	Levin-Campello algorithm	41
2.4.3	RSOA characterization	42
2.4.4	Performance evaluation	46
2.5	Conclusions.....	50
	References.....	51
	CHAPTER 3	56
	ALL OPTICAL OFDM	56
3.1	Introduction.....	57
3.2	Principle of operation.....	58
3.2.1	Cyclic prefix in AO-OFDM setup	67
3.3	Direct detection.....	69
3.3.1	DPSK modulation	70
3.3.1.1	Simulation results for DPSK	72
3.3.2	DQSK modulation	75
3.3.2.1	Simulation results for DQPSK	76
3.4	Coherent detection	78

3.4.1	Coherent setup	78
3.4.1.1	Model with frequency offset and phase noise	80
3.4.1.2	Frequency offset due to AWG and TX comb.....	81
3.4.1.3	Phase noise and EEPN investigation	83
3.4.1.4	Joint FFCPE investigation	87
3.4.1.5	Bandwidth and sampling rate requirements	88
3.4.1.6	Frequency domain equalizer and power consumption estimation.....	89
3.4.1.7	Nonlinear performance	90
3.5	Experimental results	92
3.5.1	Flat optical comb generation.....	95
3.5.2	Experimental performance evaluation	101
3.5.3	Experimental comparison between FBG and an AWG	104
3.6	Conclusions.....	106
	References.....	108
	CHAPTER 4	112
	OFDM BASED ON THE FRACTIONAL FOURIER TRANSFORM	112
4.1	Continues fractional Fourier transform.....	113
4.2	FrFT and the time lens effect	117
4.3	Implementation of digital FrFT	121
4.4	Coherent optical communications based on PM-FrFT	126
4.4.1	System performance.....	133
4.5	Conclusions.....	141
	References.....	142
	CHAPTER 5	145
	CONCLUSION AND FUTURE WORK	145

5.1	Conclusions.....	145
5.2	Further work	146

ACKNOWLEDGEMENTS

I thank my supervisor Professor Gabriella Cincotti for giving me the opportunity to work on this thesis, for her generous help, valuable advice and for giving me the opportunity to work in international projects and participating in international conference. I also thank her for sending me at a prestigious research group in Japan for a six month research. I really felt privileged for all the support during this research work.

I am also grateful to Dr. Takahiro Kodama for long discussion on the future of optical communications and for being a very good friend.

I also thank Dr. Satoshi Shimizu for introducing me to the experimental laboratory ‘world’ and Dr. Naoya Wada for accepting me in NICT laboratory.

I thank the PhD student Tomotaka Nagashima, from Osaka University, for very interesting technical discussion on fractional Fourier transform and for helping me to finalize the Matlab code.

I thank the PhD student Jacopo Morosi, from Politecnico di Milano, for helping me to finalize the experimental results in NICT laboratory.

I wish to thank Giuseppe Zarra and Alessandro Impellizzeri for their support in Roma Tre laboratory and for their friendship.

I want to thank my dear old friends ‘Grupi Shurupi’: Ani, Lodi, Kozet, Jonka, Ola, Aida, Eno, Macoku, Bulls for their friendship. I also thank the engineering students at Roma Tre university, Eno, Marsel, Tili, Enzo, Marco, Jurgen, Artan, Rudi and Dorian² for the lunch time we spend together during this thesis work.

I would like to acknowledge my family for their support during the university study and for being an example for me. Their love always encouraged me to follow my dreams.

Last but not the least, I thank my wife Lorena, for her unconditional love and support during this thesis work.

LIST OF FIGURES

Figure 1-1: Cisco Global IP Traffic Forecast, 2014–2019 [1].....	1
Figure 1-2: Evolution of electronically multiplexed serial interface rates and WDM capacities [2]-[3].	2
Figure 1-3: Spectrum utilization for fixed and flexi grid [7].	4
Figure 1-4: Time (a) and frequency (b) behaviour of a RRC pulse with roll-off factor $\alpha=0.4$	7
Figure 1-5: (a) A polarization multiplexed quadrature modulated integrated transmitter, and (b) a dual polarization coherent receiver for single carrier [14]-[15].	7
Figure 1-6: Different multicarrier transmission setup [17].....	9
Figure 1-7: Potential 400G architectures in the state of the art. ¹ DAC and ADC characteristics taken either from Section 6 or from the state of the art. ² Distances reported either in the state of the art or from OIF contributions. ³ OIF2014.030.00, ⁴ OIF2015.030.01, ⁵ OIF2015.100.00, ⁶ OIF2015.037.01, ⁷ OIF2014.031.00 [9].....	11
Figure 2-1: Schematic of the access networks [1].	17
Figure 2-2: (a) Block diagram of IM/DD and (b) CO-OFDM using optical modulation [2].....	18
Figure 2-3: Optical OFDM with D.C bias and DD receiver [4].	19
Figure 2-4: Schematic of OFDM setup.....	21
Figure 2-5: Power spectral density of the OFDM signal.	22
Figure 2-6: Down-stream and up-stream scenario for PON based on OFDM [1].....	24
Figure 2-7: P2P OFDM-based system.	27
Figure 2-8: OFDM-based PON.....	28
Figure 2-9: (a) BER versus EVM in a back-to-back configuration, (b) BER versus optical power received after 40 km for a 4-ONU system.	30

Figure 2-10: (a) BER versus EVM for a 4-user PON, (b) BER versus received optical power for a 4-user PON.	30
Figure 2-11: Schematic diagram of an SOA.	32
Figure 2-12: DMT-PON proposed.	33
Figure 2-13: Achievable bit rate as a function of SNR (dB) for different value of the gap Γ	38
Figure 2-14: Optimal power allocation with water filling solution.	40
Figure 2-15: VPI-photonics circuit build for RSOA characterization.	42
Figure 2-16: VPI-Photonics RSOA parameter.	43
Figure 2-17: VPIPhotonic results. (a) Optical gain versus the input optical power with a fixed bias current of 40mA. (b) Output power versus the input optical power. (c) Optical gain versus the driving bias current for optical input power of -10 dBm. (d) Optical gain versus the bias current for an optical input power of 10 dBm.	44
Figure 2-18: Matlab results. (a) Optical gain versus the input optical power. (b) Optical gain versus the bias current.	45
Figure 2-19: RSOA frequency response.	45
Figure 2-20: VPIPhotonic up-stream simulated setup.	47
Figure 2-21: Measured optical spectrum.	48
Figure 2-22: (a) Number of bits versus the subcarrier index, (b) estimated SNR versus the subcarrier index.	48
Figure 2-23: (a) Capacity versus RSOA input power, (b) capacity versus fiber length for input RSOA power of -10dBm.	49
Figure 3-1: Architecture of an AO-OFDM system.	59
Figure 3-2: Optical IDFT operation.	60
Figure 3-3: Optical IDFT circuit.	61
Figure 3-4: AWG configuration for IDFT/DFT operation [7].	63
Figure 3-5: Power spectral distribution of three adjacent subcarriers with $N = 8$, $T = 40$ [ps] and $FSR = 200$ [GHz].	63
Figure 3-6: (a) Received signal at the matched port (b) and unmatched port.	65

Figure 3-7: . Complementary schemes of an AO-OFDM transmitter.	65
Figure 3-8: (a) and (b) OFDM symbol. (c) and (d) demultiplexed symbol. (e) and (f) after time gating. (a), (c) and (e) are obtained with the scheme of Figure 3-7(a) and (b), (d) and (f) with the scheme of Figure 3-7(b). (g) BER performance of the two schemes of Figure 3-7.	66
Figure 3-9: AO-OFDM setup with AWG modification to insert the CP [19].	67
Figure 3-10: Three subcarriers with CP = 0.1 and R = 12.5 [GHz].	68
Figure 3-11: Eye diagram with and without CP.	69
Figure 3-12: AO-OFDM based DPSK modulation setup.	70
Figure 3-13: MZM operation for DPSK modulation and signal constellation.	70
Figure 3-14: Differential encoder implementation.	71
Figure 3-15: Constructive (a) and destructive (b) spectra generation at the outputs of the DLI.	72
Figure 3-16: Power spectral distribution of AO-OFDM 16 DPSK modulated subcarriers.	72
Figure 3-17: (a) BER as a function of the OSNR for a 12.5 Gb/s DPSK AO-OFDM subcarrier in BtB for different number of subcarriers. (b) Required OSNR as a function of the total CD accumulated for different number of subcarriers.	74
Figure 3-18: Required OSNR as a function of the total CD for different number of subcarriers considering 20% of CP.	75
Figure 3-19: Setup configuration of an optical DQPSK transmitter and receiver [24]. ..	76
Figure 3-20: (a) BER as a function of the OSNR for a 25 Gb/s DQSK AO-OFDM subcarrier in BtB for different number of subcarriers. (b) Required OSNR as a function of the total CD accumulated for different number of subcarriers.	77
Figure 3-21: Required OSNR as a function of the total CD for different number of subcarriers considering 20% of CP.	77
Figure 3-22: AO-OFDM system. Mode-locked laser diode (MLLD), pseudo random symbol sequence (PRSS), digital to analog converter (DAC), optical I/Q Mach-Zehnder modulator (I/Q MZM), wavelength selective switch (WSS), array waveguide grating (AWG), single mode fiber (SMF), erbium doped fiber amplifier (EDFA), additive white Gaussian noise (AWGN), local oscillator (LO), balanced photodetector (BPD), analog to digital converter (ADC), frequency domain equalizer (FDE).	79

- Figure 3-23:** Log(BER) versus OSNR [dB/0.1nm] for the theoretical curve (red-line), analytical (blue-line) and simulation (black-line) with different frequency offset value. 83
- Figure 3-24:** SNR penalty per subcarrier (ΔSNR_k) versus the normalized laser linewidth to symbol duration for AO-OFDM (red line) and CO-OFDM (blue line) at a target BER = 10^{-3} 85
- Figure 3-25:** SNR penalty per subcarrier ($\Delta SNR_{EEP, k}$) due to EEPN as a function of laser linewidth from analytical eq. (21) and simulation results. The system consists of 37span of 80 km SMF fiber with $D=17$ ps/(nm-km). 86
- Figure 3-26:** Required OSNR corresponding to a FEC threshold of 10^{-3} BER as a function of the averaging window length. (a) PM-QPSK modulation with a linewidth of 300 kHz (red line) and 2 MHz (black line) after 2960 km.(b) PM-16-QAM modulation with a linewidth of 300 kHz (blue line) and 2 MHz (green line) after 720 km. 87
- Figure 3-27:** Required OSNR as a function of the RX bandwidth in back to back (BtB) shown in red line, after 37 spans for a sampling rate of $4 \cdot R_s$ (black line) and $6 \cdot R_s$ (blue line). 88
- Figure 3-28:** Required OSNR as a function of FFT-size after 37 spans for a sampling rate equal to $4 \cdot R_s$ (black line) and $6 \cdot R_s$ (blue line). 89
- Figure 3-29:** Maximum number of spans N as a function of the launch power per subcarrier $P_{Tx, sub}$. (a) 21 subcarrier PM-QPSK modulated. Poggiolini estimation model (blue line), Shieh estimation model (red line), simulated center subcarrier (black dots) and outmost subcarrier (green dots). (b) 7 subcarrier PM-16-QAM modulated. Poggiolini estimation model (blue line), Shieh estimation model (red line), simulated center subcarrier (black dots) and outmost subcarrier (green dots). 92
- Figure 3-30:** Transmitter setup. Tunable laser diode (TLD), polarization controller (PC), dual-drive Mach-Zehnder (DD-MZM), pulse pattern generator (PPG), erbium-doped fiber amplifier (EDFA), clock (CLK), phase-modulator (PM), single mode fiber (SMF), optical delay line (ODL), optical band pass filter (OBPF), differential quadrature phase shift keying (DQPSK) modulator, variable optical attenuator (VOA), wavelength selective switch (WSS), polarization scrambling (POL), pseudo random bit sequence (PRBS). 93
- Figure 3-31:** Receiver setup. Power meter (PWM), arrayed waveguide grating (AWG), delay line interferometer (DLI), balanced photodetector (BPD), bit-error rate tester (BERT). 94
- Figure 3-32:** Comb generation setup. 95
- Figure 3-33:** (a) Simulated output pulses from the DD-MZM, (b) and its PSD. 97

Figure 3-34: (a) Simulated output pulses from the DD-MZM + PM (red line) and only DD-MZM (blue line), (b) and its PSD after the DD-MZM + PM (blue line) and before PM (red line).	98
Figure 3-35: Pout (red line), first derivative phase (blue line) and second derivative phase (black line).	99
Figure 3-36: Variation of broadening factor $T1T0$ versus the fiber length z (m) in case of a single DD-MZM (blue line) and cascaded DD-MZM + PM (red line).	100
Figure 3-37: (a) Experimental measure optical comb spectrum, (b) time domain Gaussian pulse. (c) Numerical simulation of optical comb PSD and (d)	101
Figure 3-38: Measured eye diagrams of a 7 ch-transmission (a) B2B (b) after 35-km SMF.....	102
Figure 3-39: Spectrum measured at an AWG output port transmitting (a) seven AO-OFDM carriers (b) six subcarriers (the target subcarrier has been switched off).....	102
Figure 3-40: BER vs received power in BTB for the DQPSK-modulated subcarrier received with direct detection compared with five QPSK subcarriers received by coherent detection (the dashed line corresponds to the mean BER curve of the five subcarriers). A theoretical curve of BER with direct detection is also shown for reference.....	103
Figure 3-41: BER vs received power for a DQPSK-modulated subcarrier for B2B, 20-km, 28-km, and 35-km transmission over uncompensated SMF.	103
Figure 3-42: Experimental comparison measured transfer function between (a) an AWG and (b) FBG.....	104
Figure 3-43: (a) BER versus the received optical power for DPSK modulated subcarriers, when a FBG is used at the RX, (b) BER vs. received optical power for DPSK and DQPSK modulation, when an AWG is used at the RX.....	106
Figure 4-1: Fourier transform of a function in time-frequency plane.....	113
Figure 4-2: Wigner distribution of FrFT kernel function.	116
Figure 4-3: Tx Schematic of FrFT multicarrier system.	119
Figure 4-4: (a) Frequency-to-time conversion, (b) time-to-frequency conversion.....	120
Figure 4-5: Representation of the signal domain in the normalized time-frequency plane.	122
Figure 4-6: Chirp modulation effect on time-frequency plane.	123
Figure 4-7: Multicarrier FrFT for optical communications.	125

Figure 4-8: Coherent PM-FrFT setup.	126
Figure 4-9: Single subcarrier in time domain before and after SMF transmission.....	127
Figure 4-10: Subcarrier separation in frequency and time domain before and after transmission in optical fiber.....	128
Figure 4-11: Temporal delay between two adjacent subcarrier before and after transmission on SMF.	129
Figure 4-12: (a) Used subcarriers in percent, (b) SMF (Km) as a function of the p-FrFT parameter assuming different subcarrier number with symbol rate 28 Gbaud.....	130
Figure 4-13: Received pulse repetition Δt [ps] as a function of p ; theoretical formula in blue line and simulation in black points for a symbol rate transmitted 28 [Gbaud]...	131
Figure 4-14: (a) Spectrogram of a single subcarrier 4-QAM modulated with 28 [Gbaud], $N = 128$, and $p = 0.1$ before the SMF fiber, (b) after the SMF.....	131
Figure 4-15: Power spectral distribution (PSD) [dB] of a single subcarrier.	132
Figure 4-16: Power spectral distribution (PSD) [dB] of 126 subcarriers.	132
Figure 4-17: Schematic of FrFT based time lens to achieve frequency-to-time conversion. N is the total number of subcarriers or points of FrFT,.....	134
Figure 4-18: (a) BER versus the subcarrier index for $R = 28$ Gbaud, $p = 0.1$, OSNR=13.8 dB, $P_{avg} = -1$ dBm, $N = 128$, and $L_{SMF} = 190$ km (b) $R = 14$ Gbaud, OSNR=11.5 and $L_{SMF} = 760$ km. Total linewidth $\Delta\nu = 500$ kHz	135
Figure 4-19: BER as a function of OSNR after 760 km of SMF with $R = 28$ Gbaud, $p = 0.1$ and $N = 512$ for different laser linewidth. In blue line is shown the theoretical curve.....	136
Figure 4-20: Required OSNR versus linewidth time symbol duration in case of V&V (blue line) and BPS (red line) algorithm are used.....	137
Figure 4-21: BER as a function of OSNR after 19span x 80 km = 1520 km fiber propagation with $R = 28$ Gbaud, $p = 0.1$ and $N = 1024$ for different average power transmission per wavelength (P_{avg}). In blue line is shown the theoretical curve..	138
Figure 4-22: BER as a function of OSNR ; black line after 380km of SMF; green line after 382km and cyanine line after 385km.	139
Figure 4-23: Comparison between digital FrFT (red line) and SRRC (blue line) single carrier transmission in terms of OSNR penalty, DSP cost, Spectral efficiency and Power consumption considering only CD&PMD.....	140

CHAPTER 1

EVOLUTION OF OPTICAL FIBER COMMUNICATION

1.1 Motivations

Global IP traffic will reach 168 Exabyte per month by 2019, with an increase of fivefold over the past five years [1]. Figure 1-1 show the rate of grow per month from 2014 to 2019. This huge grow is due to a large bandwidth request coming from different services like high-definition interactive video, high resolution editing video and distributed system. New terms like big data or deluge of data are used to denote large volume and variety of data overwhelming the physical infrastructure evolution, the capacity to manage and to process it.

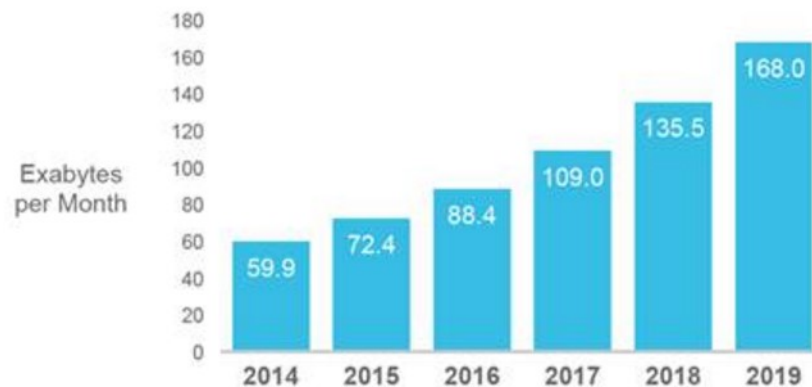


Figure 1-1: Cisco Global IP Traffic Forecast, 2014–2019 [1].

Unlike radiofrequency communications that have a very limit bandwidth from 300kHz-300GHz, lightwave technology use the infrared region from 30THz-300THz with capability of supporting Tb/s data over thousands of kilometer. Optical silica fiber is the medium used for such system with a very low cost production, 0.2dB/km loss and small probability of bit-error.

1.2 Evolution of optical transport networks

High speed serial interface (both client and line) and WDM capabilities are required to cope with such amount of data. From 2005 to 2010 the interface rate per-channel has remained nearly constant to 100Gb/s but there is transitions to high order modulation using coherent detection (green line) as shown in Figure 3-43. Using polarization division multiplexing (PDM), advanced coding and of superchannels it is expected to reach Tb/s per line interface. In Figure 3-43 white dots shows commercially available interface like Synchronous Digital Hierarchy/Optical Transport Network (SDH/OTN); black are for routers interface and grey for Ethernet standard. This technology development is due to the up-grade of network operation from circuit-switched serial interface to packet-switched parallel interface.

As shown in Figure 3-43, WDM played a very important role for cost effective data networking able to support very high data rates. Combination with PDM has further increase the data rates to approximately 100Tb/s. A further increase is very challenging because of the electrical bandwidth bottleneck limitation. Non-linear effects are viewed as the fundamental limits for the WDM systems which impose a smaller slope in scaling

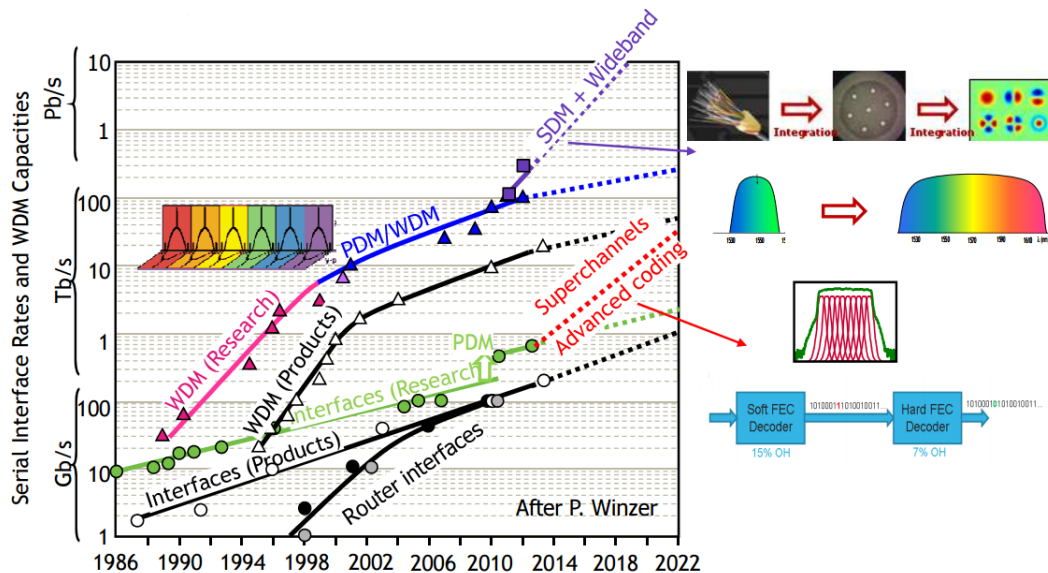


Figure 1-2: Evolution of electronically multiplexed serial interface rates and WDM capacities [2]-[3].

the capacities for both research (red triangle) and commercially products (white triangle). Spatial division multiplexing (SDM) and wideband signal is the ultimate physical frontier to overcome 100Tb/s shown with blue rectangular. Integration and use of multi-mode will contribute for a low cost and energy per bit. SDM solution will require, as for WDM system, an up-grade of all networks element, like reconfigurable add/drop multiplexer (ROADM), amplifier and transponders. However the cost of SDM employment seems very high for a mid-term solution.

As another alternative, optical packet/burst switching does not seems to be mature in order to cope with such amount of data [4] even though it has a low cost and energy per bit.

Networks operators are requiring a new generation of optical transport network to efficiently serve the high amount of volume data in a cost effective and scalable manner. Flexible optical network architectures have been proposed in response of this high capacities and disparate traffic granularity needs of the future Internet. Such networks rely on the capability to assign a spectrum portion, data rate and modulation format to bandwidth adaptable connections, with the aim of optimizing the use of the network resources and reducing the ecological impact of the network operation.

In the EU ASTRON project [5], a software-defined transceiver with improved and heterogeneous transmission characteristics based on OFDM that enables the wide and cost-efficient deployment of flexible core networks is proposed. This is achieved by the design and development of cost-optimised, compact and scalable photonic integrated components as well as all the necessary electronic circuits.

The key features of the ASTRON transceiver are the energy-efficiency and bit-rate flexibility to support rates from 10Gb/s to beyond 1Tb/s, for use in both access and core networks. To achieve energy efficiency, the ASTRON transceiver does not implement the discrete Fourier transform (DFT) in the electric domain, using power-consuming DSP and ADCs, but uses a specially designed AWG to multiplex and de-multiplex AO-OFDM and Nyquist-WDM signals directly in the optical domain [6].

Flexible optical networks, with the new concept of sliceable bandwidth-variable transponder and flexible optical cross-connect, present the benefit of providing customized spectral grids whenever new lightpaths are established. The allocation of

several channels to form super-channel configurations is performed according to user requests in a highly spectrum-efficient and scalable manner [7]. Modulation formats and center frequency are no more fixed and to establish an optical channel an optical cross connect with variable bandwidth will be able to allocate the desired spectrum requested.

According to ITU-T ongoing standardization, the minimum frequency slot unit that can be currently assigned is 12.5GHz and in the future will be scaled down to 6.25GHz [8]. Figure 3-43 show the ITU-T fixed grid comparison with the optical flexi grid. As can be observed from the figure with fixed grid transmission data rate are limit to 100Gb/s because it can be fit inside a frequency fixed slot of 50GHz. The 100Gb/s implementation in long-haul WDM transmission was coupled also with the availability of 100GbE client physical interface standardized by IEEE 802.3 in 2010. Next step for higher bit rate in WDM transmission is the use of 400Gb/s which interfaces is far from industrial availability. 400GbE task force has been launched by IEEE 802.3 in March 2014 for a standard approval expected by 2017.

If we consider the 400Gb/s implementation in a fixed 50GHz grid it will probably overlap with other frequency slot. If higher order modulation is considered the required

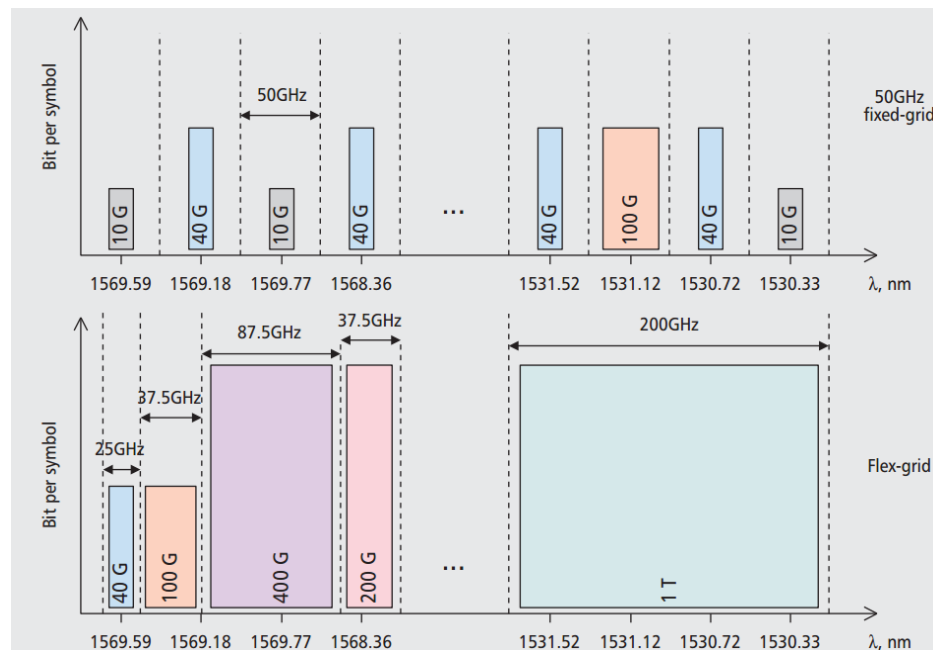


Figure 1-3: Spectrum utilization for fixed and flexi grid [7].

OSNR is very high due to laser phase noise and tight filtering in cascaded ROADMs. So the need for flexi grid in case of 400Gb/s data rates is crucial [9].

1.3 Evolution of optical access networks

Legacy access networks consist of pairs of copper point-to-point (P2P) links between the local exchange and customers; these systems can support digital subscriber line (DSL)-based services and Internet Protocol Television (IPTV), but are inadequate for future broadband multimedia applications. Hence, the last mile has become a critical bottleneck, limiting the profitability of network operators, who are experiencing a substantial reduction in revenues, due in part to the telecom competition, and in part to an increasing use of mobile phones.

Fiber-based systems are an effective solution for next the generation access networks (NGAN), as they can provide a large bandwidth to residential and business users [10]. PON architecture is the most deployed fiber to the x (FTTx) system, where x depends on where the optical link terminates [11]. The point-to-multipoint (P2MP) topology uses a passive optical splitter in the remote node (RN) to connect 32, 64 or even 128 users to the optical line termination (OLT) in the central office (CO). Users share the optical media with a time-division multiplexing (TDM) approach, and the downstream signal is broadcasted to all the optical network units (ONU), that select only the data corresponding to their own destination addresses. In the up-stream link, each ONU transmits only at time-slots assigned by the OLT, using a time division multiple access (TDMA) protocol to avoid collisions. Statistical multiplexing and media access control layer allow dynamic bandwidth assignment (DBA), to efficiently exploit the optical resources.

To further expand the bandwidth capacity, current FTTx systems should evolve toward WDM-based PONs, where the passive splitter in the RN is replaced by a arrayed waveguide grating (AWG)-based multiplexer. In this case, each ONU is assigned one or two wavelengths, and it is equipped with a tunable laser or a reflective semiconductor optical amplifier, which re-modulates an optical carrier sent from the OLT. In 2012, the full service access network (FSAN) consortium has selected the time and wavelength division multiplexing (TWDM)-based PON approach as a solution to upgrade optical access systems, with a smooth upgrade for deployed networks [12].

In a way similar to the WDM approach, an OFDM-based system uses orthogonal narrow-bandwidth subcarriers to transmit/receive to/from different ONUs [13]. The system flexibility and bandwidth granularity is higher, compared to the WDM technology, because the OLT can manage the number of the subcarriers assigned to each ONU and no guard-band is required. In addition, adaptable modulation format and power scheme are possible, and the near-far problem of TDM/TDMA systems is overcome, because there is no synchronization requirement for the ONUs, that are placed at different distances from the CO. This becomes of critical importance, when the users are assigned to different operators that do not share the same equipment in the CO. In addition, OFDM-based systems have colorless (non-user specific) ONUs, without expensive tunable lasers or large band amplifiers. Using a cyclic-prefix (CP), it is possible to perform circular convolution, to equalize chromatic dispersion in the frequency domain, with a reduced digital signal processing (DSP) complexity. In addition, OFDM systems can be integrated with both TDM and WDM technologies, to further increase the flexibility and the capacity of optical access systems. An OFDM configuration allows unbundling of the local loop (ULL), so that different operators can share the same infrastructure. The implementation of ULL in the NGAN is a strategic requirement for the European Union policy on competition and liberalization in the telecommunications market. Open access is extremely beneficial for NGANs, since it is associated with an increased competition, that drives higher levels of broadband penetration at lower prices.

1.4 High-speed single carrier and multicarrier transmission

In a single carrier transmission, only one wavelength carries the data information. An ideal pulse shaping, $\text{sinc}(t)$ pulse in time domain, is usually used to avoid intersymbol-interference (ISI) and to occupy the smallest possible bandwidth satisfying the Nyquist principle. In frequency domain it has approximately a rectangular spectrum, $\text{rect}(f)$.

In a multicarrier transmission the information is carried by multiple low-rate subcarriers which are overlapped in order to maximize the spectral efficiency, in one wavelength. OFDM is one of the approaches used by multicarrier transmission with overlapped subcarriers.

transmitter and intradyne coherent receivers. The optical power from a CW laser is divided in two parts and each part is independently modulated by a quadrature modulator, as shown in Figure 1-5(a).

The quadrature modulators typically comprise two nested Mach-Zehnder modulators with bias control and a 90° phase shifter in the outer modulators with phase control [14]-[15]. The output modulated signal are then combined in two orthogonal polarization states to obtain the signal transmitted on the optical fiber.

The coherent receiver required eight photodiode, four set of balanced detectors and linear amplifier, two ninety degree hybrid and two polarization splitting one for the received signal and the other for the local oscillator as shown Figure 3-43(b).

Single-carrier transceiver implementations are the preferred solutions for short-haul and metro applications, with baud rates ranging between 42.7 and 64 GBaud and high-level modulation formats, with 50 to 75 GHz channel spacing, achieving spectral efficiencies above 5.3 bit/s/Hz [9].

Compare to multi-carrier solutions, a single carrier uses adaptive algorithm for channel estimation, like constant modulus algorithm (CMA) and his variant for higher order modulation, like radius direct equalizer (RDE). Design of optical modulators is complex for higher order modulation which will increase the system cost.

In general it is easy to implement and require low cost, lower size and a low power dissipation. Compare to multicarrier it provide lower spectral efficiency but has the benefit of easy bandwidth allocation and network management.

ADC requirements regarding bandwidth and number of bits resolution for multi-level modulation is very challenging. At OFC 2016, NTT announced industry-first 16nm ultra-low power DSP for both 100G QPSK long-haul and 200G 16QAM metro optical links [16].

1.4.2 Multicarrier transmission

Targeting high speed channel generation, of the order of Tb/s, has meet with challenging limitation due primarily to limit sampling rate of ADC/DAC. To overcome this limitation, one of the approached proposed is to split the transmitted bandwidth in smaller sub-channels (subcarriers) in parallel which has led to creation of superchannels. The sub-channels are no needed to be overlapped as in OFDM. Nyquist optical/electrical

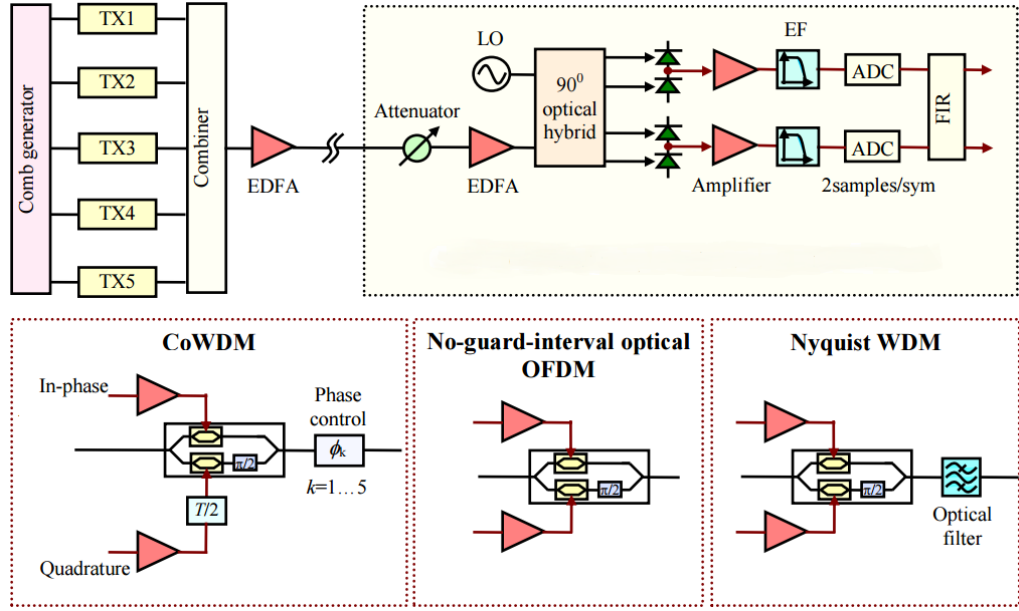


Figure 1-6: Different multicarrier transmission setup [17]

filters can be used to achieve same spectral efficiency as OFDM, known as Nyquist-WDM (NWDM). Figure 1-6 show some of the most investigated multiplexing technique for creating superchannels [17] using more than one wavelength. Strictly speaking dense-WDM (DWDM) is a multicarrier transmission. The main difference is the spacing between the subcarriers. At the transmitter side an optical comb generation is usually used to ensure that no cross-talk happen in frequency domain between the subcarriers.

Multicarrier trasmission based on coherent WDM (CoWDM) use rectangular time domain pulse and was proposed first in [18] with a spectral efficiency achieved of 1 b/s/Hz and 3 dB of penalty. In [17], as shown in Figure 1-6, an off-set QAM is proposed with a $T/2$ delay on one of the modulator arms. Off-set QAM shows less penalty because ISI and cross-talk is properly eliminated by using practical component. The main drawback of this setup is the phase control stabilization on each subcarrier because otherwise the cross-talk is very high. If offset-QAM is not used it require a high over-sampling rate. For a realistic implementation it requires a photonic integration, which is mandatory in all multicarrier systems.

Multicarrier trasmission based on no-guard-interval optical OFDM (NGI-OFDM) has been proposed and experimentally investigated in [19]-[20]. Similar to Co-WDM, NGI-

OFDM uses rectangular time domain pulse shape but with no phase control or offset-QAM modulation. To obtain good results an oversampling rate of a factor of 4 is used together with electrical pre-filter to eliminate aliasing effect. Electrical pre-filter are used for subcarrier separation at the receiver side. For both, CoWDM and NGI-OFDM the subcarrier spacing is equal to the data rate of each modulated subcarrier.

Multicarrier transmission based on Nyquist-WDM (NWDM) is proposed in [21] to improve the receiver sensitivity and to relax the requirements of the received filters by using an extra optical filter at the transmitter with a rectangular spectrum profile. Non ideal rectangular profile filter is very difficult to realize consequently residual cross-talk exists between the channels. Guard interval can relax the spectrum profile but in that case the system will achieve same spectral efficiency as in DWDM. Otherwise, electrical FIR filters can be used as in [22] with many number of taps at the transmitter side to keep cross-talk level low.

Multicarrier transmission based on coherent OFDM is another option to create superchannels with IFFT/FFT processing in the electrical domain. The highest capacity obtained using digital IFFT is 101.7Tb/s presented in [23]. The main drawback is the high peak to average power ratio (PAPR) which require non-linear mitigation. Phase noise mitigation technique are complex requiring a radio-frequency pilot tone which lie at the centres of the OFDM band to track the phase noise [24]. Cyclic prefix introduce overhead and reduce the spectral efficiency.

For next generation 400G transmission systems multi-carrier modulation formats will most likely to be used. Figure 1-7 show several 400G transceiver implementations for short-haul (SH), metro, long-haul (LH) and ultra-long-haul (ULH) applications according to OIF-Tech-Options-400G-01.0 [9]. The 400G application is sub-divided into short-haul (SH), Metropolitan (Metro), Long-Haul (LH) and Ultra Long-Haul (ULH). SH applications target very high spectral efficiency. Metro applications target at least 1000 km with the presence of ROADMs with fixed grid (100 GHz) or newly designed flexgrids (75 GHz). For LH application, the presence of ROADMs is optional but with distances close to 2000 km. ULH applications should be compatible with distances beyond 2000 km. Moving to 400G solutions faces a trade-off between spectral efficiency

and reach flexibility. If higher modulation levels are employed, reduced transmission reach is

	Modulation	Symbol Rate (Gbaud)	#sub-channels	DAC Options ¹	ADC Options ¹	State of the art Distance (km) ²
SH (~100 km, 50 GHz)	64QAM	42.7	1	1x4 80 GSa/s, 6.5 bits, 25 GHz ³	1x4 80 GSa/s, 6.5 bits, 25 GHz ³	300 ^[Buchali 14]
	16QAM	64	1	1x4 88 GSa/s, 16 GHz ^[Rios-Muller 14]	1x4 90 GSa/s, 25 GHz ^[Rios-Muller 14]	6600 ^[Rios-Muller 14]
Metro (<1000 km, 75/100 GHz, 10x ROADM)	16QAM	32	2	2x4 64 GSa/s, 16 GHz ⁴	2x4 80 GSa/s, 33 GHz ⁴	1800 ⁴
	16QAM	64	1	1x4 88 GSa/s, 16 GHz ^[Rios-Muller 14]	1x4 80 GSa/s, 33 GHz ^[Rios-Muller 14]	6600 ^[Rios-Muller 14]
	64QAM	14.2	3	3x4 32 GSa/s, 6.5 bits, 10 GHz ⁵	3x4 32 GSa/s, 6.5 bits, 10 GHz ⁵	600 ⁵
	MB-OFDM (16QAM)	8	8	8x4 12 GSa/s, 10 GHz ^[Pincemin 14]	8x4 50 GSa/s, 5 GHz ^[Pincemin 14]	1000 ^[Pincemin 14]
LH (~2000 km, optional ROADM)	QPSK	64	2	2x4 90 GSa/s, 5 bits, 20 GHz ⁶	2x4 90 GSa/s, 5 bits, 20 GHz ⁶	6577 ^[Wang 15]
	QPSK	32	4	4x4 64 GSa/s, 14 GHz ⁷	4x4 80 GSa/s, 33 GHz ⁷	2975 ⁷
	16QAM	16	4	4x4 32 GSa/s, 5 bits, 10 GHz ³	2x4 64 GSa/s, 5 bits, 17 GHz ³	630 ³
ULH (>2000 km)	QPSK	32	4	4x4 64 GSa/s, 14 GHz ⁷	4x4 80 GSa/s, 33 GHz ⁷	2975 ⁷
	8QAM	42.7	2	2x4 64 GSa/s, 16 GHz ⁴	2x4 80 GSa/s, 33 GHz ⁴	6787 ^[SZhang 14]
	16QAM	21	3	3x4 40 GSa/s, 6 bits, 11 GHz ⁵	3x4 40 GSa/s, 6 bits, 11 GHz ⁵	5000 ⁵

Figure 1-7: Potential 400G architectures in the state of the art. ¹DAC and ADC characteristics taken either from Section 6 or from the state of the art. ²Distances reported either in the state of the art or from OIF contributions. ³OIF2014.030.00, ⁴OIF2015.030.01, ⁵OIF2015.100.00, ⁶OIF2015.037.01, ⁷OIF2014.031.00 [9].

unavoidable because these high-order QAMs require higher OSNR, and are more sensitive to laser phase noise and to fibre non-linear effects. The higher the QAM order, the lower the tolerance to narrow optical filtering due to ROADM cascading.

According to the IEEE 802.3bs 400GbE Task Force timeline adopted in September 2015, the standard is expected in December 2017 [25].

1.5 Thesis outline and contributions

From the analysis done in the previous section both access and transport networks are bottleneck when considering the future demand of bandwidth, low cost solution and low power consumption.

The research objective of this thesis is to employ optical communications technology to provide a high speed novel transmission data to overcome the traditional time division multiplexing technique used commonly in access and transport layer.

In this thesis the goal is to provide a design and analysis of cost effective fiber optic access network for unbundling the local loop employing analytical and simulations tools. Propose, design and analyze high speed all optical OFDM transmission. Establish an experimental test-bed to experimentally verify the analyzed high speed real time transmission.

Propose, design and analyze a novel multicarrier transmission for optical communications systems and identify the limitations of the proposed transmission.

The following present a pre chapter overview of the thesis and the main contributions.

In chapter 1, motivation and state of the art of current research topic are described for both access and transport layers.

In chapter 2 OFDM is proposed for optical access network with direct detection for a low cost solution. OFDM offers colorless ONUs, reduced DSP complexity and compatibility with TDM/WDM technology. It also allows unbundling the local loops if reflective semiconductor optical amplifier (RSOA) are used at the ONU side. RSOA characterization is performed analytically and by simulation commercial software. Adaptive OFDM is used to overcome the RSOA bandwidth limitations and evaluation of the access networks based on RSOA and OFDM is performed for system design parameters.

In chapter 3 all optical OFDM (AO-OFDM) is proposed with a very high spectral efficiency and aggregated data rate. Direct detection DPSK/DQPSK AO-OFDM transmission is investigated with and without cyclic prefix. Polarization multiplexing AO-OFDM with coherent detection is evaluated by analytically formula and simulations result. Experimentally AO-OFDM system is demonstrated at National Institute of Communications and Information Technology (NICT), Japan, with no optical gating and chromatic dispersion for both direct and coherent detection by using a wavelength selective switch (WSS) at the transmitter side and an AWG at the receiver. Optical comb generation for AO-OFDM is evaluated both analytically and by experimental result.

Finally, an experimental comparison is performed between a fiber Bragg grating (FBG) and AWG for AO-OFDM demultiplexing.

In chapter 4 a multicarrier transmission based on electrical fractional Fourier transform (FrFT) is theoretically investigated and proposed for high speed optical communications networks. Theoretical time lens effect is derived based on FrFT and chromatic dispersion effect supported by simulation results. A fundamental study to explore the limits of the proposed system is performed and detailed results have been presented. It is demonstrated that the proposed optical transmission can encode data on both polarization and no dispersion compensation is needed at the receiver side. Further more, it is shown that the effect of phase noise is relaxed if compare to electrical OFDM transmission.

1.5.1 List of publications

The work presented in this thesis has led to the following publications:

- **J. Hoxha**, J. Morosi, S. Shimizu, P. Martelli, P. Boffi, N. Wada, and G. Cincotti, “*Spectrally-efficient all-optical OFDM by WSS and AWG*,” Optics Express **23**(9), 10986-10996 (2015)
- J. Morosi, **J. Hoxha**, P. Martelli, P. Parolari, G. Cincotti, S. Shimizu, N. Wada, and P. Boffi, “*25 Gbit/s per User Coherent All-Optical OFDM for Tbit/s-Capable PONs*,” J. Opt. Commun. Netw. **8**, 190-195 (2016)
- P. Zakyntinos, G. Cincotti, M. Nazarathy, R. Kaiser, P. Bayvel, R. I. Killey, M. Angelou, S. B. Ezra, M. Irion, A. Tolmachev, B. Gomez Saavedra, **J. Hoxha**, V. Grundlehner, N. Psaila, G. Vollrath, R. Magri, G. Papastergiou and I. Tomkos, “*Advanced Hybrid Integrated Transceivers to Realize Flexible Terabit Networking*,” IEEE Photonics Society News, February 2014, Vol. 28, No. 1
- **J. Hoxha**, G. Cincotti, S. Shimizu and N. Wada, “*FBG- and AWG-based AO-OFDM demultiplexing*,” Photonics in Switching (PS), 2015 International Conference, Florence, 2015, pp. 82-84.
- **J. Hoxha**, G. Zarra and G. Cincotti, “*A flexible OFDM system for unbundling the local loop in optical access networks*,” Networks and Optical Communications - (NOC), 2014 19th European Conference, Milano, 2014, pp. 63-66.

- **J. Hoxha**, G. Cincotti, M. Nazarathy, P. Zakyntinos and I. Tomkos, "*Software defined transceivers for high-speed flexible optical networks*," *Future Network and Mobile Summit (FutureNetworkSummit)*, 2013, Lisboa, 2013, pp. 1-8.
- **J. Hoxha** and G. Cincotti, "*Performance limits of all-optical OFDM systems*," 2013 15th International Conference on Transparent Optical Networks (ICTON), Cartagena, 2013, pp. 1-4.
- **J. Hoxha**, G. Cincotti, N. P. Diamantopoulos, P. Zakyntinos and I. Tomkos, "*All-optical implementation of OFDM/NWDM Tx/Rx*," 2013 15th International Conference on Transparent Optical Networks (ICTON), Cartagena, 2013, pp. 1-4.
- J. Morosi, **J. Hoxha**, S. Shimizu, P. Martelli, P. Boffi, N. Wada, G. Cincotti, "*QPSK- based all optical OFDM with direct and coherent detection.*" 2015 Fotonica AEIT Italian Conference on Photonics Technologies - Turin, Italy, May 6 - 8 2015
- **J. Hoxha**, G. Zarra, G. Cincotti, "*OFDM-based solutions for unbundling the local loop in optical access networks*," 16o Convegno Nazionale sulle Tecniche Fotoniche nelle Telecomunicazioni (FOTONICA), Naples, Italy 2014
- **J. Hoxha**, G. Cincotti, "*System performance of coherent all-optical OFDM in long-haul transmission*," 15o Convegno Nazionale sulle Tecniche Fotoniche nelle Telecomunicazioni (FOTONICA), Milano, Italy 2013

References

- [1] http://www.cisco.com/c/en/us/solutions/collateral/service-provider/visual-networking-index-vni/VNI_Hyperconnectivity_WP.html
- [2] P. J. Winzer, "Challenges and Evolution of Optical Transport Networks", ECOC 2010, Torino, Italy, Paper We.8.D.1.
- [3] <http://optical-networks.iscte-iul.pt/presentations/alcatel.pdf>
- [4] R. S. Tucker. Optical packet switching: A reality check. Optical Switching and Networking, 5(1):2–9, June 2008.
- [5] <http://www.ict-astron.eu/>
- [6] J. Hoxha, G. Cincotti, M. Nazarathy, P. Zakyntinos, I. Tomkos, "Software defined transceivers for high-speed flexible optical networks," Future Network & MobileSummit 2013, Lisbon, Portugal 2013.
- [7] A. Napoli, et al., "Next Generation Elastic Optical Networks: the Vision of the European Research Project IDEALIST," IEEE Communications Magazine, Vol. 53, No. 2, February 2015.
- [8] ITU-T. Transmission systems and media, digital systems and networks, February 2012
- [9] <http://www.oiforum.com/wp-content/uploads/OIF-Tech-Options-400G-01.0.pdf>
- [10] Shumate,"Fiber-to-the-Home: 1977-2007," J. Lightw. Technol., vol. 26, no. 9, pp. 1093-1103, May 2008.
- [11] T. Koonen,"Fiber to the Home/Fiber to the Premises: What, Where, and When?," vol. 94, no. 5, pp. 911-934, May, 2006.
- [12] J. J. Zhang and N. Ansari," Design of WDM PON with tunable lasers: The upstream scenario," J. Lightw. Technol., vol. 28, no. 2, pp. 228-236, January 2010.
- [13] N. Cvijetic,"OFDM for next-generation optical access networks," J. Lightw. Technol. vol.. 30, .pp. 384-398, 2012.
- [14] <http://www.oiforum.com/public/documents/OIF-PMQ-TX-01.1.pdf>
- [15] http://www.oiforum.com/public/documents/OIF_DPC_RX-01.1.pdf
- [16] <http://www.ntt-electronics.com/en/news/2016/3/industry-first-16nm-100g-200g-coherent-dsp.html>
- [17] J. Zhao and A. D. Ellis, "Offset-QAM based coherent WDM for spectral efficiency enhancement", 19, 14617-14631 (2011)
- [18] A. D. Ellis and F. C. G. Gunning, "Spectral density enhancement using coherent WDM," IEEE Photon. Technol. Lett. 17(2), 504–506 (2005).

- [19] R. Dischler and F. Buchali, "Transmission of 1.2 Tb/s continuous waveband PDM-OFDM-FDM signal with spectral efficiency of 3.3 but/s/Hz over 400 km of SSMF," OFC'09, post-deadline paper PDP2.
- [20] S. Chandrasekhar, X. Liu, B. Zhu, and D. W. Peckham, "Transmission of a 1.2-Tb/s 24-carrier no-guard-interval coherent OFDM superchannel over 7200-km of ultra-large-area fiber," ECOC'09, post-deadline paper PD2.6.
- [21] G. Bosco, A. Carena, V. Curri, P. Poggiolini, and F. Forghieri, "Performance limits of Nyquist-WDM and CoOFDM in high-speed PM-QPSK systems," IEEE Photon. Technol. Lett. 22(15), 1129–1131 (2010).
- [22] R. Schmogrow, R. Bouziane, M. Meyer, P. A. Milder, P. C. Schindler, R. I. Killey, P. Bayvel, C. Koos, W. Freude, and J. Leuthold, "Real-time OFDM or Nyquist pulse generation – which performs better with limited resources?," Opt. Express 20, B543-B551 (2012).
- [23] D. Qian, M. Huang, E. Ip, Y. Huang, Y. Shao, J. Hu, and T. Wang, "101.7-Tb/s (370×294-Gb/s) PDM-128QAM-OFDM Transmission over 3×55-km SSMF using Pilot-based Phase Noise Mitigation," in Optical Fiber Communication Conference/National Fiber Optic Engineers Conference 2011, OSA Technical Digest (CD) (Optical Society of America, 2011), paper PDPB5.
- [24] S. L. Jansen, I. Morita, T. C. W. Schenk, N. Takeda and H. Tanaka, "Coherent Optical 25.8-Gb/s OFDM Transmission Over 4160-km SSMF," in Journal of Lightwave Technology, vol. 26, no. 1, pp. 6-15, Jan.1, 2008.
- [25] <http://www.ieee802.org/3/bs/>

CHAPTER 2

OPTICAL ACCESS NETWORKS BASED ON ELECTRICAL OFDM

2.1 Introduction

Optical access networks comprise the link between ONU (customers) and OLT (service provider) as shown in Figure 2-1. This is usually called ‘last mile’ from the service provider perspective. The OLT is then connected to the core network, which provides very high speed transmission from Gb/s up to Tb/s using either SONET/SDH technology. This high speed transmission is not available at the ONU because of installed copper infrastructure which cannot provide this high amount of data. The solution on the so called ‘last-mile bottleneck’ is using the optical fiber.

In the PON architecture a single fiber originates from the OLT and power splitter are usually used to deliver the signal to ONU.

Different multiple access techniques are used to avoid collisions in the up-stream traffic originated from the ONUs, which include TDMA, WDMA, optical code-division multiplexing access (OCDMA).

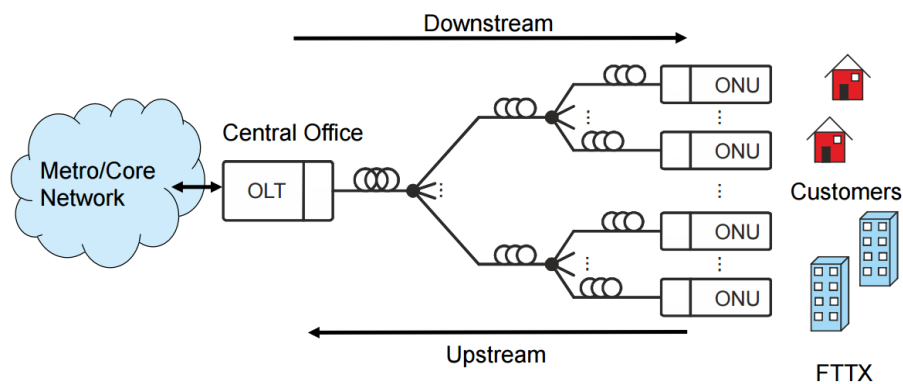


Figure 2-1: Schematic of the access networks [1].

OFDMA is an alternative solution which provides a continuous transmission (not a burst one), enable dynamic bandwidth allocation which provide a high flexibility in both time and frequency domain and make use of DSP for channel equalization.

In order to increase the data rate and the number of ONU subscriber, WDM is one the solution to be used together with OFDMA.

2.1.1 Electrical OFDM with optical modulation

Optical field of a continuous wave (CW) laser offers at least five degree of freedom for information modulation: field amplitude, intensity, phase, frequency and polarization. In practice frequency modulation is not used.

In general, the optical OFDM solution can be divided into two main groups: 1) Coherent detection (CO) with field modulation 2) Direct detection with intensity/field modulation IM/DD shown in Figure 2-2(a) and (b), respectively. CO-OFDM present a better receiver sensitivity and a higher spectral efficiency if compare to DD-OFDM [3].

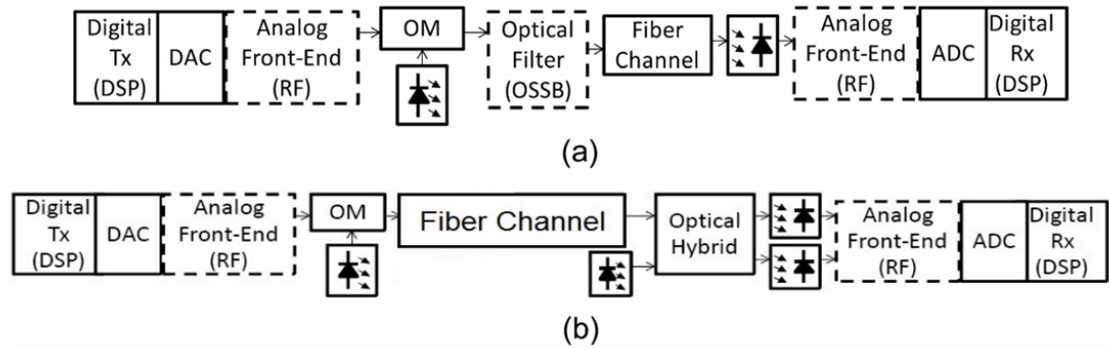


Figure 2-2: (a) Block diagram of IM/DD and (b) CO-OFDM using optical modulation [2].

2.1.1.1 IM/DD

The OFDM multicarrier signal is generated in the electrical domain, as shown in Figure 2-2(a), where an analog front end is used for radio frequency (RF) up converter after the DAC. An optical modulator (OM) is used to convert the RF-OFDM signal in the optical

domain using either the field or intensity modulation. In case of field modulation an I/Q modulator is needed. In case of intensity modulator a real electrical OFDM signal is needed to modulate the optical carriers. A DC bias is used to generate a positive electrical signal. Because at the receiver side a single photodiode is used, the optical carrier should be transmitted. Half of the power is used for the optical carrier and only half for the OFDM signal. This system was proposed for the first time in [4] and shown in Figure 2-3.

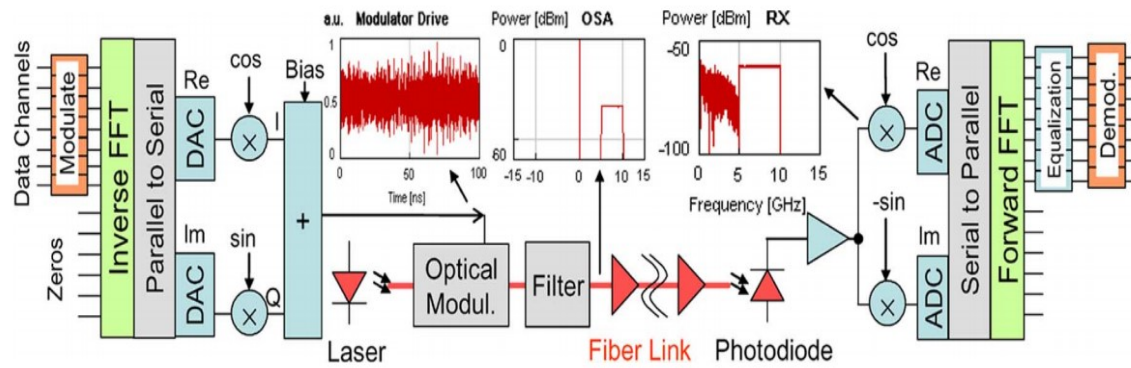


Figure 2-3: Optical OFDM with DC bias and DD receiver [4].

At the receiver, some nulls power are produced at particular frequency obtained from the mixing terms between sidebands and optical carriers after optical fiber propagation. This is due to chromatic dispersion which can cause conversion from amplitude modulation into phase modulation [5]. To avoid this effects, an optical filter is used to filter the double side band OFDM signal as in [6]. The optical signal at the output of the filter is called single side band (SSB) OFDM signal. In alternative an optical single side band (OSSB) can be generated if a Hilbert transform is used as in [7] without the need of an optical filter. In this case a dual electrode MZM is driven by a real OFDM signal and by its Hilbert transform. The real OFDM signal is obtained by the Hermitian symmetry and the Hilbert transform is obtained by using 90° electrical hybrid. In this case there is no need for RF up-conversion because the spacing from the optical carrier can be obtained by using virtual subcarriers. In alternative, only a Hermitian symmetry can be used together with an optical filter to obtain a SSB OFDM signal. The optical modulator is a dual electrode Mach Zehnder modulator (MZM) biased in quadrature. The Hermitian

symmetry is simply obtain by using one half of the IFFT size as the complex conjugate of the other half. Even in this case some of the subcarriers are filled with zero (virtual subcarriers) to leave a guard band between the OFDM signal and the optical carrier. A 180° electrical phase shift is used between the two arms of the MZM.

2.1.1.2 CO detection

In the CO-OFDM approach optical carrier is not transmitted because it is suppressed and the optical OFDM signal show more power allocated in it. An optical I/Q modulator is usually used which generate only one sideband. For this reason no optical filter is needed as in IM/DD setup. At the receiver side a complete access to the full optical field by using a local oscillator allow to maximize the transmitted data rate and no guard band is needed [3]. The sensitivity of the receiver is increased because of the local oscillator and long reach trasmission is possible to achieve. As shown in Figure 2-2 (b) at the receiver side an optical 2x4 90° hybrid is needed together with balanced photodiode and CW local oscillator. The analog front end RF is shown as in reference [2], but of course this is not mandatory and will simplify the CO-OFDM setup.

There are also many drawbacks in CO-OFDM like: phase noise and frequency shift originated by CW local oscillator. Advanced algorithm are required for mitigating this effects in DSP.

Due to the high cost derived from the optical hybrid, CW local oscillator and DSP transceiver usually the CO-OFDM is not considered for the moment as a solution for the PON.

2.2 OFDM

The schematic of OFDM setup is shown Figure 2-4. The transmitted binary data streams are mapped to complex symbols from a particular modulation formats (M-PSK, M-QAM or differential modulation) [1]. Then a serial to parallel (S/P) block is used to convert the symbols in parallel. Modulated symbols enter the inverse fast Fourier transform (IFFT) which provide an efficient method for computing the IDFT[9]. The output of the IFFT can be written as [10]:

$$x[n] = \sum_{k=0}^{N-1} X[k] e^{j2\pi k \frac{n}{N}} \quad 2-1$$

with $X[k]$ input modulated complex symbols (Fourier coefficients), $x[n]$ provide the output time series where the n -th time domain sample is the sum of N complex exponential functions and N is the IFFT size. In order to avoid overlapped between OFDM symbols, guard intervals is added (cyclic prefix).

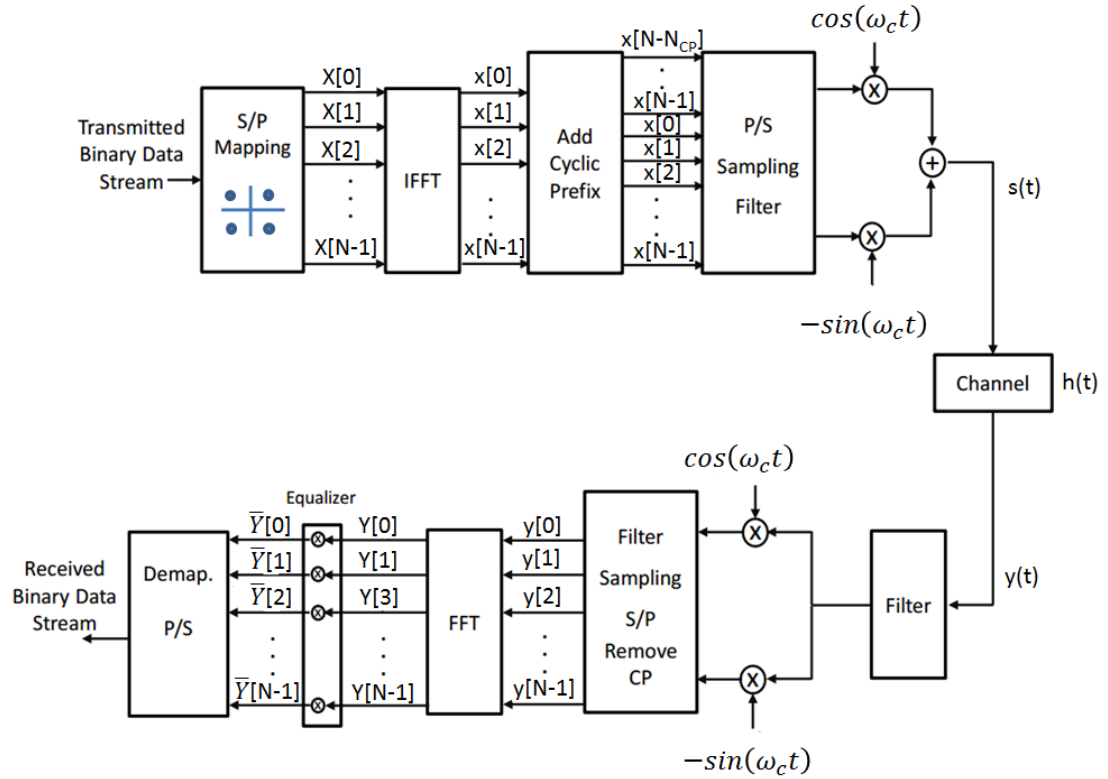


Figure 2-4: Schematic of OFDM setup.

In this case a copy of the data $x_{CP} = (x[N - 1], \dots, x[N - N_{CP}])$ will be added at the beginning of the sequence $x[n]$ which define the length of the OFDM symbol. The duration of the cyclic prefix, T_{CP} , is related to the channel impulse response length. To avoid inter-symbol interference it should be made longer which on the other hand decrease the spectral efficiency of the system. The complex output is then sampled at a rate double of Nyquist frequency equal to $2 \cdot N/2T$, where T is the OFDM symbol period without cyclic prefix. To relax the bandwidth limitation due to low pass filtering and the

sampling rate some of the subcarriers, usually 20%, are filled with zeros. These subcarriers are usually called virtual subcarriers. After the IFFT a complex signal is obtained and in order to transmit both the in-phase and quadrature component a frequency up-conversion is performed at ω_c .

The analog complex OFDM signal transmitted, considering only one OFDM symbol is written as:

$$s(t) = e^{j\omega_c t} \sum_{k=0}^{N-1} X[k] e^{j\omega_k t} * h_{Tx} \quad 2-2$$

where h_{Tx} is the transmitter filter impulse response.

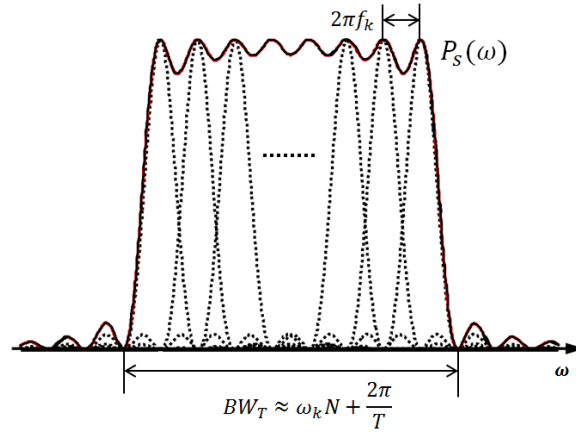


Figure 2-5: Power spectral density of the OFDM signal.

If the transmitted symbols are uncorrelated the power spectral density of the OFDM signal is [1]:

$$P_s(\omega) = \frac{T}{N^2} \sum_{k=0}^{N-1} E[|X[k]|^2] \text{sinc}^2(\omega - \omega_k) \quad 2-3$$

where $E[|X[k]|^2]$ is the average power per symbol on k th subcarrier.

The power spectral density is shown in Figure 2-5. The total bandwidth of the OFDM signal is approximated as: $BW_T \approx \omega_k N + 2\pi/T$ if a null-to-null bandwidth definition is used.

To recover the transmitted symbols a Fourier transform is performed on the received signals after down-conversion. The channel/filtering effects is neglected. The received signal is then written as:

$$\begin{aligned}
 Y[k] &= \frac{1}{T} \int_0^T s(t) e^{-j\omega_k t} dt \\
 &= \sum_{i=0}^{N-1} X[i] \frac{1}{T} \int_0^T e^{j(\omega_i - \omega_k)t} dt \\
 &= \sum_{i=0}^{N-1} X[i] e^{\frac{j(\omega_i - \omega_k)T}{2}} \frac{\sin\left[\frac{(\omega_i - \omega_k)T}{2}\right]}{\frac{(\omega_i - \omega_k)T}{2}} \\
 &= X[k]
 \end{aligned} \tag{2-4}$$

where the last equivalence is obtained if $\omega_i = \omega_k$ (orthogonality of OFDM subcarriers). Another condition can be derived from Eq. 2-4: $\omega_i - \omega_k = 2\pi m/T$ which states that in order to avoid inter-carrier interference the transmitted subcarriers must be spaced an integer multiply m of the inverse OFDM symbol duration. In order to be orthogonal and to recover the transmitted symbol with a match filter. The orthogonality condition allow to transmit overlapped spectra and to increase the spectral efficiency.

The received signal considering channel and filtering effect is sampled with an analog to digital converter after filtering with a low pass filter to avoid aliasing. The cyclic prefix is then removed and the discrete FFT operation is performed. The discrete symbols can be written as:

$$Y[k] = \sum_{n=0}^{N-1} y[n] e^{-j2\pi k \frac{n}{N}} \tag{2-5}$$

where:

$$y[n] = \sum_{i=0}^{N-1} X[i] e^{-j2\pi n \frac{i}{N}} * h_{Tx}[n] * h[n] * h_{Rx}[n] \tag{2-6}$$

$h_{Tx}[n], h[n], h_{Rx}[n]$ are the sampled version of the low pass filter, channel impulse response and received filter, respectively. Eq. 2-4 perform a circular convolution due to the cyclic prefix because the extended OFDM symbol now appear like a ‘periodic signal’ when the convolution with the channel impulse response is performed. Due to the FFT

property the received symbols can be written as: $Y[k] = X[k] \cdot H[k]$ where $H[k]$ is the discrete overall channel transfer function. A zero forcing equalizer can be designed by estimating the channel transfer function, $\hat{H}[k]$, by dividing the received symbols obtaining an equalized signal as:

$$\hat{Y}[k] = Y[k]/\hat{H}[k] \quad 2-5$$

2.3 Electrical OFDM for PONs

Next generation optical access networks is expected to deliver high data rate providing multiple service using low-cost architectures and a flexible bandwidth allocation. Current TDMA-PON present high complexity to scale the data rate up to Gb/s due to the burst mode trasmission implementation. On the other hand, WDMA-PON can provide a high data rate by using a dedicated wavelength for each ONU. However it lacks in flexibility bandwidth allocation and bandwidth granularity.

OFDMA-PON was first proposed in [13] to provide multiple service. The main principle of OFDMA is to use a subset of different subcarriers for each ONU. If only 4 ONU is consider for simplicity like in [1], the down-stream and up-stream schematic is then shown in Figure 2-6, where each ONU process only a group of the total OFDM subcarriers and the OLT process all the subcarriers.

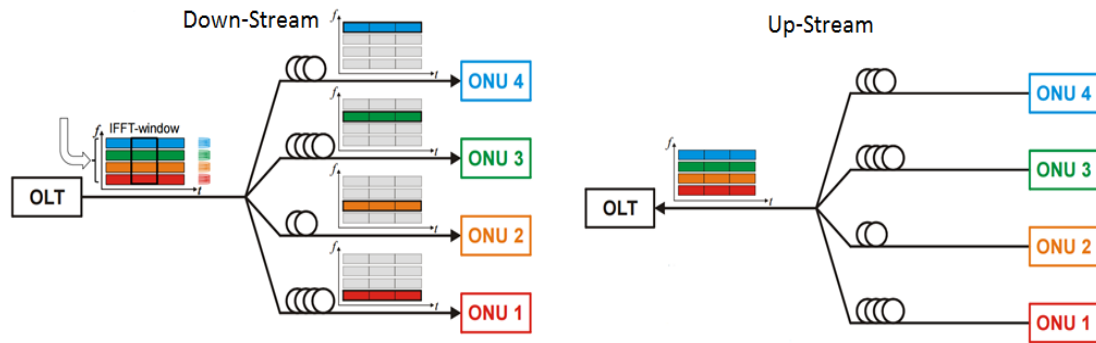


Figure 2-6: Down-stream and up-stream scenario for PON based on OFDM [1].

OFDMA is also compatible with WDMA-TDMA and they can all be used together. If the OLT assign a group of subcarriers to a ONU but the it has not enough traffic data to delivery then it can share the non-used subcarriers with other ONU using TDM. OLT is able to process in the same time slot different ONU and different wavelength (WDM) [2]. Albeit many advantage like high spectral efficiency, reduced cost compare to WDM (because OFDM needs less receivers) and transparent service provider there are also challenges for up-stream scenario like: different length of optical fiber connecting each ONU to OLT, carrier offset between the different subgroup of subcarriers and different polarization state. For down-stream the OFDM-PON scenario is more realistic and able to work on real time transmission.

2.3.1 Unbundling the local loop

In this work the focusing will be on the up-stream scenario. Another important requirements of the next generation optical access networks is to allow competition among different service provider. This should be provided through the ‘unbundling of the local loop’ (ULL) technology. Nowadays this is accomplished by traditional legacy twisted pair DSL (digital subscriber line) access with the two most popular alternative Asymmetric DSL (ADSL) and ADSL+. In the near future, the Very High-Speed DSL (VDSL) with vectoring technology is expected to provide high data rate per user up to 100Mb/s or more, an increase on the number of customer and a fast return on the investment (ROI) by reusing the same infrastructure [14]. Vectoring technology is basically based on a reduce crosstalk between DSLs.

The most used ULL technologies are direct access and bit-stream [15]-[16]. In direct access different operators who require to access the ONU is provided with a point-to-point physical access even though the infrastructure is provided by the proprietary service provider (incumbent). Usually at the CO each operators have its own ‘room’ with its own modem and their own DSL Access Multiplexer (DSLAM). So basically, the competitive operator is leasing the copper from a wholesale or service provider.

On the other hand, bit-stream technology is based on a virtual unbundling at data link layer (or Ethernet). In other words the incumbent is wholesaling virtual point-to-point connections to ULL. Virtual Unbundling of the Local Access (VULA) at the CO based

on the bit stream is expected to decrease the gap between the virtual connections and physical one [17].

2.3.2 OFDM-PON based on IM/DD for ULL

OFDM perform physical layer unbundling by simply assigning different subcarrier to different operator and users. A simple but effective approach for ULL, considering a 10Gb/s link and assigning different OFDM subcarriers to different operators is described. The open access scheme is highly efficient as it does not require optical guard band; direct detection is used at the receiver, to reduce the system costs and power consumption. Different modulation formats have been considered, so that each operator can independently choose its own system capacity.

The open access network system consists of four different operators that share the same optical distribution network (ODN) to reach their own customers. Each operator is connected to a single user, and the number of users can be further increased, reducing the received power, due to the increased splitting ratio in the RN, as well as the bandwidth (number of subcarriers) associated to each user. In a flexible-bandwidth access systems, these limitations could be compensated by dynamically changing the modulation format or increasing the baud rate. However, the maximum symbol rate is limited by the chromatic dispersion and non-linear effects, posing a constraint on the maximum link span. It is only consider the upstream link, but the downstream connection can be designed using a similar architecture.

A flexible scalable DBA protocol can be used to manage the overall system bandwidth, by assigning different subcarriers to different operators, according to different service level agreements (SLA).

A single-user 10Gb/s OFDM-based upstream system setup is shown in Figure 2-7; the OFDM baseband signal is composed of 512 subcarriers, and additional 64 subcarriers are allocated for CP (12.5%); 4 and 16 quadrature amplitude modulation (QAM) formats are used. In the first case, the signal baud rate is 5 Gbaud/s that is reduced to 2.5 Gbaud/s for 16-QAM modulation.

A spectral gap is inserted between the optical carrier and the OFDM signal, to eliminate the intermodulation products at the receiver side; therefore, after the digital-to-analog

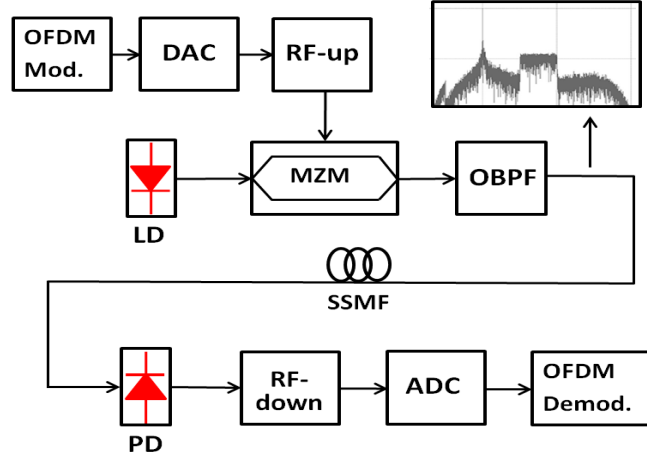


Figure 2-7: P2P OFDM-based system.

converter (DAC) with oversampling of a factor of 4, a radiofrequency (RF) oscillator is used to perform a 7.5 GHz up conversion. A raised cosine low-pass (LP) filter, with 0.2 roll-off factor, is used to suppress aliasing. The output signal is:

$$s(t) = e^{j\omega_0 t} + \alpha e^{j(\omega_0 - \Delta\omega)t} \sum_{k=0}^{N-1} X[k] e^{j\omega_k t} \quad 2-6$$

where ω_0 is the optical carrier angular frequency, $\Delta\omega$ is the guard band interval and α is a scaling factor to account for different strength power between the shifted OFDM signal and the optical carrier [18]. At the receiver the OFDM signal can be approximated as:

$$y(t) = e^{j(\omega_0 t + \Phi_D(-\Delta\omega) + \varphi(t))} + \alpha e^{j(\omega_0 - \Delta\omega)t + j\varphi(t)} \sum_{k=0}^{N-1} X[k] e^{j\omega_k t + j\Phi_D(\omega_k)} \quad 2-7$$

where $\Phi_D(\omega_k) = (\omega_k^2 \cdot c \cdot D_T) / \omega_0^2$ is the phase shift due to chromatic dispersion on the fiber with D_T total accumulated chromatic dispersion and c is the speed of light. The received photocurrent after the photodiode is expressed as:

$$\begin{aligned} I(t) \cong & 1 + 2\alpha \operatorname{Re} \left\{ e^{j\omega_0 t} \sum_{k=0}^{N-1} X[k] e^{j\omega_k t + j\Phi_D(\omega_k) - j\Phi_D(-\Delta\omega)} \right\} + \\ & + |\alpha|^2 \sum_{k_1=0}^{N-1} \sum_{k_2=0}^{N-1} X^*[k_1] X[k_2] e^{j(\omega_{k_1} - \omega_{k_2})t + j\Phi_D(\omega_{k_1}) - j\Phi_D(-\omega_{k_2})} \end{aligned} \quad 2-8$$

where the first term is the DC, in the second term are the information symbols to be recover and third term is a second order non-linear component. The aim of the spectral gap inserted by the RF electrical up-conversion is to filter out the third term in Eq. 2-10.

A laser with 100 kHz linewidth is used as an optical source and the Mach-Zehnder modulator (MZM), biased at the quadrature point, converts the RF signal into a dual side-band optical signal. To reduce the power penalty due to chromatic dispersion, it is introduced an optical bandpass filter (OBPF) to suppress the lower spectral content and to generate a single side band optical signal.

The signal is transmitted over a standard single mode fiber (SSMF), with 0.2 dB/km attenuation parameter, 17 ps/nm/km dispersion parameter and $2.6 \cdot 10^{-20} \text{ m}^2/\text{W}$ nonlinear index. An avalanche photodiode (APD) is used to enhance the system performance.

The photodiode responsivity is 0.9 A/W and the multiplication factor is 2; both thermal and shot noises are considered. To reduce costs, a Fabry-Perot (FP) lasers is used in each ONU and electrical oscillator for down-conversion of the RF-OFDM signal.

After removing the cyclic prefix, the Fast Fourier Transform (FFT) of 512 points is used to recover the modulated symbols for each subcarriers. Only one OFDM symbol is used for channel estimation and a single one tap equalizer is used for a symbol by symbol receiver [19]. Figure 2-8 illustrates the setup for a 4-ONU PON system.

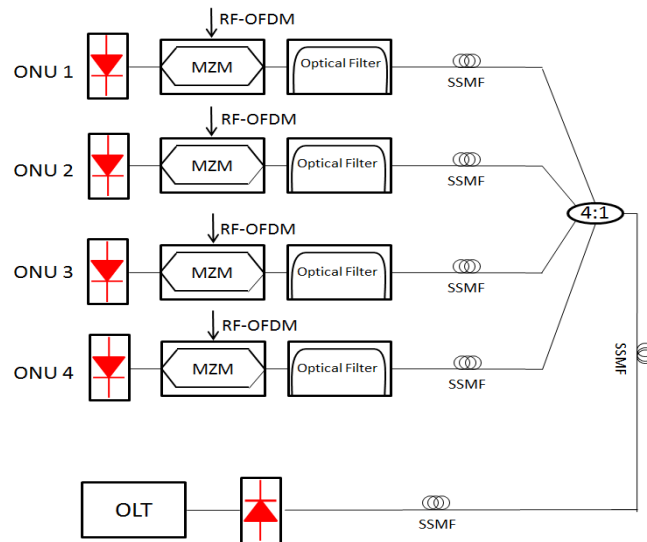


Figure 2-8: OFDM-based PON.

The transmission bandwidth is divided among the users, leaving only two subcarrier for guard band. Each ONU transmits using a only its own subcarriers, to avoid collision

In the multiple-access case, 1024 subcarriers are considered and 256 subcarriers are assigned to each user. Therefore, the bandwidth assigned to each ONU is 2.5 GHz, but it can be flexibly changed according to the DBA protocol.

To allow different operators to transmit independently, the OFDM signals from each user are combined together in the optical domain, using a 4:1 combiner. This is a key feature of the proposed approach, with respect to conventional OFDM-based systems, because this scheme allows the network operators to use their own equipment in the CO. The system complexity is transferred into the digital domain, because each ONU performs a 1024 point FFT, but it transmits only on 256 subcarriers, filling the other subcarriers with zeros pads. Only two sub-carrier is used for frequency guard band.

An additional AWG device can be included in the case that the proposed system is extended to an hybrid WDM-OFDM case [20] or to accomplish with the TWDM standard.

2.3.3 Performance evaluation

Numerical simulations have been performed with Matlab and VPIPhotonics [21] co-simulator and system performances are evaluated in terms of error vector magnitude (EVM) and the bit error rate (BER) [22].

In order to validate the PON system simulator, it is first consider a back-to-back (P2P) configuration, with only additive white Gaussian noise; Figure 2-9(a) shows the BER versus the EVM for a 10Gb/s system, and we observe a good agreement with the theoretical curves evaluated as [23]:

$$BER = \frac{2 \left(1 - \frac{1}{L}\right)}{\log_2 L} Q \left[\sqrt{\frac{3 \log_2 L}{L^2 - 1} \frac{2}{EVM^2 \log_2 M}} \right] \quad 2-11$$

where L is the number of levels in each dimension of the M -ary modulation system, and Q is the Gaussian co-error function. The forward error correction (FEC) limit ($BER=10^{-3}$) is achieved for EVM equal to -17 and -10 dB, for 16 and 4-QAM modulation, respectively.

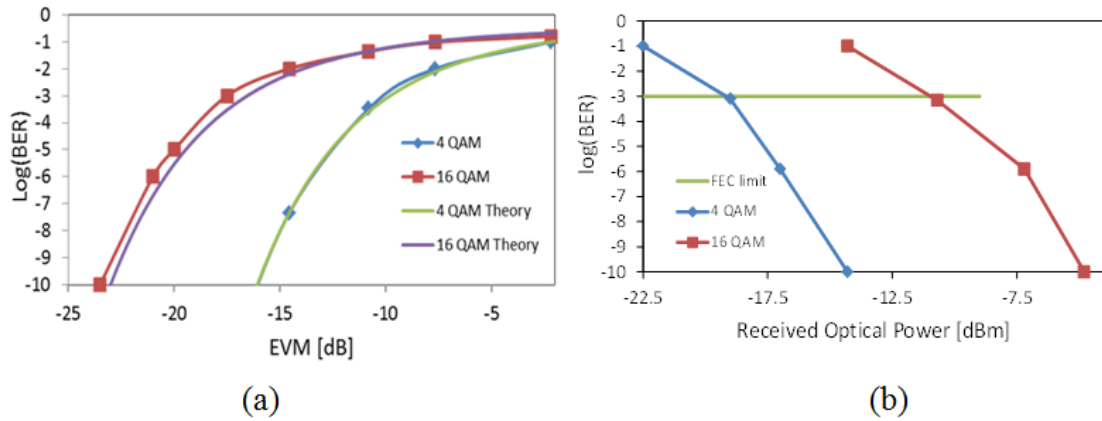


Figure 2-9: (a) BER versus EVM in a back-to-back configuration, (b) BER versus optical power received after 40 km for a 4-ONU system.

Then we consider a P2MP configuration and the performances of the transmission over a 40 km-link are shown in Figure 2-9(b); in this case, the receiver sensitivities are -19 and -14 dBm for 4 and 16-QAM modulation, respectively.

Figure 2-10(a) shows the BER versus the EVM in a 4-ONU PON system, considering that all the ONUs are at a 55 km distance from the OLT. BER as a function of the received optical power for a 55 km link is shown in Figure 2-10(b);

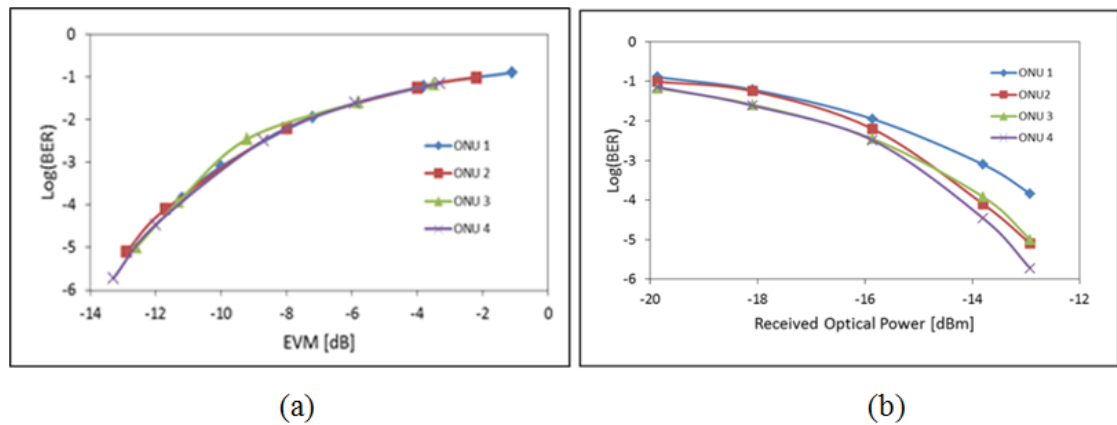


Figure 2-10: (a) BER versus EVM for a 4-user PON, (b) BER versus received optical power for a 4-user PON.

slightly different performances are observed for the four ONUs, due to chromatic dispersion effects. In the worst case (ONU1) the receiver sensitivity is -13.8 dBm. It is remark that no amplifiers or dispersion compensation techniques have been used. An simple and effective OFDM-based PON system is investigated for ULL in NGAN [24].

2.4 Access networks based on RSOA

In the previous section a OFDM-based PON was investigated numerically. There are at least two main disadvantage which limit the previous setup and they are: 1) Frequency offset originated from different CW laser source 2) ONU is not colorless.

Reflective semiconductor optical amplifier (RSOA) is proposed to be adopted in ONU for cost-effective WDM-PONs due to their advantage providing color-less access network, capability of monolithically integration, wide bandwidth of operation, low cost and power dissipation [25]. They simultaneously provide signal amplification and modulation. Therefore, customer ONU based on RSOA do not need a tunable CW source.

RSOA, as for SOA, is an optoelectronic device based on an active gain region surrounded by a lower refractive. External current provide the source for both amplification and modulation to take place. Because of the lower index surrounded the active region the signal must be well confined inside. If the optical signal confined is not perfect, noise will be added to the signal at the output of the RSOA. The input signal enter the RSOA device from the input anti-reflected (AR) facet. The amplified and modulated output signal is reflected from the high-reflected (HR) RSOA facets as shown in Figure 2-11. The input signal provided by the OLT is usually called seed signal.

The optical amplification and modulation in RSOA can be explained by a classical two-level system of the active region where three radiative mechanisms are possible: 1) spontaneous emission 2) stimulated emission and 3) stimulated absorption.

The stimulated absorption is a loss process because the incident photon is stimulating a carrier from the valence band to the conduction band.

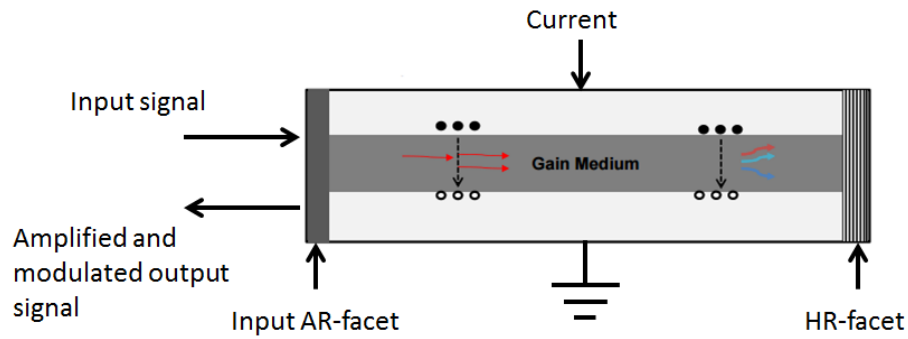


Figure 2-11: Schematic diagram of an SOA.

If a photon of light with energy equal to the band-gap of the active region is incident on the device, it can cause stimulated recombination of the electron-hole pair. Through this recombination process, the carrier loses its energy in the form of a photon of light. The recombination process generates a photon with the same frequency and phase as the incident photon. Stimulated emission is the necessary positive gain mechanism to operate, and happen only when the number of carriers in the conduction band exceeds that of the valence band, called population inversion. In this case, the likelihood of stimulated emission is greater than stimulated absorption and the device will exhibit optical gain if the injected current is sufficiently high.

Spontaneous emission process take place because there is a non-zero probability per unit time that a carrier from the conduction band can spontaneously recombine with a hole in the valence band emitting a photon with random phase and direction.

The proposed PON based on RSOA device is shown in Figure 2-12. At the OLT an adaptive OFDM based on Hermitian symmetry is used to obtain a real signal called discrete multitone (DMT). DMT is already used in xDSL due to its propriety of providing high capacity transmission, very good system performance and high degree of flexibility. Using DMT the number of bits assignment on each subcarrier vary as a function of the SNR per subcarrier, i.e, a high modulation format (more bits per subcarrier) is used for a high SNR and low modulation format is used for a low SNR. In this case rate-adaptive modem are obtained.

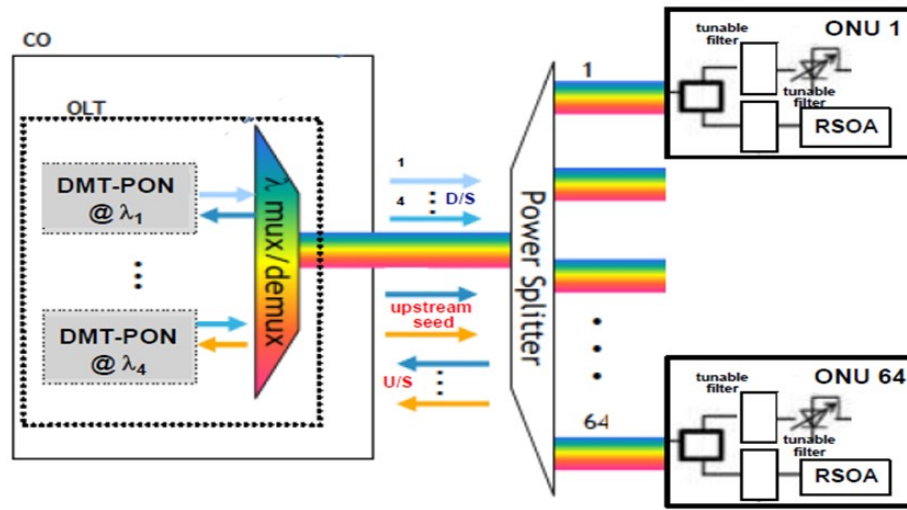


Figure 2-12: DMT-PON based on RSOA.

The proposed DMT-PON (WDM) is based on four wavelengths used at the OLT with each wavelength carrying at the up-stream at least 16 Gb/s for 16 ONU. This implies 1 Gb/s for ONU in up-stream which is the requirements for the next generation optical access networks (NG-PON2) and a total of 64 ONU for a total capacity of 64 Gb/s. At the OLT 4 different operators can use each one wavelength. The multiplexing of the wavelengths is performed by an AWG. In addition, each operator will also send the seed CW light source which will provide the carrier for the up-stream modulation data. At the remote node a power splitter with 64 output ports is used to split the energy at each ONU. No optical amplification is used. At the ONU a circulator is then used to separate the modulated DMT optical signal from the seed CW source. The circulator can even prevent any optical signal generated for example from Rayleigh backscattering back-scattering effect. Optical tunable filters must be used for the selection of different wavelength. Each ONU will be provided by a RSOA which basically works like an intensity modulators with addition of optical signal amplification. The desired seed is selected by the tunable filter and will be used for the up-stream transmission. At the ONU a DMT digital signal is generated to overcome the RSOA bandwidth limitations. For downstream scenario four pairs of wavelengths should support 32Gb/s each for a total of 128Gb/s. In case of equal ONU a capacity of 2Gb/s for each ONU is achieved if the

symbol rate is 500Mb/s with 16-QAM modulation. The setup proposed in Figure 3-43 offer the following advantage: 1) compliance with NG-PON2 2) increased capacity for both down-stream and up-stream 3) narrower transmission bandwidth which impact on optical filtering 4) no DBA algorithm as for TDM but simple medium access control (MAC) 5) unbundling the local loop by introducing other operators (OLO) maintaining the same NG-PON2 requirements as for a single ONU.

2.4.1 RSOA model

Numerically modelling of SOA has been a hot topic for two decades and it is based on two main approach. One which is based on time domain signal propagation including also the carrier density in time [29] and the other based on a more simplify model using ordinary differential equation [33]. In case of RSOA this consist on simulating a couple of partial differential equation. Simplified analytical models of RSOA can be found in [35].

The basic rate equation that govern the propagation inside RSOA are now derived based on the analysis in [39].

To derive the wave equation for the propagation of electromagnetic field inside RSOA simple calculation is given. First it is supposed the medium is linear, isotropic, homogeneous with no charge. The Maxwell-Faraday equation is written simply as:

$$\nabla \times \mathbf{E} = -\frac{\partial \mathbf{B}}{\partial t} \quad 2-12$$

where \mathbf{E} is the electric field and \mathbf{B} magnetic flux. Taking the curl of Eq. 2-9 and using the curl of the curl identity $\nabla \times \nabla \times \mathbf{X} = \nabla(\nabla \cdot \mathbf{X}) - \nabla^2 \mathbf{X}$ it is obtained the following relation:

$$\nabla^2 \mathbf{E} = \mu_0 \sigma \frac{\partial \mathbf{E}}{\partial t} + \mu_0 \epsilon_0 \frac{\partial^2 \mathbf{E}}{\partial t^2} + \mu_0 \frac{\partial^2 \mathbf{P}}{\partial t^2} \quad 2-13$$

where \mathbf{P} is the electric polarization field, σ is the conductivity, ϵ_0 and μ_0 the vacuum permittivity and permeability, respectively.

Working with phasors in Eq. 2-13 the desired wave equation is obtained as in [33]:

$$\nabla^2 \mathbf{E} - \frac{\epsilon}{c^2} \frac{\partial^2 \mathbf{E}}{\partial t^2} = 0 \quad 2-14$$

The dielectric constant is given as: $\varepsilon = n_b^2 + \chi$ where χ is the susceptibility and $n_b^2 = 1 + \chi_0$ is the background refractive index. χ_0 is the susceptibility of the material when no injected current is present in active region of the RSOA. To include the linewidth enhancement factor, α , the susceptibility χ is modified as in [33] with the following relation which include the linear dependence from the carrier density:

$$\chi = -\frac{\bar{n}\omega_0}{c}(\alpha + i)a(N - N_0) \quad 2-15$$

To further simplify Eq. 2-10 we supposed a single waveguide mode propagation and the input electrical field is linearly polarized. The complex electrical field can be written as:

$$\mathbf{E}(x, y, z, t) = \hat{x}\{F(x, y)A(z, t)e^{ik_0z - i\omega_0t}\} \quad 2-16$$

where \hat{x} is the polarization unit vector, $F(x, y)$ is the wave-guide mode distribution, $A(z, t)$ is the slowly-varying complex envelope, $k_0 = \bar{n}\omega_0/c$ is the wavenumber with \bar{n} the effective mode index, N is the carrier density, N_0 is the carrier density require for transparency and a is the differential gain. Eq. 2-16 is substituted in Eq. 2-14, integrated over x and y with a second order derivate terms not taken into account because the envelope is assumed that vary slowly; then the following equation are obtained:

$$\frac{\partial^2 F(x, y)}{\partial x^2} + \frac{\partial^2 F(x, y)}{\partial y^2} + (n_b^2 - \bar{n}^2)\frac{\omega_0}{c}F = 0 \quad 2-17$$

$$\frac{\partial A^\pm}{\partial z} \pm \frac{1}{v_g} \frac{\partial A^\pm}{\partial t} = \pm \frac{g(1 - i\alpha)A^\pm}{2} \mp \frac{\alpha_{int}}{2}A^\pm \quad 2-18$$

where α_{int} is the RSOA internal loss, A^+ and A^- are the complex envelope of the forward and backforward propagation in the RSOA, respectively. The gain coefficient is denoted by:

$$g = \frac{\Gamma a(N - N_0)}{1 + \epsilon(|A^+|^2 + |A^-|^2)} \quad 2-19$$

with Γ the confinement factor and ϵ gain saturation which take into account the mutual effect between forward and backward propagation. These equation neglect ultrafast gain non-linearity and spectral hole-burning [40]. The solution of Eq. 2-17 provide the

effective mode index and the transverse distribution. Eq. 2-18 governs the complex envelope propagation along the RSOA length.

The carrier density rate obeys the following simplify rate equation:

$$\frac{\partial N}{\partial t} = \frac{I}{qV} - \frac{N}{\tau_c} - \frac{a(N - N_0)}{hf_0} - R(N) \quad 2-20$$

where I is the injection current, q is the electron charge, V is the active region volume, τ_c is the carrier lifetime, h is the Plank constant and $f_0 = \omega_0/2\pi$ is the signal optical frequency. $R(N)$ is the recombination rate equal to $AN + BN^2 + CN^3$ where A is the nonradiative recombination, B is the bi-molecular radiative recombination and C the Auger recombination coefficient.

The complete rate equation describing the lightwave propagation inside RSOA is given by Eq. 2-20, Eq. 2-19 and Eq. 2-18. To avoid time-consuming numerical simulations, the gain coefficient g is assumed constant within two different numerical values. Therefore g becomes linear and Eq. 2-18 can be solved analytically by making the following transformation:

$$\tau = t - \frac{t}{v_g} \quad 2-21$$

where τ is a reduced time measured in a reference frame moving with the pulse. With this transformation Eq. 2-18, after simple manipulation, is then written for the forward envelope as:

$$A^+[nT + T, mZ + Z] = A^+[nT, mZ] e^{\left(\frac{g[nT, mZ] \cdot (1 - i\alpha) - \alpha_{int}}{2}\right)Z} \quad 2-22$$

with $T = Z/v_g$, $n = 0, 1, \dots$, $m = 0, 1, 2, \dots, M - 1$, and $M = L/Z$ where L is the active region length of RSOA. T and Z represent the step size on time t axis and z axis, respectively. Backward envelope is then written as:

$$A^-[nT + T, mZ - Z] = A^-[nT, mZ] e^{\left(\frac{g[nT, mZ] \cdot (1 - i\alpha) - \alpha_{int}}{2}\right)Z} \quad 2-23$$

Eq. 2-22 and Eq. 2-23 are both now expressed in a discrete form. Eq. 2-20 and Eq. 2-19 is also discretized and written as:

$$\begin{aligned} \frac{N[nT + T, mZ] - N[nT, mZ]}{Z} \\ = \frac{I[nT]}{qV} - \frac{N[nT, mZ]}{\tau_c} - \frac{a(N[nT, mZ] - N_0)}{hf_0} - R[nT] \end{aligned} \quad 2-24$$

$$g[nT, mZ] = \frac{\Gamma a(N[nT, mZ] - N_0)}{1 + \epsilon(|A^+[nT, mZ]|^2 + |A^-[nT, mZ]|^2)} \quad 2-25$$

The boundary condition for $m = M - 1$ are imposed on RSOA rear facet in the active region and given as:

$$A^-[nT + T, mZ] = \sqrt{R_2}g[nT, mZ - Z]A^+[nT, mZ - Z] \quad 2-26$$

with R_2 the rear facet power reflectivity.

The boundary condition for $m = 0$ are imposed on RSOA front facet in the active region and given as:

$$A^+[nT + T, 0] = \sqrt{R_1}g[nT, 0]A^-[nT, 0] + \sqrt{1 - R_1}A_{inp}[nT + T, 0] \quad 2-27$$

with R_1 the front facet power reflectivity and A_{inp} input signal in the RSOA. The output signal is given as:

$$A_{out}[nT + T, 0] = \sqrt{1 - R_1}g[nT, 0]A^-[nT, 0] \quad 2-28$$

Summarizing, the numerical model for simulating the propagation of complex envelope inside RSOA consist of Eq. 2-22 and Eq. 2-23 which describe the forward and backforward propagation, respectively; Eq. 2-24 and Eq. 2-25 describe the carrier density rate and gain coefficient, respectively. Eq. 2-26 and Eq. 2-27 are the boundary condition imposed on the RSOA facet and Eq. 2-28 is the output signal.

2.4.2 Bit and power loading

The performance of up-stream DMT-PON strongly depend on RSOA frequency response and are governed by the subcarriers who show the lowest SNR. To overcome the RSOA bandwidth limitation algorithm which perform bit and power loading are needed to optimize the transmission performance. In up-stream scenario, where adaptive OFDMA is performed, the dynamic algorithm should also assign the subcarriers to each ONU in order to provide them with 1 Gb/s data rate required by the NG-PON2.

The maximum achievable bit rate is given by the well know Shannon formula for bandlimited channels with white Gaussian noise (AWGN) as [41]:

$$\frac{C}{B} = \log_2(1 + SNR) \quad 2-29$$

where C is the capacity, B is the channel bandwidth and SNR is the signal-to-noise ratio. In real system there is a gap constant, Γ , which limit the maximum achievable bit rate given as:

$$\frac{R}{B} = \log_2 \left(1 + \frac{SNR}{\Gamma} \right) \quad 2-30$$

where R is the bit rate. The gap Γ , is the difference between the channel capacity, C , and the achievable bit rate R . The gap Γ , for uncoded QAM constellation is given as [42]:

$$\Gamma = \frac{1}{3} \left(Q^{-1} \left(\frac{SER}{4} \right) \right)^2 \quad 2-31$$

where SER is the symbol error rate and $Q^{-1}(\cdot)$ is the inverse Q function defined as:

$$Q(x) = \int_x^{+\infty} \frac{e^{-u^2/2}}{\sqrt{2\pi}} du \quad 2-32$$

Figure 2-13 shows the maximum achievable bit rate as a function of various gap values. In bit loading algorithm for DMT system the number of bits for a particular gap is usually given as:

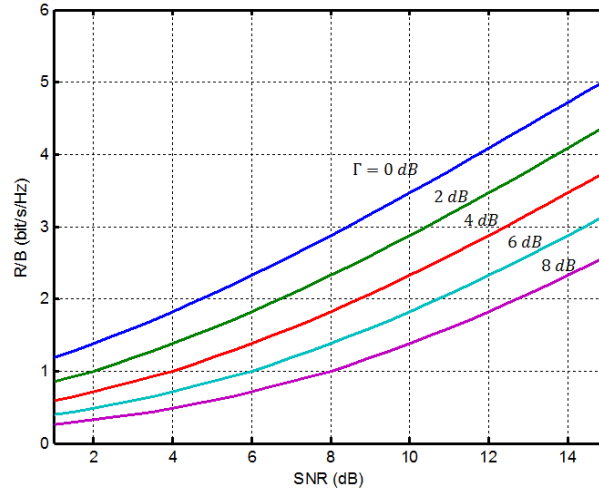


Figure 2-13: Achievable bit rate as a function of SNR (dB) for different value of the gap Γ .

$$b = \log_2 \left(1 + \frac{SNR}{\Gamma} \right) \quad 2-33$$

where b is the number of allocated bit for each subcarrier. Eq. 2-31 is a very good approximation for both square and cross constellation. For instance, for 16-QAM at a BER equal to 10^{-3} a gap of $\Gamma = 3.18$ is found. The relation between BER and SNR for both square and cross constellation is given approximately as [43]:

$$BER = Q \left(\sqrt{\frac{3}{M-1} SNR} \right) \quad 2-34$$

2.4.2.1 Water filling algorithm

The OFDM signal consist of a set of parallel N subchannels transmitted on N parallel channels. To maximize the total bit rate, $R = b/T$ with $1/T$ fixed symbol rate, requires the maximization of achievable bit, $b = \sum_{n=0}^{N-1} b_n$, over b_n number of bits per subcarrier and transmitted power per subcarrier P_n . Thus, the aggregated bit rate R is divided unequally among all the subcarriers [44], with a bit rate per subcarrier $R_n = b_n/T$. When maximizing the number of bit, a constant power constrain is also imposed, given both as:

$$Max: b = \sum_{n=0}^{N-1} b_n = \sum_{n=0}^{N-1} \log_2 \left(1 + \frac{P_n |H_n|^2}{\Gamma \sigma_n^2} \right) \quad 2-35$$

$$with \text{ power constrain: } P_T = \sum_{n=0}^{N-1} P_n \quad 2-36$$

where H_n is the channel gain, σ_n^2 is the noise variance and P_n transmitted power per subcarrier. If the received symbol, in frequency domain is approximated as $Y_n \approx H_n X_n$ then the signal to noise ratio of the received subcarrier is $SNR_{Y,n} = |H_n|^2 SNR_{X,n} = P_n |H_n|^2 / \sigma_n^2$. Using Langrange multipliers and differentiating with respect to P_n the solution to Eq. 2-11 is found known as the water filling solution:

$$P_n + \frac{\Gamma \sigma_n^2}{|H_n|^2} = a \quad 2-37$$

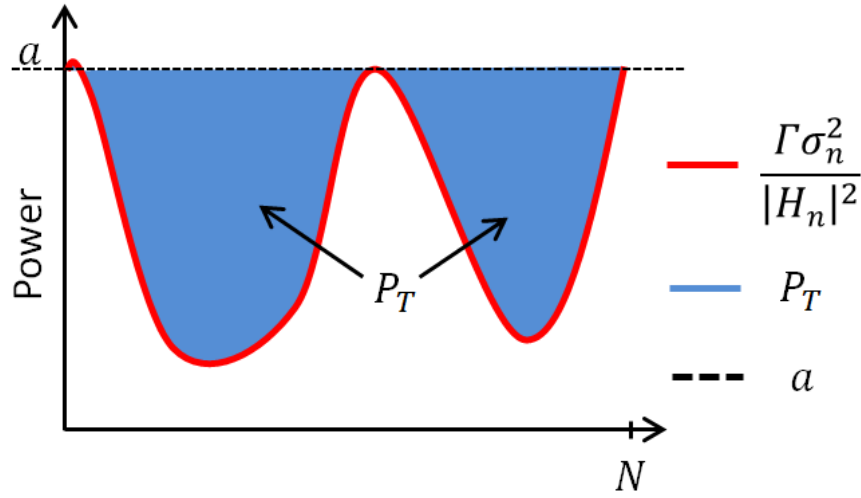


Figure 2-14: Optimal power allocation with water filling solution.

where a is a constant. Then the power on each subcarrier must be chosen such that $P_n = a - \Gamma \sigma_n^2 / |H_n|^2$ with the ‘water-level’ a constrain to Eq. 2-12. The optimum power allocated is shown schematically in Figure 2-14. This is called water filling solution because the solution show graphically a curve (or bowl) of inverted SNR_n scaled by the gap, $\frac{\Gamma \sigma_n^2}{|H_n|^2}$, being filled with power (water) to a constant flat level a . After the optimal power allocation the number of bits per each subcarrier is find using Eq. 2-35. This is also known as rate adaptive approach because the number of bit for each subcarrier may vary without any constrain. In many application there is needed to minimize the total power with the constrain of fixed data rate. This gives two equation to solve as:

$$\text{Min: } P_T = \sum_{n=0}^{N-1} P_n \quad 2-38$$

$$\text{with constrain } b: b = \sum_{n=0}^{N-1} \log_2 \left(1 + \frac{P_n |H_n|^2}{\Gamma \sigma_n^2} \right) \quad 2-39$$

Same water-filling solution is found as in Eq. 2-37. This is known as power minimization. The power/water is allocated to each subcarrier until the fixed bit rate is reached.

2.4.2.2 Levin-Campello algorithm

Previous water filling algorithm can give non-integer value bit distributions b_n which are difficult to realize in real systems. Two different alternative algorithm are proposed in literature which provides an integer number of bit distribution. These are suboptimal algorithms which approximate the water-filling solution.

The first algorithm is based on an approximation of water-filling results by rounding the bit distribution, and is called Chow's algorithm. The algorithm rounds the non-integer number to the nearest integer [45].

The second algorithm is based on greedy optimization and is proposed by Levin and Campello [46]. The idea is to increase the number of bits on each subcarrier which require least incremental energy for transmission by a unit of information, which in case of M-QAM modulation is equal to 1. According to the SNR per subcarrier the algorithm calculates the optimum bit and power distribution. There are three important definitions for the Levin Campello algorithm, the incremental energy per subcarrier, the efficiency of the bit distribution and E-tightness.

The incremental energy to transmit b_n information bits on the subcarrier is the amount of additional energy required to transmit one more information unit. The incremental energy is then:

$$I_n(b_n) = E_n(b_n) - E_n(b_n - \beta) \quad \text{Eq. 2-40}$$

where E_n is the energy per subcarrier and β is the information unit. For QAM constellation we can assume $\beta = 1$. In general I_n is related to the gap for any value of β as:

$$I_n = \frac{\Gamma \sigma_n^2}{|H_n|^2} 2^{b_n+1} (2^\beta - 1) \quad \text{Eq. 2-41}$$

A bit distribution b_n is said to be efficient among other possible distributions if:

$$\max[E_n(b_n)] \leq \min[E_m(b_{m+\beta})] \quad \text{Eq. 2-42}$$

which simply means that by adding an additional information unit in one subcarrier taken from another subcarrier there is no loss in the total symbol energy because the left side of Eq. 2-42 is assumed smaller than the right side and hence efficiency in bit distribution is achieved.

A bit distribution is said to be E-tightness if:

$$0 \leq N\bar{E} - \sum_{n=0}^{N-1} E_n(b_n) \leq \min_{0 \leq i \leq N-1} [I_n(b_n + \beta)] \quad \text{Eq. 2-43}$$

where \bar{E} is the average transmitted energy. Eq. 2-43 implies that no additional information is transmitted without violating the total energy constrain. This is very useful for algorithm which maximize the bit rate under some power constrain.

This algorithm is used to evaluate the performance of the proposed DMT-PON to maximize the total bit rate when RSOA device is on the ONU side.

2.4.3 RSOA characterization

To evaluate the DMT-PON performance in up-stream it is consider a fixed fiber length with a varying incident optical power from the OLT side. The setup of DMT –PON was shown in Figure 2-12. A co-simulation between Matlab and VPI-Photonics is used for all performance evaluation. A characterization of the RSOA device used in the DMT-PON is first performed by comparing both VPI-Photonics results with the numerical result given in section 2.4.1 where the partially equation are numerically solved. VPI-photonics circuit to characterize the RSOA device is shown in Figure 2-15.. A driving sinusoidal signal is used to bias the RSOA with a VPI Driving-Module which control the peak-to-peak amplitude and the frequency of the current.

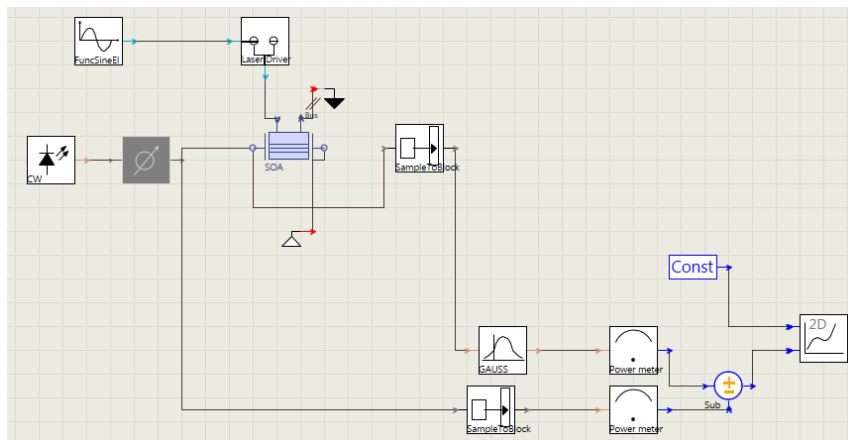


Figure 2-15: VPI-photonics circuit build for RSOA characterization.

name:	value	Unit	type
Device Structure			
DeviceSectionLength	300e-6	m	S
ActiveRegionType	Bulk		S
ActiveRegionWidth	1.5e-6	m	S
ActiveRegionThickness	270e-9	m	S
CurrentInjectionEfficiency	1.0		S
Optical Parameters			
NominalFrequency	SampleModeCenterFrequency	Hz	S
EffectiveIndex	0.0		S
GroupIndex	3.7		S
PolarizationModel	Isotropic		S
InternalLoss	3000.0	1/m	S
InternalLossCarrierDepe...	0.0	m ²	S
ConfinementFactor	0.45		S
OpticalCouplingEfficiency	1.0		S
InterfaceReflectionCoef...	1.0e-5 0.9		S
InterfaceReflectionPhas...	180.0 0.0	deg	S
InterfaceTransmissionPh...	0.0	deg	S
DeviceSectionPhaseShift	0.0	deg	S
Nonlinear Parameters			
Gain Parameters			
GainShapeModel	Parabolic		S
GainModel	Linear		S
GainCoefficientLinear	3e-20	m ²	S
GainPeakFrequency	0	Hz	S
GainBandwidth	1e13	Hz	S
CarrierDensityRefGainS...	2.0e+24	1/m ³	S
ParabolicGainShapeFitting	FirstOrderIIR		S
NonlinearGainCoefficient	1.0e-23	m ³	S
NonlinearGainTimeconstant	500e-15	s	S
Carrier Dynamics			
Chirp Parameters			
Spontaneous Emission			
NoiseModel	InversionParameter		S
InversionParameter	2.0		S
NoiseCenterFrequency	0	Hz	S
NoiseFrequencyCarrierD...	0.0	Hz ...	S
NoiseBandwidth	10e12	Hz	S
NoiseBandwidthCarrierD...	0.0	Hz ...	S
Numerical			
Visualization			

Figure 2-16: VPI-Photonics RSOA parameter.

A variable optical attenuator is put in front of the RSOA in order to vary the CW power. The RSOA output is then filter by an optical Gaussian band pass filter (OBPF) and measured in a power meter module. The RSOA parameter are listed in Figure 2-16 and most of them are taken from [47]. The RSOA investigated contain bulk active medium, with cavity length $L = 300 \cdot 10^{-6}$ (m), $w = 1.5 \cdot 10^{-6}$, $d = 270 \cdot 10^{-9}$ (m), $\Gamma = 0.45$, initial carrier density $= 3 \cdot 10^{24}$ (1/m³), inversion parameter $= 2$ and differential gain $= 3 \cdot 10^{-20}$ (m²). The noise model included in VPIPhotonic is determined by the inversion factor, η_{SP} , which in general is proportional to the noise figure (NF). Its value is given as:

$$\eta_{SP} = \frac{N}{N - N_0} \quad \text{Eq. 2-44}$$

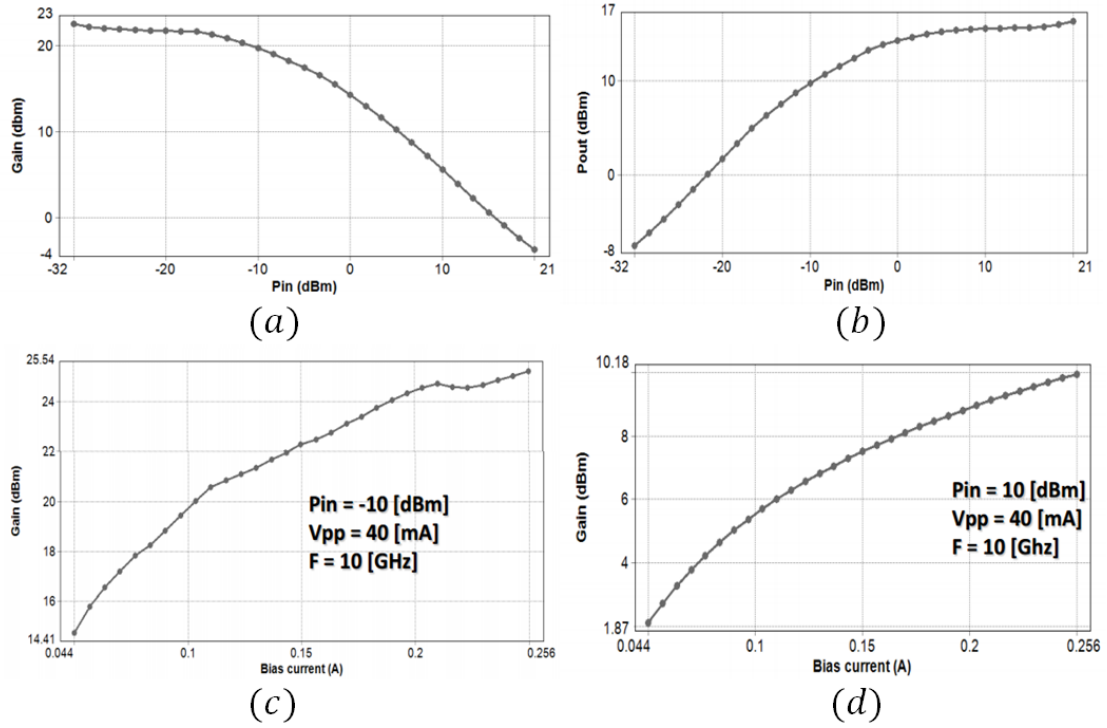


Figure 2-17: Numerical results. (a) Optical gain versus the input optical power with a fixed bias current of 40mA. (b) Output power versus the input optical power. (c) Optical gain versus the driving bias current for optical input power of -10 dBm. (d) Optical gain versus the bias current for an optical input power of 10 dBm.

with $\eta_{SP} = 1$ for a total population inversion leads to the quantum limit value equal to $NF = 3\text{dB}$. In simulation η_{SP} is 2 which leads to a noise figure $NF = 6\text{dB}$.

A 10 GHz sinusoidal electrical driving current with a peak to peak amplitude of 40 mA is used to have comparative result with the results presented in [47]. Figure 2-17(a) show the optical gain versus the optical input power where the gain saturation, as expected, is obtained. Figure 2-17(b) show the output power versus the input optical power. Figure 2-17 (c) show the optical gain versus the bias current for an input optical power of -10 dBm. In Figure 2-17(d) is shown the optical gain versus the bias current when the input power is 10dBm where as expected a strongly saturated gain is obtained. Using the same RSOA parameter Matlab numerical simulation results are shown in Figure 2-18. The power noise is also included with the ASE power spectral density given as:

$$P_{ASE} = \eta_{SP}(G - 1)h\nu B_{sim} \quad 2-45$$

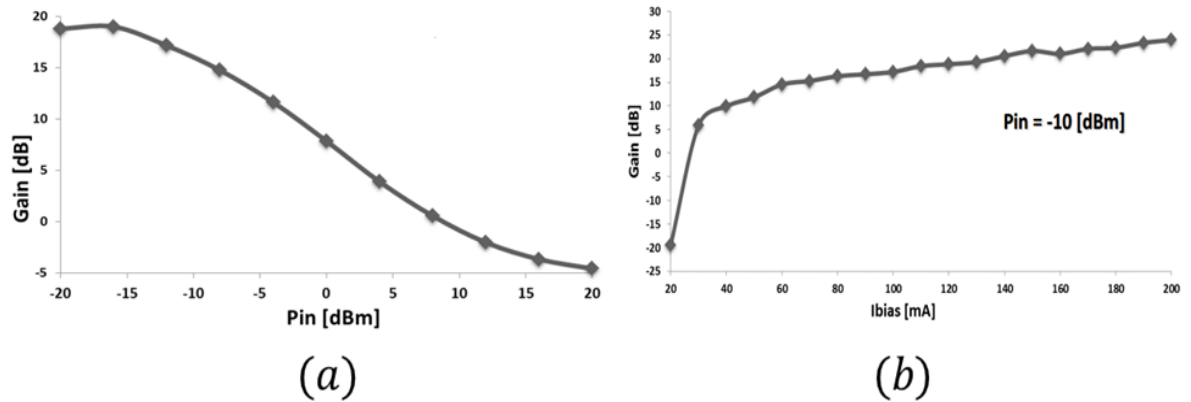


Figure 2-18: Matlab results. (a) Optical gain versus the input optical power. (b) Optical gain versus the bias current.

where B_{sim} is the simulation bandwidth and G is the single pass gain. The spontaneous emission will have so two contribution; one from the spontaneous emission in section Z and the input noise amplified.

Although the results are not identical they show very similar behavior confirming both m Matlab and VPIPhotonic models with experimental results presented in [47].

Commercial RSOA device have limit electro-optical bandwidth between 1 and 2 GHz [50]. This is due to a long carrier lifetime which depend on the combination between high carrier density and low photon density.

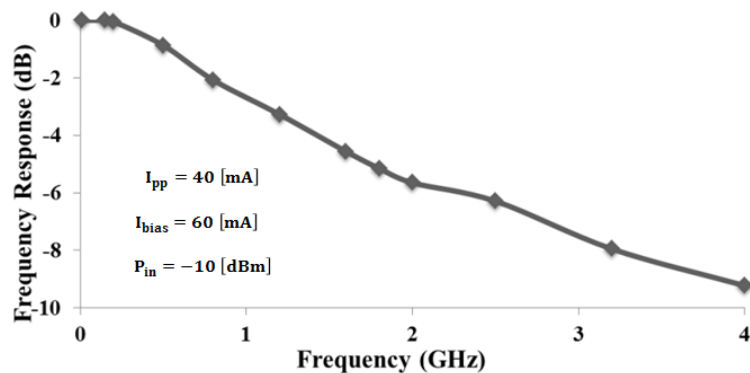


Figure 2-19: RSOA frequency response.

Even the absence of a cavity in RSOA limits the modulation speed of the device. In Figure 2-19 is shown the modulation frequency response of the RSOA. As observed, the bandwidth at 1.2 GHz show a modulation frequency response of -3 dB.

2.4.4 Performance evaluation

To test the proposed DMT-PON based approach only one wavelength is considered for up-stream scenario originated from 16 ONU as was shown in Figure 2-12. The transmission system parameter are listed in Table 2-1. Each ONU generate pseudo-random data, preamble for channel equalization, an IFFT of 256 point with 96 used subcarrier

Table 2-1: Transmission parameters.

OFDM DSP Parameters	Value	Unit
IFFT/FFT	256	
Virtual subcarriers	20%	
Used subcarriers	96	
Subcarrier bandwidth	49.8	MHz
Cyclic prefix	3%	
Adaptive modulation	BPSK/4-QAM/16-QAM/32-QAM/64-QAM	
DAC/ADC sampling rate	4	GS/s
DAC/ADC resolution	6	bits
Bessel Filter	8	GHz
Fiber Parameter		
Dispersion	17	ps/nm/km
Slope	0.07	ps/nm ² /km
Loss	0.2	dB/km
Non-linear effect	1.3	1/(W·km)
Effective area	80	μm^2
APD		
Quantum efficiency	0.8	
Thermal noise	10^{-12}	A/Hz ^{1/2}

with adaptive bit and power loading. The IFFT will generate a real signal because it is arranged in order to satisfy the Hermitian symmetry. Subcarrier bandwidth is 49.8 MHz. The base-band real signal DMT generated from a DAC with 6 bit resolution is then low pass filter to account for bandwidth limitation. The DMT signal is combined with an optimum bias current equal to $I_{bias} = 150[mA]$ and directly modulate the seed source provided by the OLT on a 1.2 GHz RSOA device. For a trade of saturation power, gain and modulation bandwidth a length of RSOA cavity equal to $300\mu m$ is chosen. The signal is then transmitted on 25 km single mode fiber without any optical amplification. At the receiver (OLT) the signal is received with an APD and low pass filter with a Bessel filter of 8 GHz to account for both photodiode and ADC bandwidth limitation. After signal synchronization and CP removed the FFT is taken to recover the transmitted symbol after channel equalization. The EVM is then used to measure the BER using 2-11 and to estimate the SNR per each subcarrier with the result used as input for Levin Campello algorithm. Only one RSOA is used due to high computational complexity if 16 RSOA are used in parallel. The distance from each ONU to the OLT is assumed the same. The VPIPhotonic setup to simulate the up-stream scenario is shown in Figure 2-20.

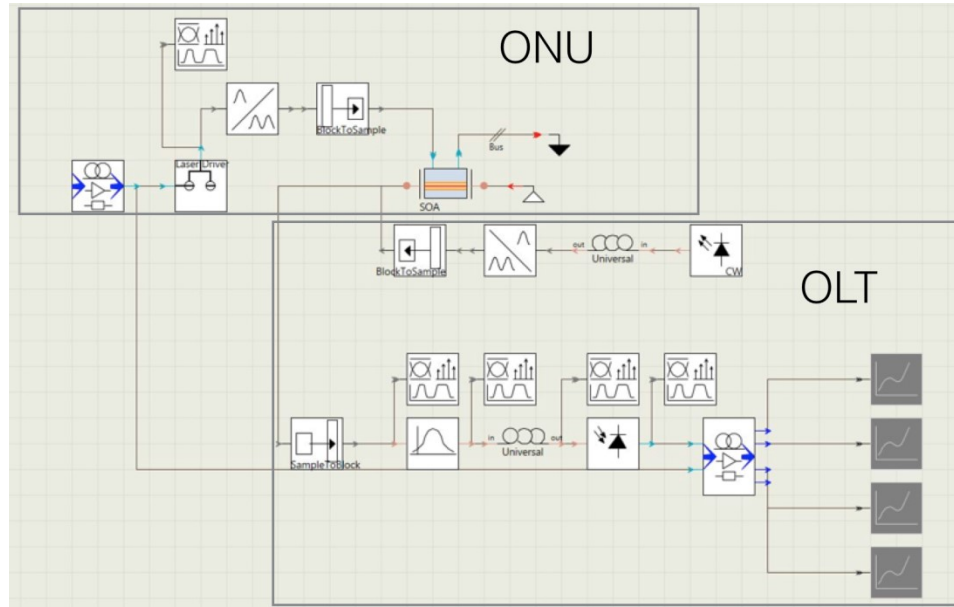


Figure 2-20: VPIPhotonic up-stream simulated setup.

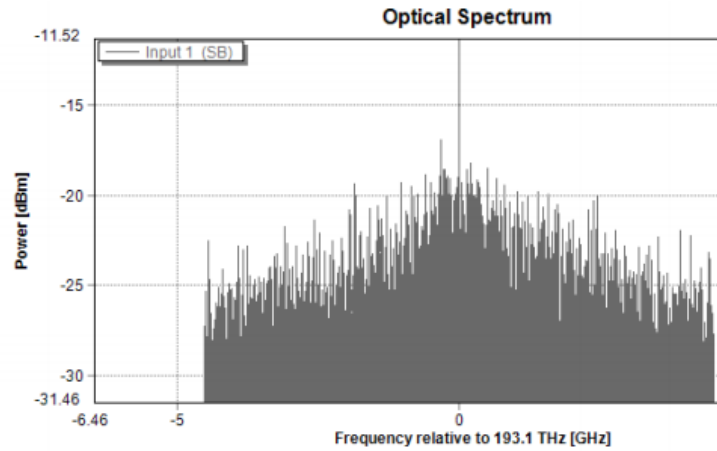


Figure 2-21: Received optical spectrum.

Different VPI blocks are used to measure the optical and electrical spectrum, to emulate the fiber, RSOA, optical and electrical filters and additional module for RSOA input/output and Matlab interface. Ad hoc Matlab code is implemented to be compatible with VPI software device.

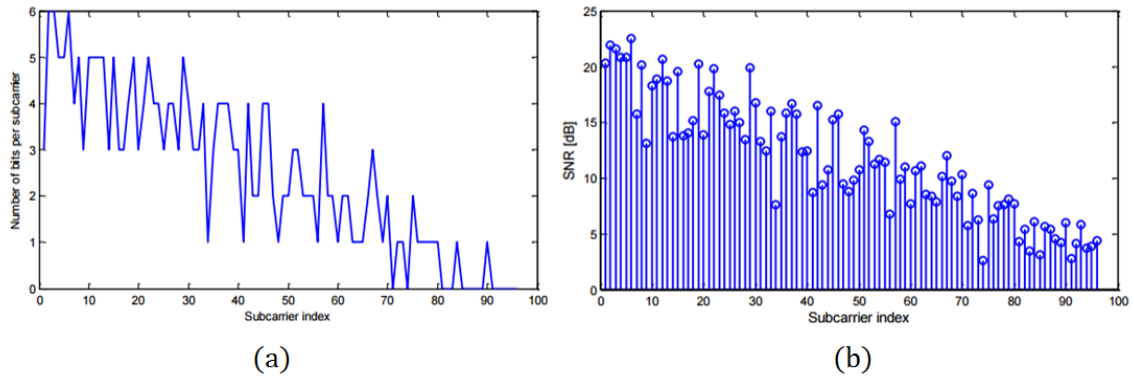


Figure 2-22: (a) Number of bits versus the subcarrier index, (b) estimated SNR versus the subcarrier index.

The received optical spectrum is shown in Figure 2-21 with a symbol rate equal to 6.24GHz. Figure 2-22(a) show the numer of bits estimated from the LC algorithm,

assigned for each subcarrier, based on the estimated SNR shown in Figure 2-22(b) for an input optical power in RSOA of 0dBm.

Figure 3-43(a) show the capacity (of 16 ONU) achieved using the LC algorithm and chromatic dispersion compensation versus the input power fed to RSOA device at a BER = 10^{-3} . The capacity is mainly limit by the in-band ASE noise generated from the RSOA and residual chirp. From this graph it is observed that in order to achieve 34Gb/s total capacity a RSOA input optical power of more than -10dBm is needed. In order to increase more the capacity we need to increase more the bandwidth of RSOA. With this solution 2Gb/s data is provided for each ONU in up-stream. Figure 3-43(b) show the capacity as a function of the fiber length. If the target data rate for up-stream is 1Gb/s per ONU a length of 45km fiber is possible to achieve. Power penalty less than 0dBm is obtained from back-to-back and after 25 km due to high resilient OFDM to chromatic dispersion effect. To also satisfy the power budget requirements an APD is used at the OLT with a receiver sensitivity of -28dBm at a BER = 10^{-3} [51]. To further enhance the receiver sensitivity of about 7 dB an optical filter can be used in front of the RSOA device as in [52].

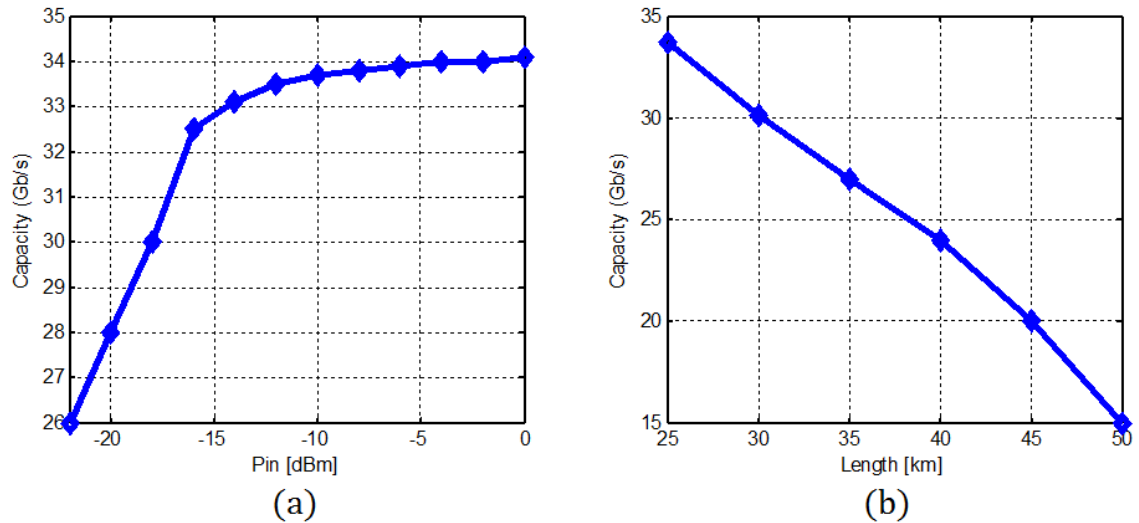


Figure 2-23: (a) Capacity versus RSOA input power, (b) capacity versus fiber length for input RSOA power of -10dBm.

2.5 Conclusions

WDM-PON is a promising approach for the future high-speed access networks with a high degree of flexibility. The use of WDM in long haul transmission is mature and their shift in the access networks is becoming challenging mainly due to their cost.

OFDM, which is very popular in wireless and wireline communications, has become recently the most potential candidate for the future high speed access networks providing data rate higher than 10Gb/s. This success is due to its high robustness against chromatic dispersion and chirp effects. OFDM shows less computational complexity if compared to single carrier transmission because of the frequency domain equalization employed. In this chapter was shown that the use of adaptive OFDM (named also DMT) in access networks can also fulfill the requirements of unbundling the local loop where different operators can transmit and receive on different assigned subcarriers.

To lower the cost of WDM-PON and to be compatible with the existing access network a DMT-PON is proposed using colorless RSOA device on each ONU. RSOA theory was briefly discussed and a simplified numerical differential equation is proposed for simulation. RSOA numerical simulation was compared against VPIphotonics results with very similar behavior.

Performance of the proposed DMT-PON was evaluated in up-stream scenario in case of a single wavelength and 16 ONUs. The RSOA bandwidth limitation was overcome by using Levin Campello algorithm to enhance the total capacity. Low cost RSOA with 1.2GHz bandwidth can provide 1Gb/s data for each ONU over more than 45km of single mode fiber.

The proposed architecture based on DMT-PON using RSOA shows a great potential for the next generation high speed networks.

References

- [1] J. von Hoyningen-Huene and C. Ruprecht, "OFDM for Optical Access," in Optical Fiber Communication Conference, OSA Technical Digest, paper Th1H.1.
- [2] N. Cvijetic, "OFDM for Next-Generation Optical Access Networks," in Journal of Lightwave Technology, vol. 30, no. 4, pp. 384-398, Feb.15, 2012.
- [3] W. Shieh, H. Bao, and Y. Tang, "Coherent optical OFDM: theory and design", Opt. Exp., vol. 16, no. 2, pp. 842-859, Jan. 2008.
- [4] A. J. Lowery, L. B. Du and J. Armstrong, "Performance of Optical OFDM in Ultralong-Haul WDM Lightwave Systems," in Journal of Lightwave Technology, vol. 25, no. 1, pp. 131-138, Jan. 2007.
- [5] G. Meslener, "Chromatic dispersion induced distortion of modulated monochromatic light employing direct detection", IEEE J. Quant. Electron. 20 (1984) 1208–1216.
- [6] M. Sieben, J. Conradi, D. Dodds, B. Davies, S. Walklin, 10 Gbit/s optical single sideband system, Electron. Lett. 33 (1997) 971–973
- [7] G.H. Smith, D. Novak, Z. Ahmed, "Novel technique for generation of optical SSB with carrier using a single MZM to overcome fiber chromatic dispersion" , in: Technical Digest 1996 International Topical Meeting on Microwave Photonics, 1996, MWP '96, 1996, pp. 5–8 suppl.
- [8] R.W. Chang, High-speed multichannel data transmission with bandlimited orthogonal signals, Bell Sys. Tech. J. 45 (1966) 1775–1796.
- [9] J.W. Cooley, J.W. Tukey, An algorithm for the machine calculation of complex Fourier series, Math. Comput. 19 (1965) 297–301.
- [10] S.B. Weinstein, P.M. Ebert, "Data transmission frequency-division multiplexing using the discrete Fourier transform" , IEEE Trans. Commun. Technol. 19 (1971) 628–634.
- [11] J.G. Proakis, "Digital Communications", McGrawHill Higher education, 2001.
- [12] L. Xiu, D. Qian, J. Hu, W. Wei and T. Wang, "OFDMA-based passive optical networks (PON)," in Proc. LEOSST 2008, pp. 159-160, paper TuE3.1.

- [13] D. Qian, J. Hu, P. Ji, T. Wang and N. Cvijetic, "10-Gb/s OFDMA-PON for delivery of heterogeneous services," in Proc. OFC/NFOEC 2008, pp. 1-3, paper OWH4.
- [14] <https://www.alcatel-lucent.com/solutions/vdsl2-vectoring>
- [15] P. Odling, B. Mayr, S. Palm, "The technical impact of the unbundling process and regulatory action," IEEE Comm. Magazine 38(5), 74–80 (2000).
- [16] S. Bregni, R. Melen, "Local loop unbundling in the Italian network," IEEE Comm. Magazine 40(10), 86–93 (2002). IEEE Std 802.1Q, 2003 Edition (2003).
- [17] M. Merka, "VULA, Virtual Unbundled Local Access, the Austrian Example," TNO DSL Seminar, June, 2012, The Hague, Netherlands.
- [18] W. Shieh and I. Djordjevic, OFDM for Optical Communications (Academic press, 2010).
- [19] B. J. C. Schmidt, A. J. Lowery, and J. Armstrong, "Experimental demonstrations of electronic dispersion compensation for long haul transmission using direct-detection optical OFDM," J. Lightw. Technol, vol. 26, pp. 196-203, 2008.
- [20] N. Cvijetic, M. Cvijetic, M. Huang, E. Ip, Y. Huang, T. Wang, "Terabit optical access networks based on WDM-OFDMA-PON" J. Lightw. Technol., vol. 30, no. 4, February 15, 2012.
- [21] <http://www.vpiphotonics.com/index.php>
- [22] H. A. Mahmoud., H. Arslan, "Error vector magnitude to SNR conversion for nondata-aided receivers", IEEE Trans. on Wireless Commun., vol. 8, no. 5, pp. 2694 - 2704 2009
- [23] R.A. Shafik, Md. S. Rahman, A. R. Islam, "On the extended relationship among EVM, BER and SNR as performance metrics", 4th International Conference on Electrical Computer Engineering ICECE, pp. 408-411, 2006
- [24] J. Hoxha, G. Zarra, G. Cincotti, "A flexible and spectrally efficient OFDM system for unbundling the local loop in optical access networks," 19th European Conference on Network and Optical Communications, NOC Milan, Italy, June 2014.
- [25] K. Y. Cho, Y. Takushima, and Y. C. Chung, "10-Gb/s operation of RSOA for WDM PON," IEEE Photon. Technol. Lett. 20(18), 1533–1535 (2008).

- [26] J. Prat, C. Arellano, V. Polo, and C. Bock, "Optical network unit based on a bidirectional reflective semiconductor optical amplifier for fiber to-the-home networks," *IEEE Photon. Technol. Lett.*, vol. 17, no. 1, pp. 250–252, Jan. 2005.
- [27] G. de Valicourt, C. Fortin, A. Enard, F. Van Dijk, and R. Brenot, "10 Gbit/s modulation of reflective SOA without any electronic processing," in *Proc. OFC*, Mar. 2011, pp. 1–3, paper OThT2.
- [28] P. Vetter, "Next generation optical access technologies," presented at the Eur. Conf. Exhib. Opt. Commun., Amsterdam, The Netherlands, 2012, Paper Tu.3.G.
- [29] T. Durhuus, B. Mikkelsen, and K. E. Stubkjaer, "Detailed dynamic model for semiconductor optical amplifiers and their crosstalk and intermodulation distortion," *J. Lightw. Technol.*, vol. 10, no. 8, pp. 1056–1065, Aug. 1992.
- [30] E. Zhou, X. Zhang, and D. Huang, "Analysis on dynamic characteristics of semiconductor optical amplifiers with certain facet reflection based on detailed wideband model," *Opt. Express*, vol. 15, no. 14, pp. 9096–9106, 2007.
- [31] M. J. Connelly, "Reflective semiconductor optical amplifier pulse propagation model," *IEEE Photon. Technol. Lett.*, vol. 24, no. 2, pp. 95–97, Jan. 15, 2012.
- [32] J. W. D. Chi, L. Chao, and M. K. Rao, "Time-domain large-signal investigation on nonlinear interactions between an optical pulse and semiconductor waveguides," *IEEE J. Quantum Electron.*, vol. 37, no. 10, pp. 1329–1336, Oct. 2001.
- [33] G. P. Agrawal and N. A. Olsson, "Self-phase modulation and spectral broadening of optical pulses in semiconductor laser amplifiers," *IEEE J. Quantum Electron.*, vol. 25, no. 11, pp. 2297–2306, Nov. 1989.
- [34] A. Mecozzi and J. Mørk, "Saturation induced by picosecond pulses in semiconductor optical amplifiers," *J. Opt. Soc. Amer. B*, vol. 14, no. 4, pp. 761–770, 1997.
- [35] C. Antonelli, A. Mecozzi, Zhefeng Hu and M. Santagiustina, "Analytic Study of the Modulation Response of Reflective Semiconductor Optical Amplifiers," in *Journal of Lightwave Technology*, vol. 33, no. 20, pp. 4367–4376, Oct. 15, 2015.
- [36] C. Antonelli and A. Mecozzi, "Reduced model for the nonlinear response of reflective semiconductor optical amplifiers," *IEEE Photon. Technol. Lett.*, vol. 25, no. 23, pp. 2243–2246, Dec. 2013.

- [37] S. P. O Duill and L. P. Barry, "Improved reduced models for single-pass and reflective semiconductor optical amplifiers," *Opt. Commun.*, vol. 334, pp. 170–173, 2015.
- [38] M. J. Connelly, "Reflective Semiconductor Optical Amplifier Pulse Propagation Model," in *IEEE Photonics Technology Letters*, vol. 24, no. 2, pp. 95-97, Jan.15, 2012.
- [39] M. J. Connelly, "Semiconductor Optical Amplifiers" , Springer; 2002 edition (January 31, 2002)
- [40] J. Mork, A. Mecozzi, and G. Eisenstein, "The Modulation response of a semiconductor laser amplifier," *IEEE J. Sel. Topics Quantum Electron.*, vol. 5, no. 3, pp. 851–860, May/Jun. 1999.
- [41] C. E. Shannon, "A mathematical theory of communication," *Bell Syst. Tech. J.*, vol. 27, pp. 379–423, 623–656, Jul., Oct. 1948.
- [42] A.G. Armada, "SNR Gap Approximation for M-PSK-Based Bit Loading", *IEEE Transactions on Wireless Communications*, vol. 5, no.1, Jan. 2006.
- [43] K. Cho and D. Yoon, "On the General BER Expression of One- and Two-Dimensional Amplitude Modulations", *IEEE Transactions on Communications*, vol. 50, no. 7, pp. 1074-1080, Jul. 2002.
- [44] <http://web.stanford.edu/group/cioffi/book/chap4.pdf>
- [45] P. S. Chow, J. M. Cioffi, and J. A. C. Bingham, "A practical discrete multitone transceiver loading algorithm for data transmission over spectrally shaped channels," *IEEE Trans. Commun.*, vol. 43, no. 234, pp. 773–775, Feb. 1995.
- [46] J. Campello, "Optimal discrete bit loading for multicarrier modulation systems," in 1998 IEEE International Symposium on Information Theory, 1998. Proceedings, 1998, p. 193.
- [47] J. L. Wei, A. Hamié, R. P. Gidding, E. Hugues-Salas, X. Zheng, S. Mansoor, and J. M. Tang, "Adaptively modulated optical OFDM modems utilizing RSOAs as intensity modulators in IMDD SMF transmission systems", *Opt. Express*, vol. 18, no. 8, pp. 8556–8573, 2010.

- [48] L. Q. Guo and M. J. Connelly, “A novel approach to all-optical wavelength conversion by utilizing a reflective semiconductor optical amplifier in a co-propagation scheme,” *Opt. Commun.* **281**(17), 4470–4473 (2008).
- [49] C. Arellano and J. Prat, “Semiconductor optical amplifiers in access networks,” presented at the International Conference on Transparent Optical Network (ICTON), (Barcelona, Catalonia, Spain, 2005), Paper We.A1.4.
- [50] G. Cossu, F. Bottoni, R. Corsini, M. Presi, and E. Ciaramella, “40 Gb/s Single R-SOA Transmission by Optical Equalization and Adaptive OFDM,” *IEEE Photon. Technol. Lett.* **25**(21), 2119–2122 (2013).
- [51] B. Y. Cao et al., “RSOA intensity modulator frequency chirp-enabled 40 Gb/s over 25 km IMDD PON systems,” presented at the Opt. Fiber Commun. Conf., Los Angeles, CA, USA, 2015, Paper W1J.3.
- [52] J. L. Wei, C. Sánchez, R. P. Giddings, E. Hugues-Salas, and J. M. Tang, “Significant improvements in optical power budgets of real-time optical OFDM PON systems,” *Opt. Exp.*, vol. 18, no. 20, pp. 20 732–20 745, Sep. 2010.

CHAPTER 3

ALL OPTICAL OFDM

This chapter provides an introduction to all-optical OFDM (AO-OFDM) data transmission and highlights the advantage over other transmission approaches. Detail investigation of AO-OFDM principle with mathematical expression are also provided for continuous optical IDFT/DFT. The system simulation performance are numerically evaluated for AO-OFDM in direct detection with and without cyclic prefix. Detailed analytically and numerically models are used to investigate a polarization multiplexed AO-OFDM system with coherent detection in long haul transmission. Experimental results are presented using a WSS at the transmitter and either an AWG or FBG at the receiver.

3.1 Introduction

Optical networks based on WDM with direct detection (DPSK/DQPSK) or OOK cannot accommodate the new requirements related to the increasing demand for bandwidth. There are at least two weak points of old WDM networks: 1) they cannot provide flexible networks if the traffic of data is changing for example 2) higher order modulations to increase the spectral efficiency is very challenges and the fixed optical grid. Elastic optical networks is the main candidate to fulfill all this requirements 0.

Two optical transmission system are the main candidate addressing towards elastic networks; orthogonal frequency division multiplexing (OFDM) which utilize orthogonal sinc-shape subcarriers spaced the inverse of symbol period [2] and Nyquist wavelength division multiplexing (NWDM) which utilize rectangular subcarrier spaced close to the symbol rate. This two approaches can transmit spectrally-efficient superchannels with bit rates beyond 1 Tb/s [4]. At the receiver side, the superchannels are demultiplexed by a set of filters with sinc-like or rectangular transfer functions. Both approach utilize a variable number of low data-rate subcarriers to adjust the aggregate rate.

Chromatic dispersion (CD) and polarization mode dispersion (PMD) can be effectively estimated and compensated in digital coherent detection schemes, using adaptive equalizer and digital signal processors (DSP), which are low cost to produce in volume. NDWM is more suitable for ultra long haul link; is cost effective and have adaptive capabilities using DSP. OFDM is more suitable for metro and long haul; provide subwavelength granularity; high degree of flexibility by using the electrical subcarriers and can provide one tap equalizer to compensate for linear effects. The main disadvantage from both system is DAC/ADC bandwidth limitations; high power consumption and nonlinear limitations [5].

AO-OFDM is a promising alternative approach, that offers the advantage of reduced power dissipation and does not require high-speed DAC/ADC where both IFFT/FFT operation are performed in optical domain [6]. AO-OFDM can also be used in software defined transceiver for high sped flexible optical network [7].

The main difference electrical and optical OFDM is that a linear convolution is performed among the data signal and the IFFT/FFT impulse response in the optical

domain. On the other hand, in the electrical domain, it is possible to generate a circular convolution by introducing a cyclic prefix or/and postfix to improve the fiber dispersion tolerance and simplify the digital equalizer. An optical gating module is needed in the AO-OFDM approach to sample the demultiplexed waveforms in the middle of the optical eye diagram. Alternatively, a large-bandwidth receiver, with sampling rate larger than $4R$ is required, being R the symbol rate; in this way, the effects of inter-carrier interference (ICI) are reduced [8]. Many techniques have been proposed to perform the optical IFFT/FFT based, for instance, on Mach-Zehnder delay interferometers using either a continuous wave source with data modulation [9] or a pulsed optical signal from a mode locked laser diode (MLLD) [10]. Arrayed waveguide gratings (AWG) [11], wavelength selective switches (WSS) [12], fiber Bragg gratings (FBG) [13] have been used, and a coherent wavelength division multiplexing approach has been also proposed, based on no guard-interval OFDM [14].

All these approaches can be grouped in two categories, depending on the optical source: a first approach is based on a frequency-locked optical comb (no need to be phase-locked), and a train of short pulses is generated either by a MLLD or a continuous wave (CW) laser followed by phase modulators (PM). Alternatively, it is possible to use a set of independent CW lasers, modulated by I/Q modulators to obtain a *sinc*-shaped optical spectrum. In this case, the optical waveform strongly depends on the electrical shape, and high speed ADC and RF amplifiers, together with anti-aliasing filters are required. In addition, free running CW lasers can present frequency offsets that enhances the ICI.

In AO-OFDM schemes, the FFT block is optically implemented at the RX, using an AWG or WSS. However, it is also possible to demultiplex the subcarriers in the electrical domain, using an electrical FFT block and a large bandwidth RX, to detect at least three adjacent subcarriers [12]. We generically refer to this hybrid approach, (optical IFFT at the TX and electrical FFT at the RX) as coherent OFDM (CO-OFDM).

3.2 Principle of operation

At the transmitter side, the AO-OFDM general setup consist in a train of optical pulse which are generated with repetition rate equal to the channel spacing that coincides also with the baud rate of data stream T , and with a time duration T_s short enough to cover all

the generated spectrum of OFDM subcarriers. The pulse stream is passively split to feed optical modulators. The data modulated pulses are fed to each subcarrier of AO-OFDM device where sinc-shape filters are used to separately filter each channel and combine them together by performing an inverse DFT operation. At the receiver side same optical filters performs the DFT operation by demultiplexing the OFDM sub-carriers, show in Figure 3-1.

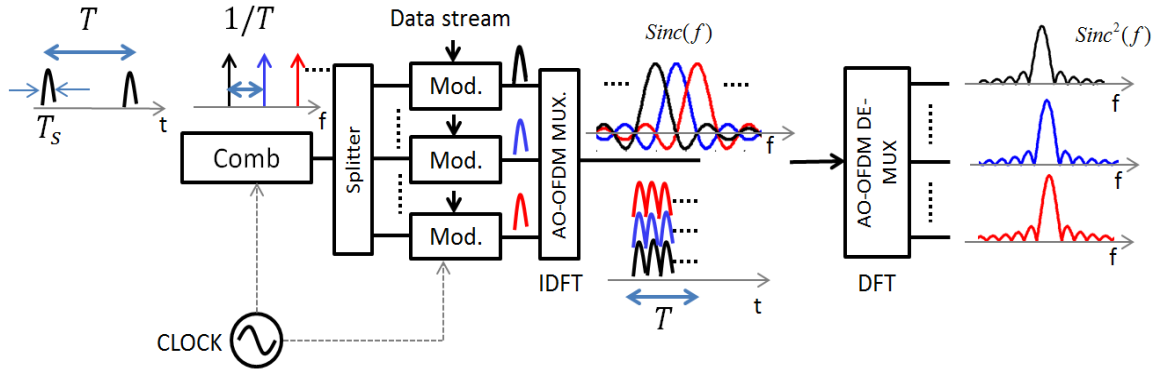


Figure 3-1: Architecture of an AO-OFDM system.

The AO-OFDM principle is explained in more detailed by re-calling the digital IDFT operation. The N-point IDFT operation is performed as:

$$x_m = \sum_{n=0}^{N-1} X_n e^{j2\pi \frac{mn}{N}} \quad 3-1$$

where the N inputs X_n (frequency domain sample) are transformed into N outputs x_m (time domain samples); N is the number of time/frequency samples and $0 \leq n, m \leq N - 1$. This relation can be written in a continuous time form as:

$$x(t) = \sum_{n=0}^{N-1} e^{j2\pi \frac{mn}{N}} \delta(t - nT_s) * X_n(t) \quad 3-2$$

with $X_n(t) = \sum_{i=-\infty}^{+\infty} c_{n,i} \delta_n(t - iT)$ the input signals to be transformed taken with a period T as in discrete case; $T_s = T/N$ is the sampling interval. If the impulse response of the continuous IDFT is $h_m(t) = \sum_{n=0}^{N-1} e^{j2\pi \frac{mn}{N}} \delta(t - nT_s)$ the output of IDFT will be a

train of Dirac delta functions with phases $e^{j2\pi\frac{mn}{N}}$ and time delay/duration T_s . 3-2 can be simplify by performing the convolution with the Dirac delta obtaining:

$$x(t + iT) = \sum_{i=-\infty}^{+\infty} \sum_{n=0}^{N-1} e^{j2\pi\frac{mn}{N}} c_{n,i} \delta_n(t - (nT_s + iT)) \quad 3-3$$

where $c_{n,i}$ is the i th information symbol at the n th subcarrier and δ_n should be an optical pulse with time duration equal to T_s and i integer number which can be assumed zero for simplification if $0 \leq t < T$. To perform 3-3 in the optical domain, an optical comb is needed to provide a train of short pulses $X_n(t)$ with time duration T_s which will also provide the information symbols to transmit with symbol rate equal to $1/T$; optical delays with delay time T_s and phase shifter with precise phases $e^{j2\pi\frac{mn}{N}}$. In Figure 3-2 is shown the principle operation of optical IDFT for $0 \leq t < T$ expressed with 3-3 :

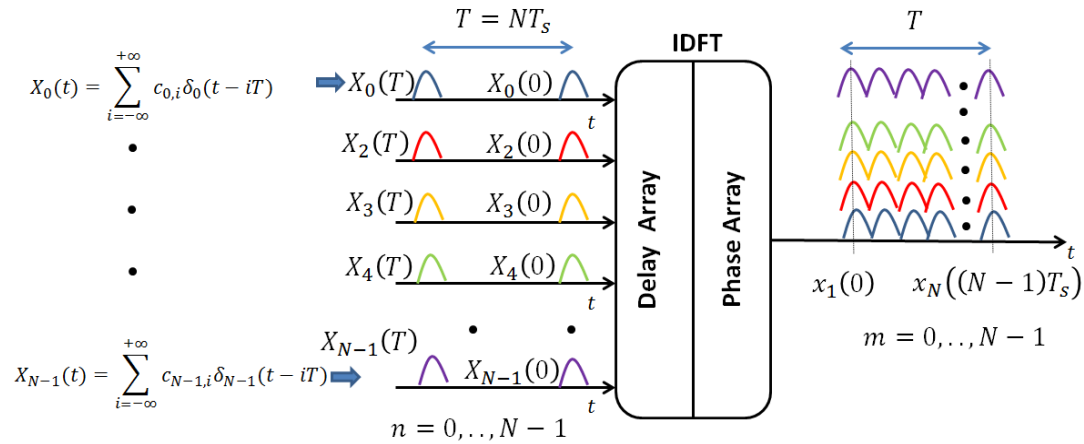


Figure 3-2: Optical IDFT operation.

At the output of IDFT, sampling at time positions $t = mT_s$ is performed [15]. The optical IDFT circuit simplify with delay and phase array is shown in Figure 3-3, where the triangles are coupler/splitter. Short pulses modulate in phase/amplitude (to provide information) and generated from the same laser source are used as inputs for the IDFT optical circuit. Different colors correspond to different input subcarrier. At the output N-copy of each pulse with a deterministic phase is created in order to shift the spectrum of the subcarrier as a function of the input port. In other words, all the spectral information

provided by the input train of short pulses are filtered with the same *sinc*-shape filter spaced $1/T$ between two adjacent ports. At the output, the N th copy of the pulses originated from one port are summed with other N th copy from the other N -ports without inter-carrier interference (ICI). The number of copy N depend on the number of inputs port or subcarrier and so the total bandwidth consider. This is a fundamental difference from the digital implementation of IDFT where the whole bandwidth is equal to symbol rate, whereas in optical IDFT the total bandwidth is

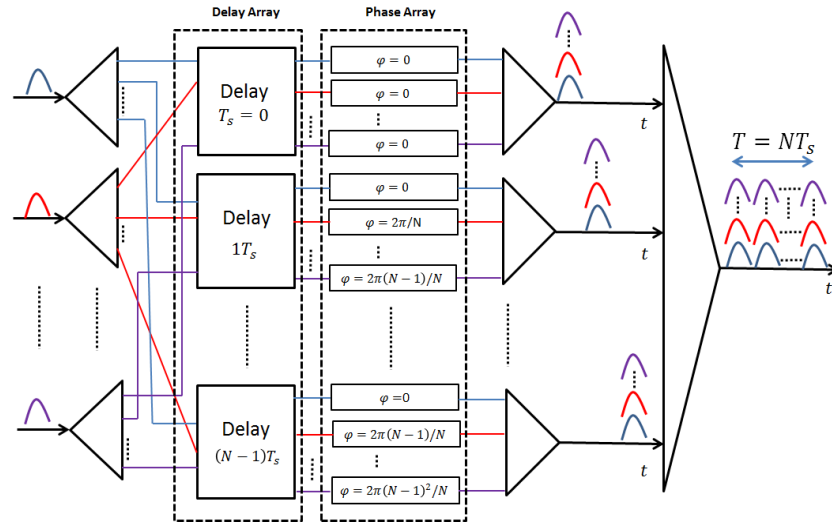


Figure 3-3: Optical IDFT circuit.

decided by the symbol rate but it is N times larger. This of course depend on the sampling time T_s . In digital domain we have a sampling time equal to inverse of the symbol rate whereas in optical domain the sampling time is equal to T/N with $1/T$ the symbol rate. In optical IDFT the dual ‘symbol rate’ will be the sampling time $1/T_s$.

If ‘discrete’ frequency is $f_n = nf$ with $f = 1/(NT_s) = 1/T$ sampling frequency interval, the product of sampling time and frequency is: $T_s f = 1/N$. Once f and N is decided the sampling time is found as: $T_s = 1/fN$.

To evaluate the frequency domain representation of the optical IDFT the Fourier transform of the impulse response $h_m(t) = \sum_{n=0}^{N-1} e^{j2\pi \frac{mn}{N}} \delta(t - nT_s)$ is evaluated as:

$$\begin{aligned}
H_m(f) &= \sum_{n=0}^{N-1} e^{j2\pi \frac{T_s n m}{T}} e^{-j2\pi n T_s f} \\
&= \sum_{n=0}^{N-1} e^{-j2\pi n T_s \left(f - \frac{m}{T}\right)} \\
&= \frac{e^{-j\pi T_s \left(f - \frac{m}{T}\right) N} \sin\left(\pi T_s \left(f - \frac{m}{T}\right) N\right)}{e^{-j\pi T_s \left(f - \frac{m}{T}\right)} \sin\left(\pi T_s \left(f - \frac{m}{T}\right)\right)}
\end{aligned} \tag{3-4}$$

where apart from a phase multiplication the Dirichlet kernel function is derived and defined as:

$$D(N, u) = \frac{\sin(\pi u N)}{\sin(\pi u)} \tag{3-5}$$

with $u = T_s \left(f - \frac{m}{T}\right)$. The maximum of $D(N, u)$ is obtained at $u = 0$ when $f = m/T$. At multiply of m/T the center of each subcarrier is find. The main lobe of $D(N, u)$ is find by the condition: $uN = 1 \Rightarrow f = \pm(1/T + m/T)$, which are also the zeros of the optical IDFT transfer function. This zeros are not the only one, there are addition zeros at multiply of $f = p(1/T + m/T)$, $p = \pm 2, \pm 3, \dots$. Local maximum and minimum can be easily approximated at frequency: $f = (p + 1)(1/T + m/T)$ and this region are called side lobes of the transfer function. 3-5 for a fixed output port m has a periodicity $f = 1/T_s$ defined as free spectral range (*FSR*) of the optical IDFT device. Once the number of input/output N ports have been decided together with symbol rate/subcarrier spacing, the $FSR = N/T$ and $T_s = 1/FSR$.

To provide this phases and delays an AWG can be used to perform the IDFT operation [16] with low insertion loss, easy to increase the number of ports and to integrate in a planar silica. The AWG was proposed first proposed in [17], for optical-code division multiply-access (OCDMA) who turns out to use the same deterministic phase of the IDFT. An AWG configuration that implements the IDFT/DFT in the optical domain is shown in Figure 3-4; it composes of two slab couplers with confocal configuration, so that the distance between the two spherical surfaces is equal to their distance R . The input/output waveguide gratings compose of N waveguides with width w and pitch is do .

The inner grating composes of N waveguides with the same width and pitch d ; the delay T_s among the waveguide is the FSR. If the slab parameters satisfy the condition: $N = R\lambda/d_0dn_{eff}$ with λ central wavelength of optical laser source and n_{eff} slab refractive index the transfer function is same as in 3-4. If $N = 8$ and $T = 40$ [ps] the free spectral range is: $FSR = 200$ [GHz]. In Figure 3-5 is shown the power spectral distribution (PSD [dB]) of 3 adjacent subcarriers where the FSR is highlight. The main lobe width of each subcarrier is 50 [GHz].

The main drawback of using an AWG is the slab diffraction effect which modify the impulse response of the device as:

$$h_m(t) = e^{-\left(\frac{\pi w}{d_0 N T_s} t\right)^2} \sum_{n=0}^{N-1} e^{j2\pi \frac{mn}{N}} \delta(t - nT_s) \quad 3-6$$

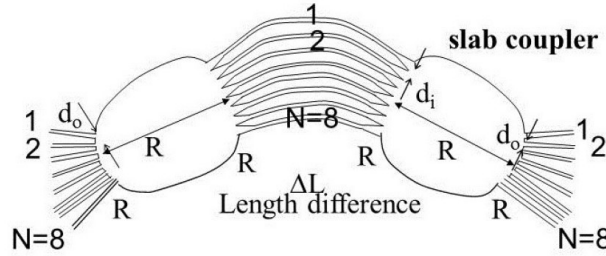


Figure 3-4: AWG configuration for IDFT/DFT operation [7].

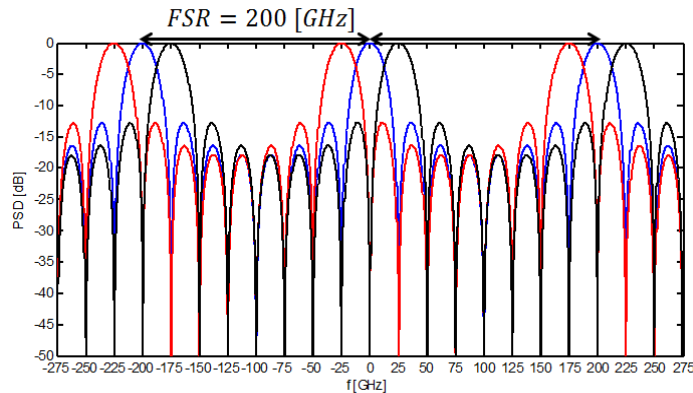


Figure 3-5: Power spectral distribution of three adjacent subcarriers with $N = 8$, $T = 40$ [ps] and $FSR = 200$ [GHz].

At the receiver same AWG can be used as a DFT. Let's suppose $i = 0$ and only one subcarrier is transmitted with $c = 1$. The detected signal at n th subcarrier after the DFT can be written as:

$$Y_n(t) = \sum_{k=0}^{N-1} \sum_{m=0}^{N-1} e^{j2\pi \frac{(m+k)n}{N}} \delta(t - (k+m)T_s) \quad 3-7$$

where it is observed that in optical domain a linear convolution is performed because the total number of sample after the DFT is $2N - 1$. For $m + k = N - 1$ there is a superposition of N pulses, which gives the right sample time $t_s = (N - 1)T_s$. In this case, the received waveform $Y_n(t)$ is:

$$Y_n(t) = N\delta(t)e^{j2\pi \frac{(N-1)n}{N}} \quad 3-8$$

If the signal does not match to the transmitted subcarrier, it can be expressed at time $t_s = (N - 1)T_s$ as:

$$\begin{aligned} Y_{n,p}(t) &= \sum_{k=0}^{N-1} \sum_{m=0}^{N-1} e^{j2\pi \frac{kn+pm}{N}} \delta(t - (k+m)T_s) \\ &= \delta(t)e^{j2\pi \frac{(N-1)p}{N}} \sum_{m=0}^{N-1} e^{j2\pi \frac{m(n-p)}{N}} \\ &= \delta(t)e^{j2\pi \frac{(N-1)p}{N}} \frac{1 - e^{j2\pi(n-p)}}{1 - e^{j2\pi \frac{(n-p)}{N}}} \end{aligned} \quad 3-9$$

where $p \neq n$ is a different port. If all the subcarrier are transmitted at the receiver there is not only the desired information given by 3-7 but there is also information by adjacent ports expressed by 3-9. However at time sample $t_s = (N - 1)T_s \Rightarrow Y_{n,p}(t) = 0$. This crosstalk requires a precise optical sampling with an optical time gating module or a large electrical bandwidth (4 times the symbol rate) in order to sample at the electrical domain. In Figure 3-6 (a) is shown the received signal at the matched port with the desired information and (b) the unmatched port signal. If time gating is performed at the right time the unmatched port information will cancel and no cross-talk will be observed. The cross talk originated from the adjacent port is higher from the cross talk of the other ports.

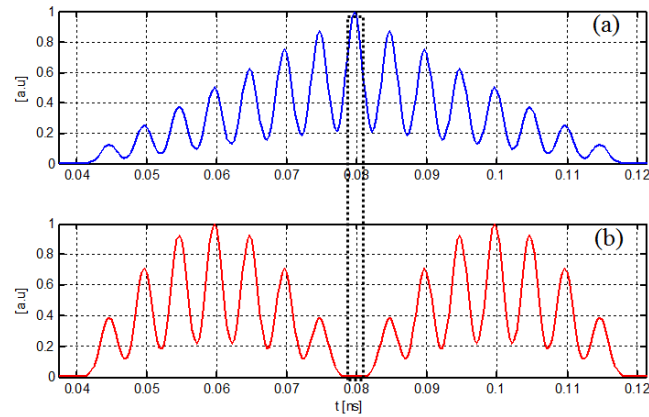


Figure 3-6: (a) Received signal at the matched port (b) and unmatched port.

A complementary AO-OFDM TX is shown in Figure 3-7 (b), where the position of the splitter and optical multiplexer are inverted, compared to Figure 3-7 (a). In this case, input optical spectral lines are demultiplexed and shaped by the AWG or the wavelength selective switch (WSS), that generate the OFDM symbols. A detailed analytical and numerical comparison of the two approaches is presented in [18], showing that the system performance in the configuration of Figure 3-7 (b) strongly depends on the DAC and modulator bandwidth, which affects the subcarriers orthogonality.

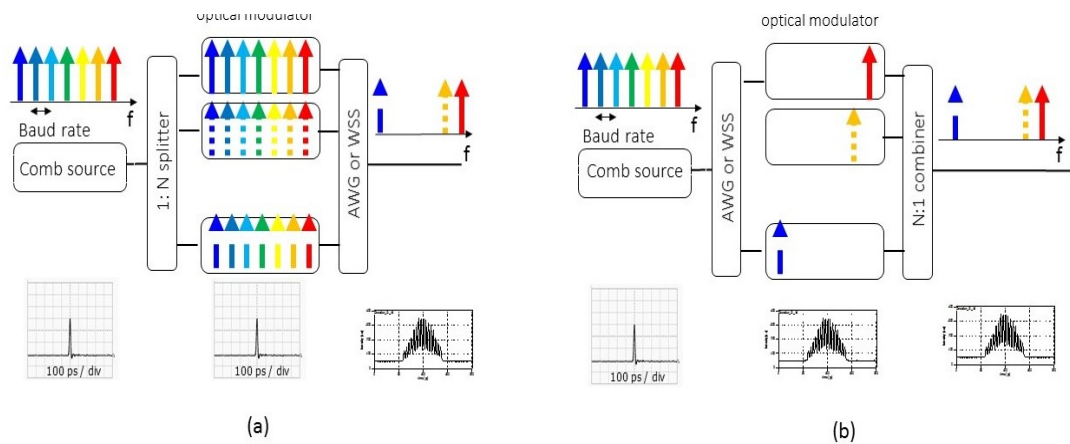


Figure 3-7: . Complementary schemes of an AO-OFDM transmitter.

A basic experiment that confirms this result is performed, considering a $N = 16$ subcarrier, $T = 12.5$ GHz spaced AO-OFDM system, using Lithium Niobate phase modulators, with approximately 12.5 GHz bandwidth. The OFDM symbol corresponding to a single subcarrier is shown in Figure 3-8 (a) and (b), using the two architectures of Figure 3-7, respectively. In the case of the setup of Figure 3-7 (a), the rising and falling time is about 40 ps, and it is related to the input pulse duration. On the other hand, using the setup of Figure 3-7 (b), the symbol rising and falling time becomes 40 ps, due to 12.5 GHz modulator bandwidth. We incidentally observe that, in both cases, the OFDM symbols have not a rectangular profile, due to an additional waveform resaper, that has been introduced after the TX, to enhance the system performances [11] and compensate the slab diffraction effect in the AWG.

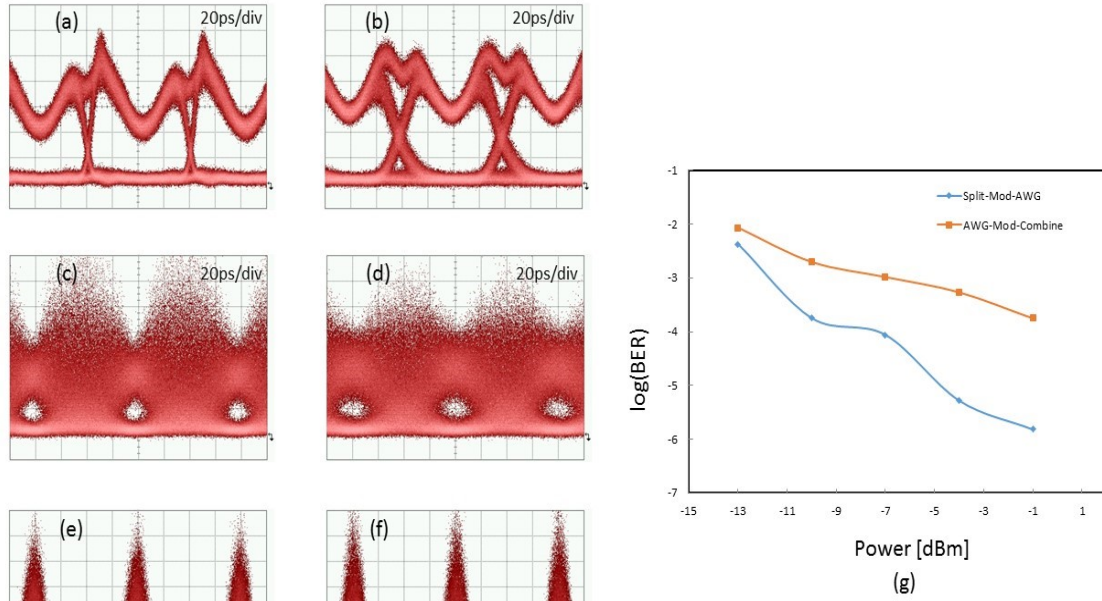


Figure 3-8: (a) and (b) OFDM symbol. (c) and (d) demultiplexed symbol. (e) and (f) after time gating. (a), (c) and (e) are obtained with the scheme of Figure 3-7(a) and (b), (d) and (f) with the scheme of Figure 3-7(b). (g) BER performance of the two schemes of Figure 3-7.

At the RX, the signal is first demultiplexed using another AWG, and then time gating is applied. The demultiplexed signal, before and after time gating are shown in Figure 3-8 (c) and (e), respectively, for the setup of Figure 3-7(a), and in Figure 3-7(d) and (f), for the setup of Figure 3-7(b). Finally, the BER measurements of Figure 3-8 (g) confirm that the scheme of Figure 3-7 (a), reduces ICI, thanks to the steep rising and falling edge of the OFDM waveforms. Therefore, it is concluded that the scheme of Figure 3-7 (a) is preferable, thanks to the short duration of the modulated optical pulses, that are not affected by the electrical waveform, modulator bandwidth, or DAC resolution.

3.2.1 Cyclic prefix in AO-OFDM setup

In this section the performance of AO-OFDM with direct detection are evaluated with and without cyclic prefix (CP). Adding a CP in optical domain is not obviously, especially when optical IDFT is placed after the modulators. This leaves with the only possibility to modify the AWG device in order to extend the OFDM symbol by T_{CP} . The AWG modification is shown in Figure 3-9 taken from [19]. The pulses generated from a comb source enter the first slab coupler which is simply a splitter and then fed to the modulators. The output of the modulators which are the Fourier coefficients are then phase shifted by the second slab coupler with IDFT deterministic phases. The pulses generated from a comb source enter the first slab coupler which is simply a splitter and then fed to the modulators. The output of the modulators which are the Fourier coefficients are then phase shifted by the second slab coupler with IDFT deterministic phases.

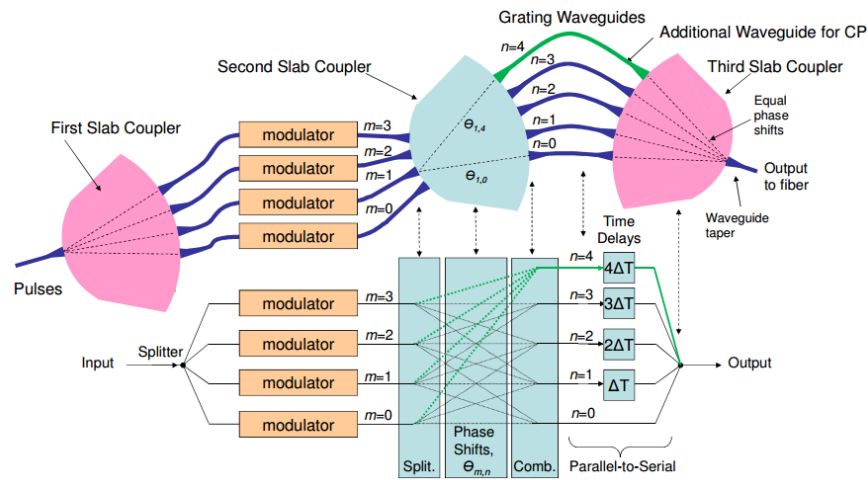


Figure 3-9: AO-OFDM setup with AWG modification to insert the CP [19].

An addition waveguide longer than the other is inserted in order to extend the OFDM symbol. In this case the periodicity of the optical IDFT was used to apply a post-CP. Every 4 pulses one more pulse is added from the addition waveguide. This setup is equivalent to a lower symbol rate without changing the AWG configuration. The OFDM symbol duration is increased and it is simply: $T_{CP} = T(N + N_{CP}/N)$. Consider the number of CP equal to P , then the number of samples is increased to $K = P + N$ and 3-3 is modify as:

$$x(t) = \sum_{n=0}^{K-1} e^{j2\pi \frac{mn}{N}} c_n \delta_n(t - nT_s) \quad 3-10$$

The main drawback of this method is that the source and data rate should be reduced in order to accommodate the CP in one symbol OFDM. Every time one need to add a CP the comb frequency must be changed.

In order to not change the source frequency comb a WSS is proposed in [20] to re-place the AWG. The benefits is twofold because using a WSS at the transmitter a flexible allocation of the subcarriers can be achieved and also a variable symbol rate can be used. If the symbol rate change the WSS will change its impulse response in order to fit the new rate.

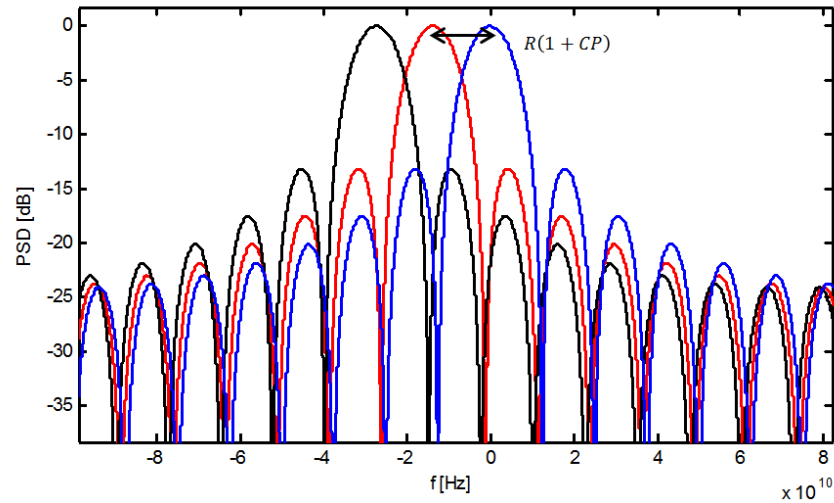


Figure 3-10: Three subcarriers with CP = 0.1 and R = 12.5 [GHz].

This is not possible with an AWG is used at the transmitter. This method consist on changing the spacing of the WSS sinc-shape filters while keeping same spectral width in order to reduce the OFDM symbol duration with respect to duration of the comb repetition time to accommodate for the CP. The WSS k th filters can be expressed in frequency domain as:

$$H_{WSS,k}(f) = \text{sinc}\left(\frac{f - kR(1 + CP)}{R}\right) \quad 3-11$$

where $R = 1/T$. This CP is a zero guard interval rather than a copy of some sample from the OFDM symbol. Suppose $R = 12.5$ [GHz] and OFDM symbol duration $T = 80$ [ps]. If $CP = 0.1$ the OFDM symbol duration is now $T' = 72.7$ [ps]. In Figure 3-10 are shown three subcarriers with a spacing equal to $R(1 + CP)$. An AO-OFDM is simulated with QPSK modulation to verify the proposed CP and the eye diagram with and without CP is shown in Figure 3-11.

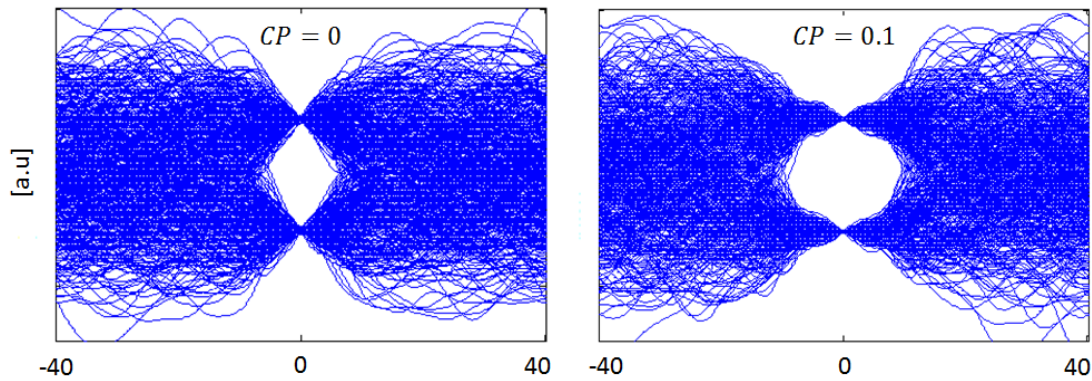


Figure 3-11: Eye diagrams with and without CP.

3.3 Direct detection

In this section AO-OFDM with direct detection is investigated w/o CP. Two modulation formats are investigated: differential phase shift key (DPSK) and differential quadrature phase shift key (DQPSK) with a symbol rate equal $R = 12.5$ GHz. Both modulation

encode information on the phase of the signal. Because the photodiode is only sensitive to the optical power a one bit delay line interferometer (DLI) is used for demodulation [21]. With DLI, the information at the transmitter is encoded on the phase difference between consecutive symbols.

3.3.1 DPSK modulation

The setup of AO-OFDM with DPSK modulation is shown in Figure 3-12.

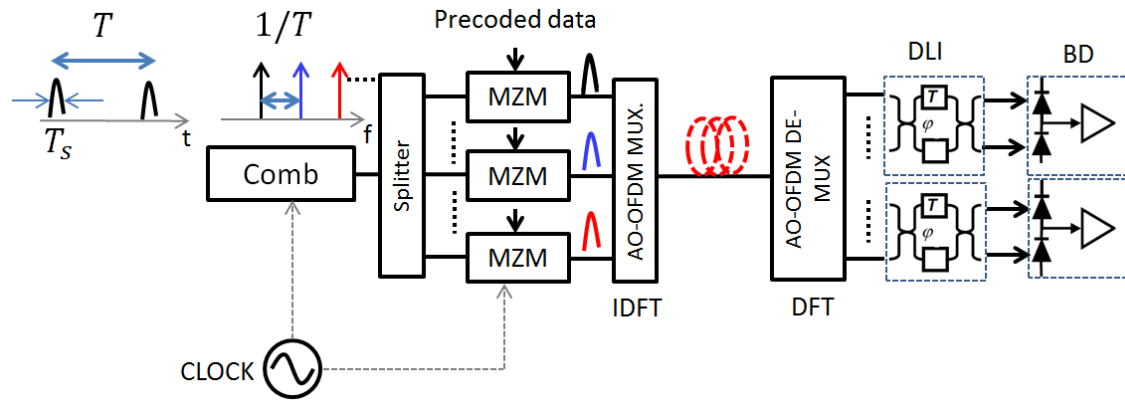


Figure 3-12: AO-OFDM based DPSK modulation setup.

At the transmitter side to avoid chirp between symbols transition a MZM modulator is used biased at the minimum with a peak to peak ideal voltage equal to $2V_\pi$ as shown in Figure 3-13.

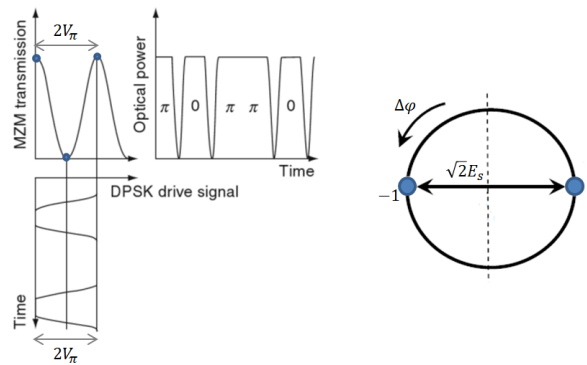


Figure 3-13: MZM operation for DPSK modulation and signal constellation.

The 180° phase is encoded when the MZM switched between two maximum and at the output intensity dips are observed. This characteristic can also be observed from the DPSK signal constellation where transition across the zero is obtained every time there is a switch between two maximum of the MZM operation or between '+1' and '-1'. The distance between two constellation points is $\sqrt{2}E_s$ where E_s is the signal energy and the phase difference is $\Delta\phi$. Before the optical modulation the electrical signal is differential encoded to realize the correlation between different symbols transmission. The differential encoded is realize by XOR (modulo-2 addition) functions as follows:

$$d(k) = a(k) \oplus d(k-1) \quad 3-12$$

where $a(k)$ is the current data to be transmitted which is differential encoded in a new sequence $d(k)$. The encoder is shown in Figure 3-14.

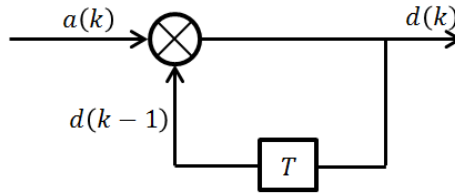


Figure 3-14: Differential encoder.

At the receiver the differential phase modulation is converted to an amplitude modulation by using a DLI in a MZM configuration as in Figure 3-12. The delay between two arms of the MZM is equal to the symbol interval T . The power at the constructive port of the DLI is simply: $P_{DLI,out,1}(t) = P_{DLIin}(t)\cos^2\left(\frac{\varphi(t)-\varphi(t-T)}{2}\right)$. In case of equal phase difference the output power is maximum and minimum otherwise. At destructive port the power is : $P_{DLI,out,2}(t) = P_{DLIin}(t)\sin^2\left(\frac{\varphi(t)-\varphi(t-T)}{2}\right)$. If $\varphi(t) - \varphi(t-T) = 0 \Rightarrow P_{DLI,out,1}(t) = P_{DLIin}(t)$ & $P_{DLI,out,2}(t) = 0$; if $\varphi(t) - \varphi(t-T) = \pm\pi$ then $P_{DLI,out,1}(t) = 0$ & $P_{DLI,out,2}(t) = P_{DLIin}(t)$. The spectrum of the both destructive and constructive port is shown in Figure 3-15. Both spectrum have same information and in theory only one output port need to be received. Further, an OOK conversion is

performed after the DLI based MZM configuration. In order to improve of 3dB the OSNR a balanced photo-detector (BPD) is usually used because the different output ports OOK modulation have opposite polarities. The signal generated at the constructive port is known as duobinary modulation, similar to electrical duobinary format. At the destructive port the signal generated is known as alternate mark inversion (AMI) where the carrier frequency is suppressed.

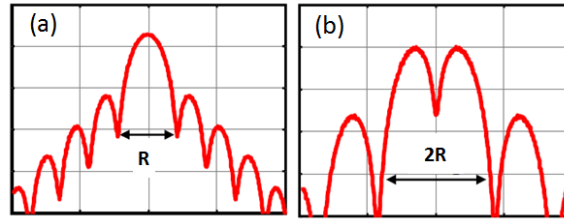


Figure 3-15: Constructive (a) and destructive (b) spectra generation at the outputs of the DLI.

3.3.1.1 Simulation results for DPSK

To evaluate AO-OFDM based DPSK modulation different number of channels are simulated. The symbol rate considered is $R = 12.5$ [GHz]. The setup is based on Figure 3-16. An AWG with 16 ports is used at the receiver with 12.5 [GHz] subcarrier spacing and 200 GHz free spectral range.

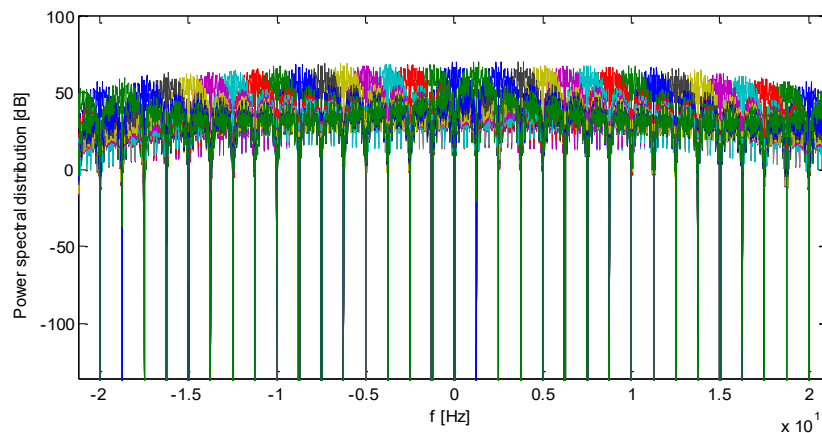


Figure 3-16: Power spectral distribution of AO-OFDM 16 DPSK modulated subcarriers.

After the demodulation performed by the AWG an optical time gating is used to sample in the middle of the eye diagram followed by a DLI and BPD. 16 DPSK-modulated subcarriers are shown in Figure 3-16, where it is observed a very flat power distribution among the subcarriers.

In numerical simulation an optical pre-amplifier is considered at the receiver side where an OSNR defined as the ratio of signal power, P_s , and noise power is imposed by adding ASE noise. The OSNR is defined as:

$$OSNR = \frac{P_s}{pN_0B_{ref}} \quad 3-13$$

where p is 1 or 2 depending if the noise is consider in one or two polarization, N_0 is the single-sided power spectral density and B_{ref} is the optical noise bandwidth equal to: $B_{ref} = \Delta\lambda \frac{f^2}{c}$ where c is the speed of light, f carrier frequency and $\Delta\lambda$ is th reference bandwidth set usually to 0.1nm. The OSNR is measured before the AWG demultiplexing. No other optical filter is used. After the BPD an electrical 5-th order Bessel filter is used, with bandwidth $0.8 \cdot R$. To estimate the average bit error rate (BER) a Monte Carlo (MC) simulations method is considered, investigating only the central subcarrier which show the worst cross-talk due to the overlap spectra with other subcarriers. In order to estimate the BER different noise samples are simulated and added to the system by running different loop. The simulation stop by defining a relative error. The average BER is given as:

$$\hat{P}_E = \frac{1}{N_R N_b} \sum_{i=1}^{N_R} \sum_{j=1}^{N_b} E_{i,j} \quad 3-14$$

where N_R define how many times the simulation have run, N_b number of bits used in each run and $E_{i,j}$ error variable ($E = 0$ if no error is found and $E = 1$ if an error is found) on the i th run of the j th bit transmitted. The unbiased and consistent variance from the current block is calculated as: $\sigma_E^2 = 1/(N_R - 1) \sum_{i=1}^{N_R} (E_i - \hat{P}_E)^2$. The confidence interval for the mean value m_E is then expressed as in [22]: $\hat{P}_E - t_u \sigma_E / \sqrt{N_R} < m_E < \hat{P}_E +$

$t_u \sigma_E / \sqrt{N_R}$ where t_u is the uth percentile of a Student t-distribution. For high N_R this value is approximated to: $t_u \cong x \sqrt{N_R} / \sqrt{N_R - 2}$ with $x = 2$ the confidence interval is 95%. The simulation will stop if the error: $e_p \leq accuracy_value$ where $e_p = x \sqrt{N_R} / \sqrt{N_R - 2} \sigma_E / \sqrt{N_R}$.

In the following simulation the BER accuracy is 0.1, with 95% Gaussian confidence.

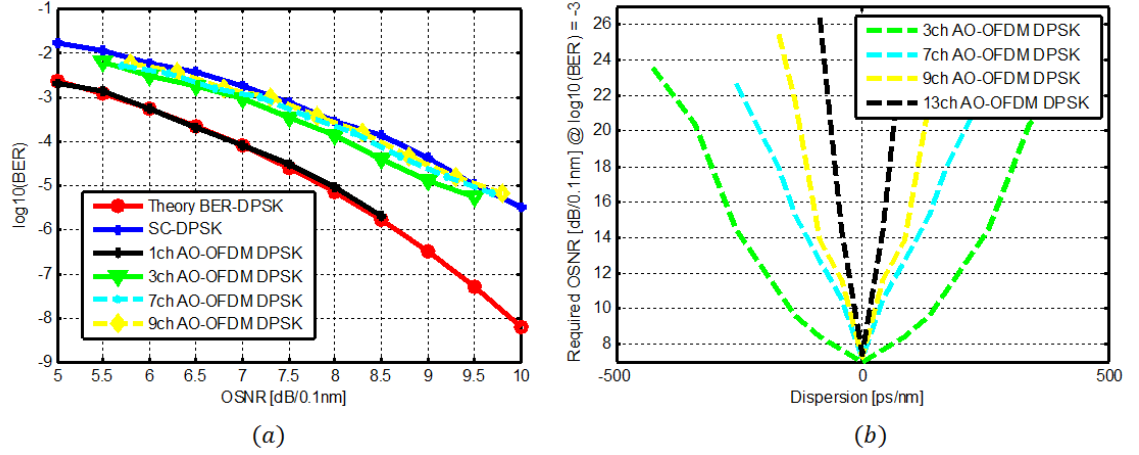


Figure 3-17: (a) BER as a function of the OSNR for a 12.5 Gb/s DPSK AO-OFDM subcarrier in BtB for different number of subcarriers. (b) Required OSNR as a function of the total CD accumulated for different number of subcarriers.

Figure 3-17(a) shows $\log(\text{BER})$ for a back-to-back (BtB) configuration for 12.5 Gb/s DPSK modulation. In blue-line is shown the performance of a single carrier 12.5 Gb/s DPSK modulated, without time-gating, and in red-line is shown the theoretical curve of DPSK modulation calculated as in [23]:

$$BER_{DPSK} = \frac{1}{2} e^{-SNR} \left(1 + \frac{SNR}{4} \right) \quad \text{Eq. 3-15}$$

A single carrier DPSK- modulated is shown in black line with the same performance as the theoretical one, because we are receiving with a match filter. It is also show the performance in case of 3, 7, 9 subcarriers, which show better performance in BtB compare to single channel DPSK. At a $\log(\text{BER})$ equal to -3, a 2.5dB penalty compare to the theoretical one due to the cross-talk between the subcarriers is observed. To measure the system performance, in terms of chromatic dispersion (CD) tolerance, the length of the single mode fiber (SMF) is changed, in order to get different value of CD. The

polarization mode dispersion (PMD) and nonlinear effects are not considered. Figure 3-17(b) shows the CD tolerance at 12.5 Gb/s for different number of subcarriers. It shows the required OSNR at a $\log(\text{BER})$ equal to -3 as a function of the total accumulated chromatic dispersion. As can be observed, the system shows large penalty if the number

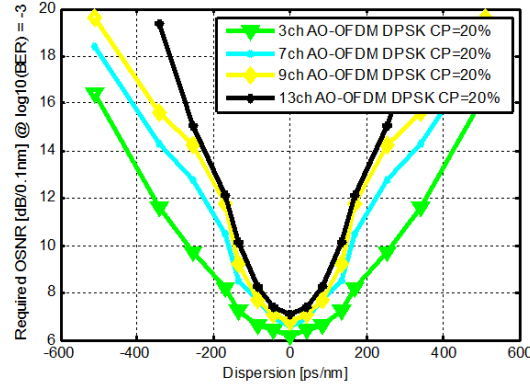


Figure 3-18: Required OSNR as a function of the total CD for different number of subcarriers considering 20% of CP.

of subcarriers is increased. If a CP is considered with the signal, the CD tolerance is increased as shown in Figure 3-18. It is considered just 20% of CP, corresponding to 10 Gb/s for each subcarrier. As can be observed from the figure, we can further increase the CD tolerance. For 13 subcarriers case we can reach approximately 20 km of SMF.

3.3.2 DQSK modulation

As for DPSK modulation for AO-OFDM based on DQPSK the setup is similar. However for DQPSK modulation an I/Q MZM modulator is used. It consists in two MZM in an Mach-Zehnder interferometer structure and a phase modulator with a static phase shift of $\pi/2$ in one of the arms. The principle of DQPSK is to represent two bits by an optical phase difference between consecutive symbols. A pre-coder is used for electrical differential encoding as shown in Figure 3-19. The PRBS sequence is first divided in two odd and even sequences, u_k and v_k , respectively, each at a half bit rate. The differential encoded sequence is then obtained as in [25]:

$$I_k = u_k v_k I_{k-1} + u_k \bar{v}_k Q_{k-1} + \bar{u}_k \bar{v}_k I_{k-1} + \bar{u}_k v_k \bar{Q}_{k-1} \quad 3-16$$

$$Q_k = u_k v_k Q_{k-1} + \bar{u}_k v_k \bar{I}_{k-1} + \bar{u}_k \bar{v}_k \bar{I}_{k-1} + \bar{u}_k \bar{v}_k \bar{Q}_{k-1}$$

3-17

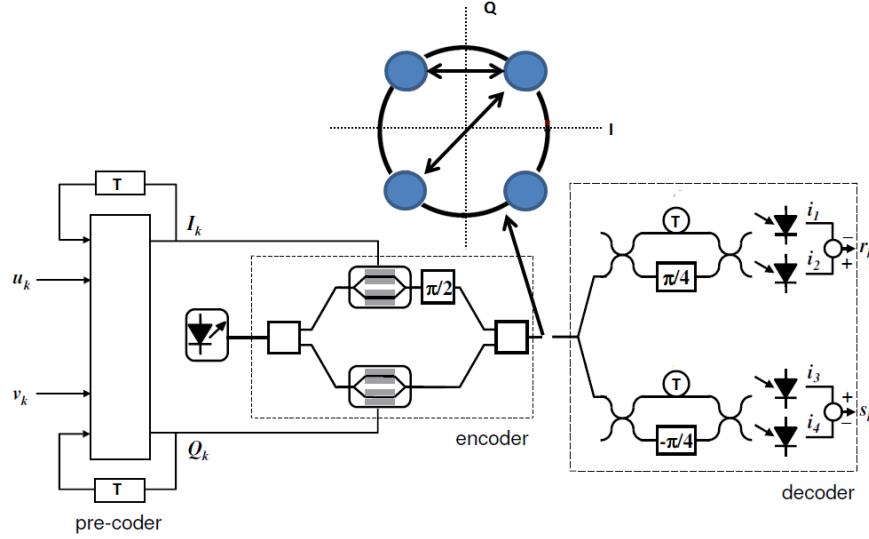


Figure 3-19: Setup configuration of an optical DQPSK transmitter and receiver [24].

The pre-coded sequence is calculated from the previous value I_{k-1} , Q_{k-1} and on the values of u_k, v_k . This differential sequence drive the I/Q modulator biased at the null points with a peak to peak ideal voltage of $2V_\pi$. At the receiver two DLI in parallel are used as decoder with a phase shift of $\pi/4$ and $-\pi/4$ between the two arms in order to decode the I and Q information.

3.3.2.1 Simulation results for DQPSK

The performance in case of DQPSK modulation are investigated, for 25 Gb/s bit rate for each subcarrier. BER as a function of the OSNR in BtB is shown Figure 3-20. In blue-line is shown the performance of a single carrier 25 Gb/s DQPSK, in red line is shown the theoretical curve calculated as [23]:

$$BER_{DQPSK} = Q(a, b) - \frac{1}{2} I_0(ab) e^{-\frac{a^2+b^2}{2}}$$

3-18

where Q is the Marcum Q function, I_0 is the modified Bessel function of the first kind and zero order. The parameter a and b are defined as: $a = \sqrt{\gamma(2 - \sqrt{2})}$, $b = \sqrt{\gamma(2 + \sqrt{2})}$ where γ is the bit SNR.

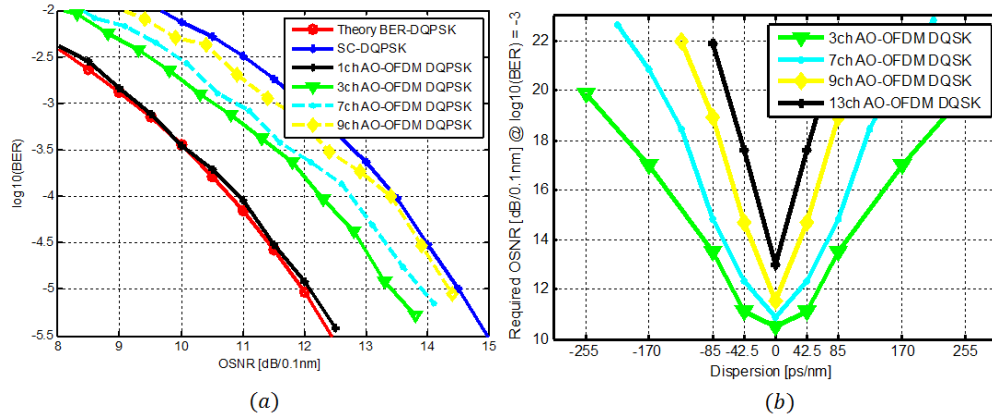


Figure 3-20: (a) BER as a function of the OSNR for a 25 Gb/s DQSK AO-OFDM subcarrier in BtB for different number of subcarriers. (b) Required OSNR as a function of the total CD accumulated for different number of subcarriers.

In black line is shown the 25 Gb/s DQPSK AO-OFDM single carrier. A perfect match between the AO-OFDM and theoretical curve is obtained because we are in the case of match filter.

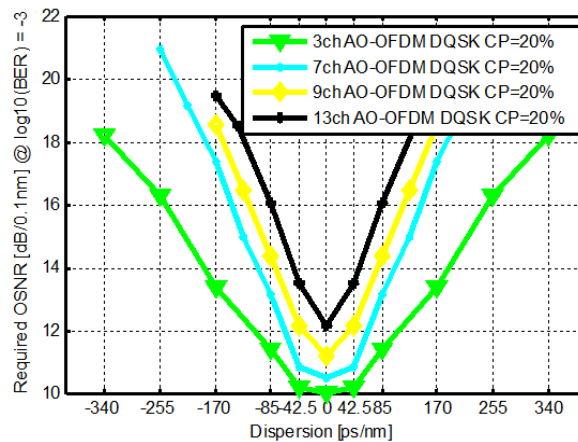


Figure 3-21: Required OSNR as a function of the total CD for different number of subcarriers considering 20% of CP.

There are 2 dB of penalty at $\log(\text{BER})$ equal to -3 between the single carrier DQPSK and AO-OFDM. In case of 3, 7, 9 subcarriers this penalty become lower but still the performance in BtB are better than the DQPSK modulated without optical filters. In case of 9 subcarriers a penalty of 2 dB is find due to the cross-talk of the adjacent channels.

To increase the dispersion tolerance 20% of CP is considered, and the performance are shown in Figure 3-21 for 3,7,9,13 subcarriers.

3.4 Coherent detection

This section is devoted to analyse the performance of AO-OFDM coherent schemes, using advanced modulation and polarization multiplexing (PM). It is consider the scheme of Figure 3-7(a), that presents the better performance for ICI suppression, and use an AWG at the RX, receiving one subcarrier at each output port [26]. Compared to CO-OFDM; no CP, oversampling or fast adaptive filter is required. In CO-OFDM, CP is needed because of the limit RX bandwidth, and a WSS with limit number of ports and low resolution is used at the receiver. An AWG can demultiplex a larger number of subcarrier compare to WSS, without additional power losses [27]. By theoretical analysis and numerical simulations, it is demonstrate that AO-OFDM presents better performances, in terms of phase noise reduction and equalization enhancement phase noise (EPPN).

3.4.1 Coherent setup

The AO-OFDM scheme for dual-polarization is shown in Figure 3-22, and is composed of a MLLD that generates a train of optical pulses with repetition rate $R = 12.5[\text{GHz}]$. The passive splitter divides the signal into N_s outputs, and each signal is independently QPSK or 16-quadrature amplitude modulation (16QAM) modulated. The signals are sinc-shaped filtered and multiplexed by an AWG or a WSS, so that each AO-OFDM symbol of duration $T = 1/R$, for a single polarization, can be expressed as:

$$x(t) = \sum_{k=0}^{N_s-1} X_k \text{rect}\left(\frac{t}{T}\right) e^{-j2\pi f_k t} \quad 3-19$$

where X_k is the k th complex symbol of a pseudo random symbol sequence (PRSS), and $f_k = k/T$ ($k=0, 1, \dots, N_s - 1$) are subcarrier centre frequencies.

The optical link is composed of N spans, each including a single mode fiber (SMF) of $L_{span} = 80 \text{ km}$ length and an erbium doped fiber amplifier (EDFA) with $NF = 6 \text{ dB}$

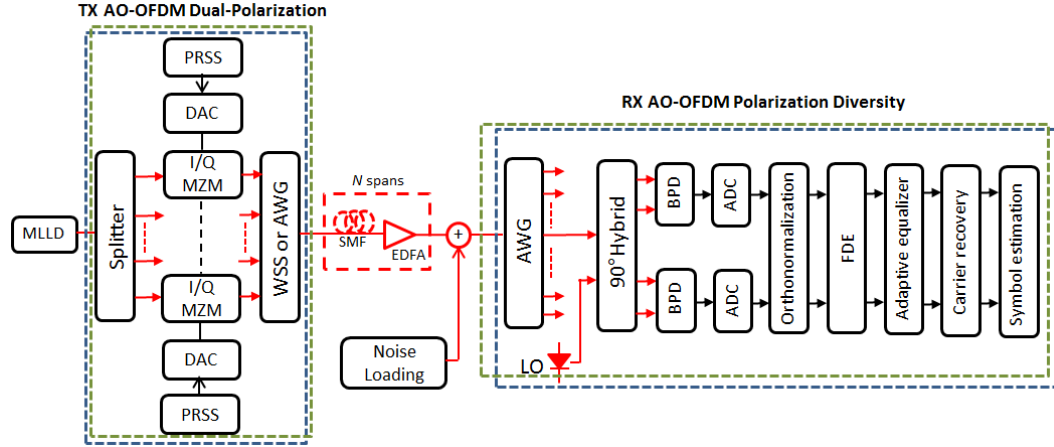


Figure 3-22: AO-OFDM system. Mode-locked laser diode (MLLD), pseudo random symbol sequence (PRSS), digital to analog converter (DAC), optical I/Q Mach-Zehnder modulator (I/Q MZM), wavelength selective switch (WSS), array waveguide grading (AWG), single mode fiber (SMF), erbium doped fiber amplifier (EDFA), additive white Gaussian noise (AWGN), local oscillator (LO), balanced photodetector (BPD), analog to digital converter (ADC), frequency domain equalizer (FDE).

noise figure, whose gain completely recovers the span losses. The fiber attenuation is $\alpha = 0.2 \text{ dB/km}$, the dispersion parameter $D = 17 \text{ ps/nm/km}$, the dispersion slope $S = 0.07 \text{ ps/nm}^2/\text{km}$, the non-linear parameter $\gamma = 1.3 \text{ (Wkm)}^{-1}$ and $\text{PMD} = 0.1 \text{ ps/km}^{1/2}$.

AWGN is loaded at the RX to model the ASE noise introduced by all the EDFAs. In this way, it is possible to evaluate the BER versus the received OSNR; with the only exception of the nonlinear effects study, in sub-section 3.4, where the nonlinear phase noise (NLPN) due to nonlinear signal-noise interaction generated in each span is considered.

After the AWG, which de-multiplex all the subcarriers in parallel, a standard coherent RX is used to recover the complex symbols following by a DSP. The coherent RX includes a CW laser as local oscillator (LO), that mixes with the demultiplexed

subcarrier in a dual polarization 2 x 4 90° hybrid coupler, whose outputs are connected with two balanced photodetectors, for each polarization. The received signals are filtered by a five-pole Bessel filter to simulate the RX bandwidth limitation, and sampled with a 6-bit resolution by an ADC.

The DSP consists of an orthonormalization blocks, digital CD compensation based on an overlap-and-save frequency-domain equalization (FDE) filter [28], adaptive equalizer for the PMD, joint carrier recovery using a feed-forward carrier phase recovery (FFCPE) and maximum like-hood (ML) symbol detection [29].

3.4.1.1 Model with frequency offset and phase noise

In the analytical model the AWG behavior at the RX is assimilated to a correlated optimally match filter for the k th ($k=0, 1, \dots, N_s-1$) subcarrier, and the received complex symbols can be written as [30]:

$$\hat{X}_k = e^{j(\theta_{LO} + \varphi_{LO})} \left[\frac{1}{T} \int_0^T r(t) e^{j2\pi(f_k + \Delta f_{AWG})t} dt \right] \quad 3-20$$

where Δf_{AWG} is the frequency offset of the AWG and $r(t)$ is the received waveform given as:

$$\begin{aligned} r(t) &= e^{j(2\pi\Delta f_{Tx}t + \varphi_{Tx})} \cdot s(t) + n(t) \\ &= e^{j(2\pi\Delta f_{Tx}t + \varphi_{Tx})} \sum_{l=0}^{N_s-1} X_l \text{rect}(t) e^{-j2\pi f_l t} + n(t) \end{aligned} \quad 3-21$$

with $n(t)$ AWGN noise which model the ASE noise, Δf_{Tx} is the TX frequency offset and φ_{Tx} is the phase noise, model as a Wiener process [31] with zero mean and variance of the phase change given by: $\sigma_\varphi^2 = 2\pi\Delta\vartheta T$, with $\Delta\vartheta$ being the laser linewidth. Δf_{Tx} will affect all the subcarrier equally because we assumed a MLLD at the transmitter. We will keep it in the analytically model for cases where the frequency comb is obtained from successive phase modulators which are originated from a CW laser. In this case the stability of the frequency comb will depend only on the frequency locking of the each frequency lines, and don't need to be phase locked. Each RX symbol in 3-20 will also multiply a complex exponential term with phase shift sum of θ_{LO} and φ_{LO} due to local oscillator frequency offset and phase noise, respectively. It is observed that θ_{LO} and φ_{LO}

will affect the system exactly like in single carrier modulated signal, because after the AWG a de-multiplexed waveform is obtained. The fiber transfer function in the equation is omitted which it is supposed completely equalized in digital domain.

3.4.1.2 Frequency offset due to AWG and TX comb

Substituting 3-21 in 3-20 it is obtained:

$$\begin{aligned} \hat{X}_k = e^{j(\theta_{LO} + \varphi_{LO})} & \left[\frac{1}{T} \int_0^T \left\{ e^{j(2\pi\Delta f_{TX}t + \varphi_{TX})} \sum_{l=0}^{N_s-1} X_l \text{rect}(t) e^{-j2\pi f_l t} \right. \right. \\ & \left. \left. + n(t) \right\} e^{j2\pi(f_k + \Delta f_{AWG})t} dt \right] \end{aligned} \quad 3-22$$

where it is observed that θ_{LO} and φ_{LO} are outside the integral and by using DSP it can be mitigated. What we can't recover is ICI originated inside the integral in 3-22. It is consider only the frequency offset originated from AWG and TX comb, neglected the previous effects together with φ_{TX} , and re-write the formula in 3-22 as in [32]:

$$\begin{aligned} \hat{X}_k &= \sum_{l=0}^{N_s-1} X_l H_{A,k} \frac{1}{T} \int_0^T e^{-j2\pi(f_l - f_k - (\Delta f_{AWG} + \Delta f_{TX}))t} dt + n_k \\ &= \eta_0 X_k + \sum_{k \neq l} \eta_{l-k} X_l H_{A,k} + n_k \end{aligned} \quad 3-23$$

where $H_{A,k}$ is the Fourier transform of the anti-aliasing filter and the remain terms are defined as:

$$\eta_0 = \frac{1}{T} \int_0^T e^{-j2\pi\Delta F t} dt = e^{-j\pi\Delta F T} \frac{\sin(\pi\Delta F T)}{\pi\Delta F} \quad 3-24$$

$$\begin{aligned} \eta_{l-k} &= \frac{1}{T} \int_0^T e^{-j2\pi(f_l - f_k + \Delta F)t} dt \\ &= \frac{\sin(\pi(f_l - f_k)\Delta F T)}{\pi(l - k) + \Delta F T} e^{-j\pi((f_l - f_k) + \Delta F)T} \end{aligned} \quad 3-25$$

$$n_k = \frac{1}{T} \int_0^T n(t) e^{j2\pi(f_k + \Delta F)t} dt \quad 3-26$$

where the index l, k takes value on the set S given as: $S[l, k] = \{0, \dots, N_s - 1 : l \neq k\}$ and $\Delta F = \Delta f_{AWG} + \Delta f_{Tx}$ sum of both frequency offset. The first term in 3-23, cause a rotation of the detected signal and is given in 3-24; second term is ICI defined in 3-25; and finally the third one, AWGN, is defined in 3-26. Here we are investigating the worst case condition, where the two frequency offset are with opposite sign (which mean the received waveform and the AWG center wavelength are moving in opposite direction). In 3-25 they just sum together with the same sign giving the totally frequency offset ΔF . ICI is assumed Gaussian-distributed with variance given as:

$$\sigma_{ICI}^2 = \sum_{k \neq l} \eta_{l-k}^2 X_l^2 H_{A,k}^2 \quad 3-27$$

and the signal to noise ratio (SNR) per k th subcarrier is defined as in [33]:

$$SNR_k = \frac{\eta_0^2 E[|X_k|^2]}{\sigma_{AWGN}^2 + \sigma_{ICI}^2} \quad 3-28$$

We considered 21 subcarriers PM-QPSK modulated with 2^{16} symbols each, transmitted in 37 spans of optical fiber, assuming a sampling rate of 8 sample per symbol for digital equalization of linear effects and without considering nonlinear effects. The RX bandwidth is 30 GHz. In simulation it is added white noise before the AWG with $OSNR_k$ for the k th subcarrier defined as in 3-13.

The relation between SNR and OSNR for two-polarization and the bit-error rate (BER) for k th subcarrier is given as in [3]:

$$OSNR_k = \frac{R}{B_{ref}} SNR_k \quad 3-29$$

$$BER_k = \frac{2}{\log 2(M)} \left(1 - \frac{1}{\sqrt{M}}\right) \operatorname{erfc} \left(\sqrt{\frac{3}{2} \frac{SNR_k}{(M-1)}} \right) \quad 3-30$$

where M is the constellation size ($M=4$ for QPSK and $M=16$ for 16-QAM modulated signal).

In Figure 3-23 is shown the plots of $\log(\text{BER})$ versus the OSNR, obtained with the analytical model of 3-28 (blue line), numerical simulations (black line) and theoretical curve of 3-30 (red line) for different value of frequency offset ΔF GHz. We observe very good agreement between the analytical results and simulated one, except when $\Delta F = 2$

GHz, where the simulated results give approximately 0.5 dB penalty at $\log(\text{BER}) = -3$. If ΔF increase more than 2 GHz the system show more than 3

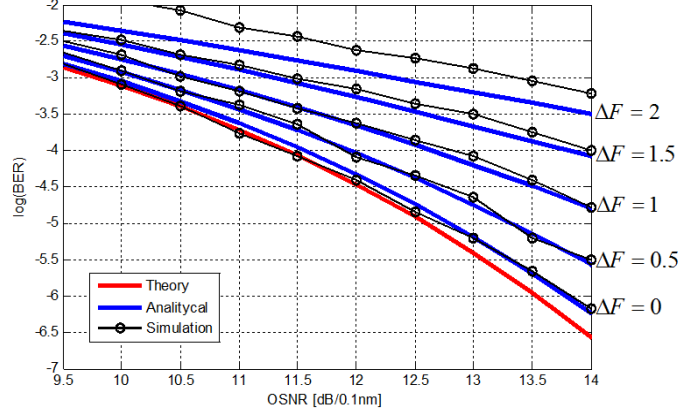


Figure 3-23: Log(BER) versus OSNR [dB/0.1nm] for the theoretical curve (red-line), analytical (blue-line) and simulation (black-line) with different frequency offset value.

dB penalty in terms of OSNR. If $\Delta f_{Tx} = 0$ the AWG center wavelength should change within 2 GHz.

3.4.1.3 Phase noise and EEPN investigation

Assuming we can control the AWG center wavelength precisely with a temperature controller active circuit and also that TX comb is not moving in frequency, 3-22 is re-written as:

$$\hat{X}_k = e^{j(\theta_{LO} + \varphi_{LO})} \left[\frac{1}{T} \int_0^T \left\{ e^{j(\varphi_{Tx})} \sum_{l=0}^{N_s-1} X_l \text{rect}(t) e^{-j2\pi f_l t} + n(t) \right\} e^{j2\pi(f_k)t} dt \right] \quad 3-31$$

As for the frequency offset analyze, it is observed that θ_{LO} and φ_{LO} are outside the integral, and will not affect ICI in de-multiplexing the received AO-OFDM signal. 3-31 is re-written as:

$$\begin{aligned} X_k &= \sum_{l=0}^{N_s-1} X_l H_{A,k} \frac{1}{T} \int_0^T e^{-j2\pi(f_l - f_k)t + j\varphi_{Tx}} dt + n_k \\ &= \eta_0 X_k + \sum_{k \neq l} \eta_{l-k} X_l H_{A,k} + n_k \end{aligned} \quad 3-32$$

where $\eta_0 = |\eta_0|e^{-j\varphi_0}$ is the common phase error (CPE), which is a constant rotation for the received constellation easily corrected in DSP, expressed as $|\eta_0| = E[|\eta_0|] + \zeta$, with ζ residual amplitude noise for each AO-OFDM symbol and $E[|\eta_0|]$ ensemble average. Then 3-32 is re-writing as:

$$\tilde{X}'_k = e^{-j\varphi_0}\tilde{X}_k = \eta_0 X_k + e^{-j\varphi_0} \sum_{k \neq l} \eta_{l-k} X_l H_{A,k} + e^{-j\varphi_0} n_k \quad 3-33$$

where ICI due to phase noise is given as:

$$\eta_{l-k} = \frac{1}{T} \int_0^T e^{-j2\pi(f_l - f_k)t + j\varphi_{Tx}} dt \quad 3-34$$

Again it is assumed ICI is Gaussian distributed and express the SNR per k th subcarrier as:

$$SNR_k = \frac{E[|X_k|^2] \cdot E[|\eta_0|]^2}{\sigma_{AWGN}^2 + \sigma_{ICI}^2} \quad 3-35$$

where the variance of ICI due to phase noise is:

$$\sigma_{ICI}^2 = E[\zeta^2] + E \left[\sum_{k \neq l} |\eta_{l-k}|^2 |X_k|^2 |H_{A,k}|^2 \right] \quad 3-36$$

Following the calculation given in [34] the SNR penalty per k th subcarrier (ΔSNR_k) is given as:

$$\Delta SNR_k = \frac{E[|\eta_0|]^2}{1 + SNR_k - E[|\eta_0|]^2 SNR_k} \quad 3-37$$

It is now compare the SNR penalty per subcarrier originated from the phase noise of adjacent subcarriers, given in Eq. 3-38, between the coherent AO-OFDM proposed here and CO-OFDM, for PM-QPSK modulation in back-to-back (BtB). The results are shown in Figure 3-24 where we observe that AO-OFDM overcome CO-OFDM because the demultiplexing is performed before taking down in base-band the received signal and does not suffer from the phase noise of the received local oscillator.

It is also observed that both systems shows very good performance with respect to the laser linewidth, because of the short duration of the optical OFDM symbol if compared for instance to the electrical one where the duration in time is on the order of microseconds.

As shown by Shieh and Ho in [35], EEPN is the primary source of limitations in dispersion uncompensated (DU) coherent systems, imposing a very tight constrain on the total laser linewidth due to un-compensated CD.

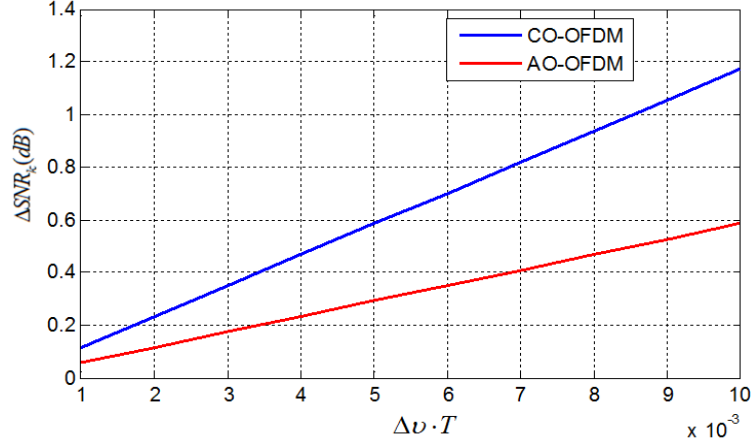


Figure 3-24: SNR penalty per subcarrier (ΔSNR_k) versus the normalized laser linewidth to symbol duration for AO-OFDM (red line) and CO-OFDM (blue line) at a target BER = 10^{-3} .

The impact of EEPN is expressed here in terms of SNR ($SNR_{EEP,k}$) and SNR penalty per k th subcarrier ($\Delta SNR_{EEP,k}$) as:

$$SNR_{EEP,k} = \frac{(1 - \sigma_T^2) \cdot E[|X_k|^2]}{E[|X_k|^2] \cdot \sigma_T^2 + \sigma_{AWGN}^2} \quad 3-39$$

$$\Delta SNR_{EEP,k} = \frac{SNR_{EEP,k} \cdot \sigma_T^2 + 1}{1 - \sigma_T^2} \quad 3-40$$

where $\sigma_T^2 = \pi c(2f_0^2)^{-1} D_t R \Delta\theta$ is the total interference due to intra-symbol and inter-symbol interference, f_0 laser center frequency and $D_t = D \cdot N$ total accumulated CD.

Next is compare the detection of simultaneous 3 subcarriers CO-OFDM versus 1 subcarrier AO-OFDM, both analytical and by simulations after 37 span, corresponding to an accumulated dispersion of 50320 ps/nm. In case of CO-OFDM it is used fixed sinc-shape digital filter to demultiplex the received subcarriers. The $SNR_{EEP,k}$ is chosen to be the ASE limit 9.8 dB corresponding to FEC threshold 10^{-3} . Figure 3-25 reports

$\Delta SNR_{EEP,N,k}$ versus the total laser linewidth obtained with the analytical model of 3-40 (blue line for CO-OFDM and red line for AO-OFDM) and numerical simulation (black line).

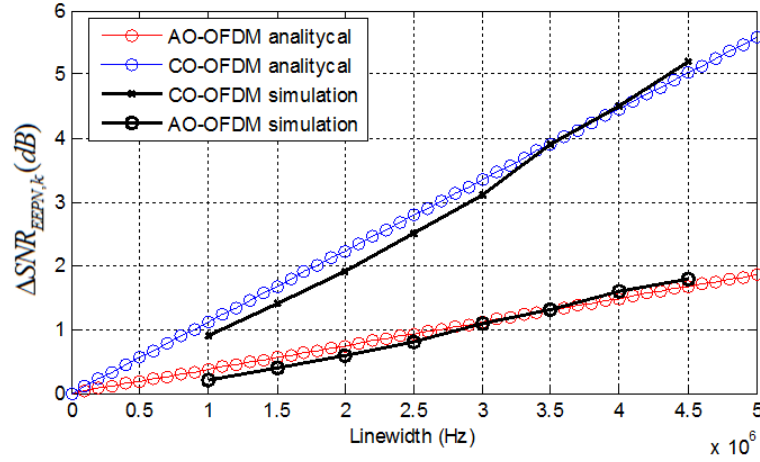


Figure 3-25: SNR penalty per subcarrier ($\Delta SNR_{EEP,N,k}$) due to EEPN as a function of laser linewidth from analytical eq. (21) and simulation results. The system consists of 37span of 80 km SMF fiber with $D=17$ ps/(nm-km).

A very good agreement between the theoretical predictions and numerical simulations for both system considered here is found. EEPN induce a large penalty in CO-OFDM compare to AO-OFDM, because the RX signal bandwidth is increased with a factor of 3. Within 1 dB of penalty a total laser linewidth of 0.9 MHz and 2.5 MHz is find for CO-OFDM and AO-OFDM, respectively. In case of narrow-laser linewidth, less than 0.5 MHz, CO-OFDM shows very small penalty with respect to AO-OFDM and is more convenient to use because only one coherent RX is needed for the de-multiplexing of three subcarrier. However, we should take into account the increasing electrical power consumption and also the impossibility to use more higher order modulation as 16-QAM.

3.4.1.4 Joint FFCPE investigation

The required OSNR at $BER = 10^{-3}$ is investigated for 21-subcarrier PM-QPSK and 7-subcarrier PM-16-QAM modulated signals, transmitted over 37 spans and 9 spans, respectively, as a function of the averaging window length with nonlinear effects also taken into account. Manakov-PMD equation is used for fiber simulation in order to speed

up the time results, with the nonlinear terms reduced of a factor $8/9$. A sampling rate of $6 \cdot R_s$ and $8 \cdot R_s$ for PM-QPSK and PM-16-QAM, respectively, is used. A five pole Bessel filter with 30 GHz bandwidth was used to account for RX electronic limitations. Two different laser linewidths are considered, 300 kHz and 2 MHz. A joint FFCPE between two polarizations is used as in [36]-[38], for phase noise estimation. Results are reported in Figure 3-43. The optimum window length is 31 symbols with similar performance between the two consider laser linewidth. For PM-QPSK modulation shown in Figure 3-26(a), the required OSNR, for a total linewidth of 300 kHz (red line) and 2 MHz (black line), is found to be 11.7 dB and 12.02 dB, respectively. In case of PM-16-QAM shown in Figure 3-26(b), the required OSNR is 17.55 dB for 300 kHz (blue line) and 18.4 dB for 2 MHz (green line) laser linewidth. Within 1 dB of penalty the joint FFCPE scheme for PM-16-QAM can tolerate a total laser linewidth per symbol duration of 2×10^{-4} , where in case of PM-QPSK modulation this penalty is find to be within 0.4 dB.

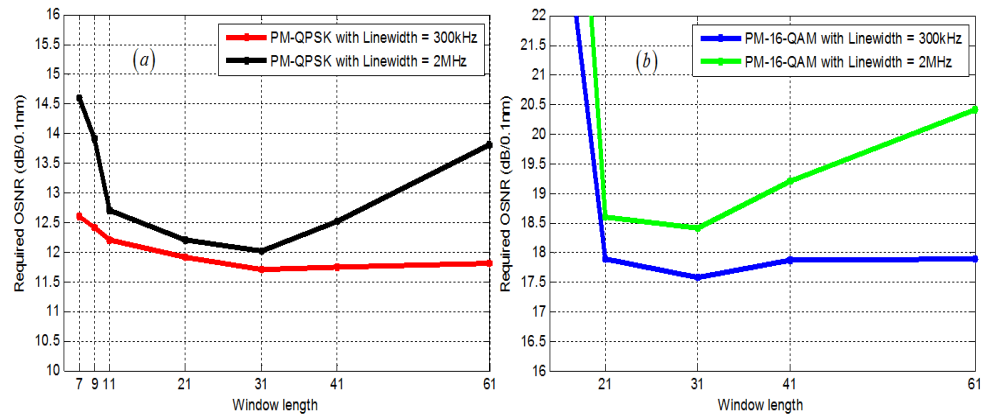


Figure 3-26: Required OSNR corresponding to a FEC threshold of 10^{-3} BER as a function of the averaging window length. (a) PM-QPSK modulation with a linewidth of 300 kHz (red line) and 2 MHz (black line) after 2960 km. (b) PM-16-QAM modulation with a linewidth of 300 kHz (blue line) and 2 MHz (green line) after 720 km.

3.4.1.5 Bandwidth and sampling rate requirements

The required OSNR as a function of RX bandwidth in BtB and after 37 spans, for 21-subcarriers PM-QPSK modulated, is shown in Figure 3-27, accounting also for nonlinear effects. Two different sampling rate are investigated, equal to $4 \cdot R_s$ and $6 \cdot R_s$ for PM-

QPSK modulation only due to current ADC sampling rate limitations. The total laser linewidth was fixed to 300 kHz. To compensate for CD, a FDE equalizer with a FFT-size

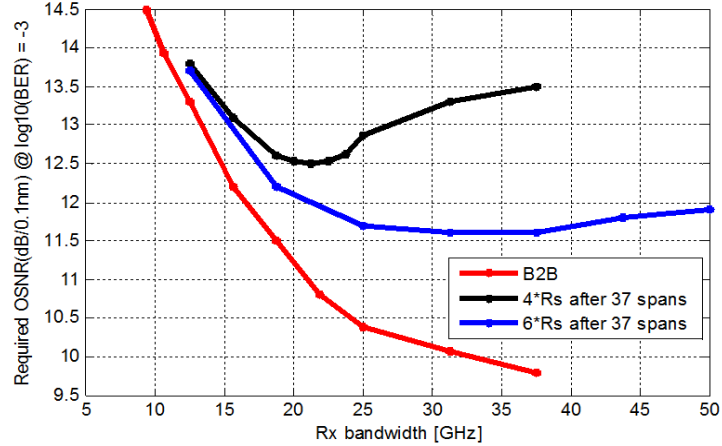


Figure 3-27: Required OSNR as a function of the RX bandwidth in back to back (BtB) shown in red line, after 37 spans for a sampling rate of $4 \cdot R_s$ (black line) an $6 \cdot R_s$ (blue line).

equal to 2048 is used. Four FIR filters $T/2$ spaced with 13-taps each are used for PMD equalization, and phase noise estimation with a window length of 31 symbols.

When using 4 sample per symbol the required OSNR is 12.5 dB and further increase if RX bandwidth become greater than 23 GHz. This is a non-trivial result, and show that the RX bandwidth must be chosen carefully in order to not have additionally OSNR penalty. When 6 sample per symbol are used the required OSNR is 11.7 dB for a RX bandwidth of 25 GHz. Even in this cases, if the RX bandwidth is greater than 37 GHz the required OSNR tend to increase.

3.4.1.6 Frequency domain equalizer and power consumption estimation

The algorithm for AO-OFDM, as for N-WDM, are in principles well known and commonly used offline for experiments or sometimes even used in a real-time field programmable gate array (FPGA) implementation. The main limitation is the computational complexity and power consumption. In this work we used two FDE for CD compensation, for each polarization, employing the overlap and save block wise

algorithm, assuming the total accumulated CD is known a priori. We divide the received signals in blocks, called FFT-size, with an overlap fixed to half size of the block. We then take the FFT of each block and multiply by the inverse fiber transfer function. By

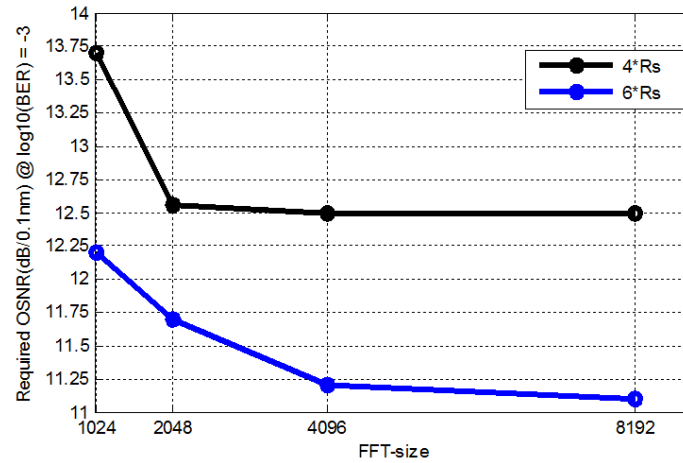


Figure 3-28: Required OSNR as a function of FFT-size after 37 spans for a sampling rate equal to $4 \cdot R_s$ (black line) and $6 \cdot R_s$ (blue line).

taking the IFFT we are able to obtain the transmitted signals. In Figure 3-28, the required OSNR at $\text{BER} = 10^{-3}$ as a function of the FFT-size after 37 spans when 21 subcarriers PM-QPSK modulated are transmitted, for two different sampling rate, $4 \cdot R_s$ (black line) and $6 \cdot R_s$ (red line) is shown.

When using 6 sample per symbol (corresponding to a sampling rate of 75 GSa/s) we obtain better performance in terms of required OSNR, as expected. If FFT-size is equal to 2048 we gain 0.85 dB compare to 4 sample per symbol (corresponding to 50 GSa/s).

If FFT-size is equal to 4096 we gain more than 1 dB in case of 75 GSa/s sampling rate, but on the other hand the computational complexity together with power consumption will also increase.

The computational complexity, as number of real multiplications/sum per bit, with $N_{FFT} = 2048$ and sampling rate of 50 GSa/s is calculated. A FFT with 2048 points needs 32776 real multiplications and 61444 real additions. In frequency domain we used 2048 complex taps for chromatic dispersion compensation, equal to 8192 real multiplication and 4096 real additions. After transforming back to time domain, using a 2048 IFFT, we find the total number of operations as 73744 real multiplications and 126984 real

additions. At the output of the filter we have 1024 sample T/4 spaced, giving 144.01 real multiplications per bit and 248.03 real additions per bit for a PM-QPSK AO-OFDM signal. Following the Savory method [39], we find an average energy per bit 392pJ and a power dissipation on an application specific integrated circuit (ASIC) of 17W. We used four FIR filters with 13 taps T/2 spaced each for PMD equalization, giving a maximum of 39 complex multiplications per bit. These complex multiplications require 156 real multiplications and 78 real sums, giving an approximate power dissipation of 13.5W.

3.4.1.7 Nonlinear performance

In recent years, there have been a lot of efforts to accurately predict the performance over DU links modeling the nonlinear interference (NLI) originated by Kerr effects as additive Gaussian noise [40]-[43]. Among several approach the most utilized is the one proposed by Poggiolini and his group [44]. In demonstration of the Gaussian noise (GN) model, they were able to accurately estimate the NLI power spectral density (PSD) function assuming a rectangular power spectrum signal, like the one of N-WDM transmission, in order to obtain a close-form solution and to clarify different integration regions. Unfortunately, in AO-OFDM system the subcarrier spectra is *sinc*-shaped, and a close-form solution is not possible to achieve. It is expected that GN model will under-estimate the NLI PSD in AO-OFDM. Shieh and Chen in [45] assumed a CO-OFDM transmission and they demonstrated a PSD, expressed in a close-form solution, very similar to GN model assuming a discrete spectrum. They arrived at apparently similar results with completely different demonstration, which they call under ‘dense subcarrier’ assumptions, where subcarriers spacing smaller than the total bandwidth is considered. In both models the NLI is assumed as additive Gaussian noise statistically independent from the ASE noise, in order to write the following equation for OSNR:

$$OSNR = \frac{P_{Tx,sub}}{P_{NLI} + P_{ASE}} \quad 3-41$$

where $P_{Tx,sub}$ is the launch power per AO-OFDM subcarrier for both polarization, P_{ASE} and P_{NLI} are, respectively, the ASE and NLI noise power defined in $B_{ref} = 12.5$ GHz bandwidth. The noise power is given by: $P_{ASE} = G_{ASE} \cdot B_{ref}$, with $G_{ASE} = N \cdot (G-I) F h \nu$, G

gain, F noise figure, h Planck constant and ϑ the frequency. We re-write the Shieh model in a way similar to Poggiolini model, and the two NLI noise power are given below as:

$$P_{NLI,Pogg} = \left(\frac{2}{3}\right)^3 N \gamma^2 L_{eff} P_{Tx,ch} \frac{\log(\pi^2 |\beta_2| L_{eff} N_s^2 R_s^2)}{\pi \beta_2 R_s^3} B_{ref} \quad 3-42$$

$$P_{NLI,Shieh} = \frac{3}{8} N \gamma^2 L_{eff} P_{Tx,ch} \frac{\log(2\pi^2 |\beta_2| L_{eff} N_s^2 R_s^2)}{\pi \beta_2 R_s^3} B_{ref} h_e \quad 3-43$$

$$h_e = \frac{2(N - 1 + e^{-\alpha L N} - N e^{-\alpha L})}{N(e^{-\alpha L} - 1)^2} + 1 \quad 3-44$$

where L_{eff} is the fiber effective length, L is the fiber span length and h_e is the noise enhancement factor accounting for the FWM interference between different spans. However, in DU links this factor has very small impact and if condition $\alpha L \gg 1$ is satisfied, h_e approaches 1. Apart from the constant 2 inside the natural logarithmic, with very small impact, the main difference between Eq. 3-42 & Eq. 3-45 is just a constant number, $3/8$ and $(2/3)^3$. It is simulated 21 subcarrier PM-QPSK and 7 subcarrier PM-16-QAM corresponding, respectively, to 976.5Gb/s and 651 Gb/s total capacity with 7% FEC overhead. 8 sample per symbol was used for PM-16-QAM and 6 sample per symbol for PM-QPSK. Two, fully uncorrelated, PRBS of 2^{16} symbols were used for each subcarrier in each polarization, and BER was evaluated by direct error counting.

The estimated OSNR required in 0.1 nm for $BER = 10^{-3}$ was 11.7 dB for PM-QPSK and 18.3 dB for PM-16-QAM. Using Eq. 3-41, Eq. 3-42, Eq. 3-43 and Eq. 3-44, we are able to estimate the maximum number of spans for each system. Figure 3-29 reports the performance of the center subcarrier (black dots) and outmost subcarrier (green dots) together with the estimated model of Poggiolini (blue line) and Shieh (red line). From Figure 3-29 we observe for the center subcarrier Shieh model fits better than Poggiolini model which tend to over-estimate the performance in terms of maximum number of span achieved. Both models approximately converge together if we move from the maximum number of span. For the outmost subcarrier, we find out that Shieh model under-estimate the performance and Poggiolini model can be used as a better estimator.

We find an optimal launch power of -6 [dBm] and -5 [dBm] respectively for PM-QPSK and PM-16-QAM. For the outmost subcarrier, PM-QPSK modulated, the maximum distance found is 3280 km and for the center subcarrier 2960 km. In case of PM-16-QAM

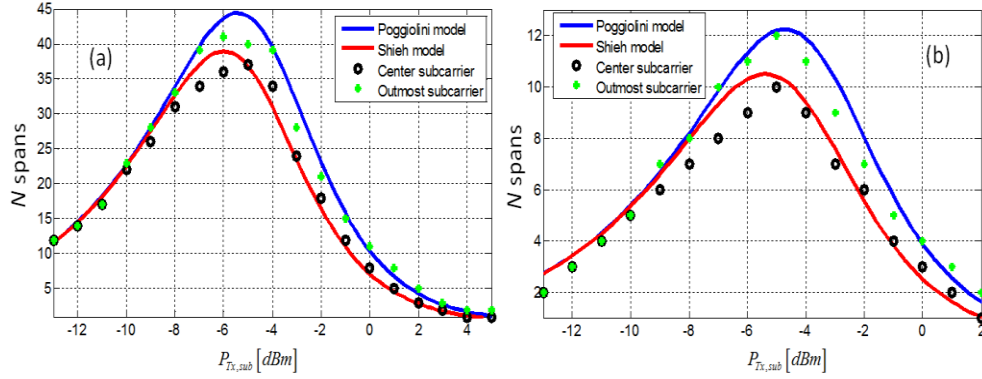


Figure 3-29: Maximum number of spans N as a function of the launch power per subcarrier $P_{Tx,sub}$. (a) 21 subcarrier PM-QPSK modulated. Poggiolini estimation model (blue line), Shieh estimation model (red line), simulated center subcarrier (black dots) and outmost subcarrier (green dots). (b) 7 subcarrier PM-16-QAM modulated. Poggiolini estimation model (blue line), Shieh estimation model (red line), simulated center subcarrier (black dots) and outmost subcarrier (green dots).

modulation, the outmost and center subcarrier have maximum distance, respectively, of 960 km and 800 km.

3.5 Experimental results

In a conventional OFDM scheme, channel orthogonality is achieved only at the time instant that corresponds to the center of the auto- and cross-correlation time waveforms. Time-gating is applied to reduce ICI. However, when an optical OFDM superchannels is transmitted over an uncompensated link, the OFDM subcarriers experience different delays and time-gating is no longer efficient to suppress ICI. Insertion of CP to decrease ICI reduces the overall spectral efficiency. Using a suitable filter shaping at the TX, all the OFDM subcarriers are successfully received, without CP, or CD compensation, or optical time gating. Seven AO-OFDM subcarriers are transmitted over a fiber span, allowing an effective bandwidth sharing among different users, without reducing the

spectral efficiency that is 2 bit/s/Hz. In addition, the RX is largely simplified, and real-time OFDM signal processing is achieved.

A 8-channel 12.5-GHz spaced OFDM system has been already experimentally demonstrated, using an AWG both at TX and RX [46]. In that case, CD largely affect the system performances, and transmission over a length larger of 15 Km was not possible. The combined use of a WSS, with a second-order super-Gaussian transfer function, and an AWG allows us to transmit over a 35-km uncompensated link. It is also observe that the electrical signal shape does not affect the system performances. In fact, the optical signal is a train of Gaussian pulses with 13-ps full width at half maximum (FWHM) and the electrical signal has 80 ps duration (bit rate $B=12.5$ GHz), that is six-times larger.

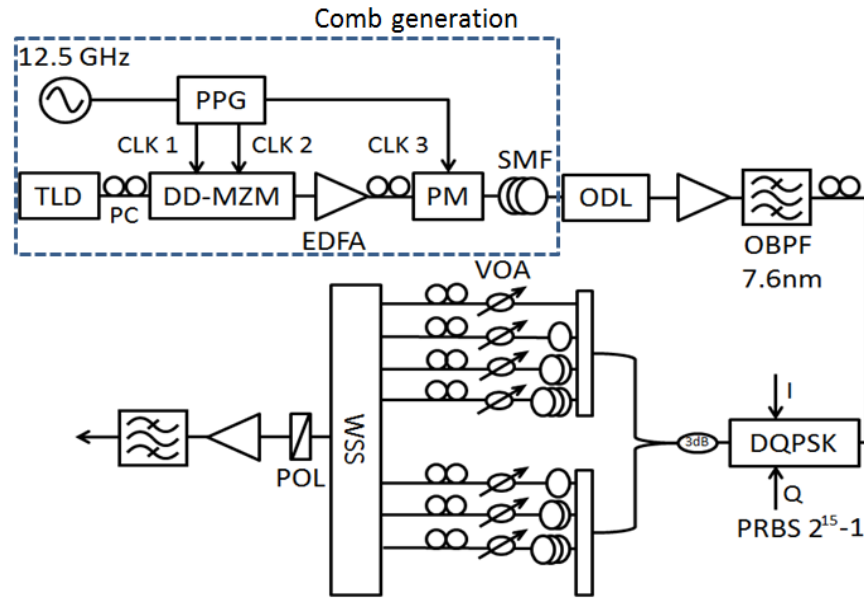


Figure 3-30: Transmitter setup. Tunable laser diode (TLD), polarization controller (PC), dual-drive Mach-Zehnder (DD-MZM), pulse pattern generator (PPG), erbium-doped fiber amplifier (EDFA), clock (CLK), phase-modulator (PM), single mode fiber (SMF), optical delay line (ODL), optical band pass filter (OBPF), differential quadrature phase shift keying (DQPSK) modulator, variable optical attenuator (VOA), wavelength selective switch (WSS), polarization scrambling (POL), pseudo random bit sequence (PRBS).

Figure 3-30 shows the TX architecture for a 7-channel DQPSK-modulated AO-OFDM system; the subcarrier spacing equates the symbol rate $B=12.5$ GHz, to achieve the maximum spectral efficiency [47].

The optical comb is generated by a tunable laser diode (TLD) centered at 1550.259 nm, followed by a DD-MZM, an optical phase modulator (PM) and a single mode fiber (SMF) that compresses the optical pulse. The two cascaded modulators are driven both at $B=12.5$ GHz. The peak to peak voltages, $V_{pp,i}$, at the outputs of the two RF driver amplifiers of the DD-MZM are 8.3 V and 11 V; the phase modulator is driven by a signal with 5.6 V peak to peak, to increase the overall modulation index. Numerical and analytical demonstration detail is given below, supported by experimental results. After the PM modulator, a 3-km SMF used for pulse compression, an optical delay line (ODL) to synchronize the optical pulse peak with the electrical signal, an erbium-doped fiber amplifier (EDFA) and an optical band pass filter (OBPF) are employed.

A DQPSK signal is obtain by precoding two $2^{15}-1$ pseudo random data sequences (PRBS) for the in-phase (I) and quadrature (Q) signals, that are sent to a pulse pattern generator (PPG). The total optical power before the optical DQPSK modulator is 5 dBm, and the modulator insertion loss is 8 dB. All the optical comb lines are modulated by the same electrical signal, and the seven subcarriers are generated using a 3 dB coupler followed by two 6 dB couplers; variable optical attenuators (VOA) are used to equalize the subcarriers power, polarization controller (PC) and delay lines are used to decorrelate the seven optical signals. The lengths of the decorrelation delay lines are 1, 2, 3, 4, 5 m.

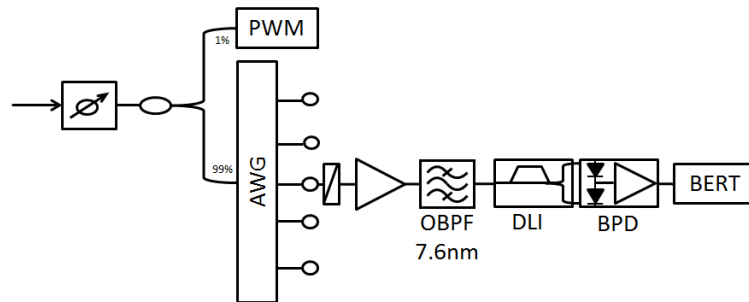


Figure 3-31: Receiver setup. Power meter (PWM), arrayed waveguide grating (AWG), delay line interferometer (DLI), balanced photodetector (BPD), bit-error rate tester (BERT).

In this way, we achieve a full subcarrier decorrelation, and there is not ICI underestimation, as in the odd/even subcarriers approach [48]. A 1x8 WSS with 6 dB

insertion loss is used at the TX. After the WSS a polarization scrambling (POL), an EDFA and a 7.6-nm OBPF are used. The total launched power on the SMF was 2 dBm.

Figure 3-31 shows the RX setup and the system performances are evaluated by attenuating the received power with a VOA, and splitting the signal with a 20-dB coupler before the AWG. The power meter (PWM) measures the 1% of the received power. The AWG has 16 ports, 200 GHz free spectral range (FSR), 12.5 GHz subcarrier spacing and 10 dB insertion loss. We use a pre-amplifier, a 7.6-nm OBPF, a one-bit delay line interferometer (DLI) and a balanced photo-detector (BPD), with 45 GHz bandwidth, to measure the bit error rate (BER). The_BERT tester supports line rates up to 32 Gb/s.

3.5.1 Flat optical comb generation

The setup of comb generation is shown in Figure 3-32. A TLD is used as a CW source. Then a DD-MZM based on LiNbO₃ is used driven by two RF sinusoidal signal generated by a RF synthesizer. RF delay and attenuator are used to control the sinusoidal signal, V_i , entering the DD-MZM. The output electrical field from the DD-MZM can be written as in [49]:

$$E_{out,MZM}(t) = \frac{E_{in}(t)}{2} (e^{-j\varphi_1(t)} + e^{-j\varphi_2(t)}) \quad 3-45$$

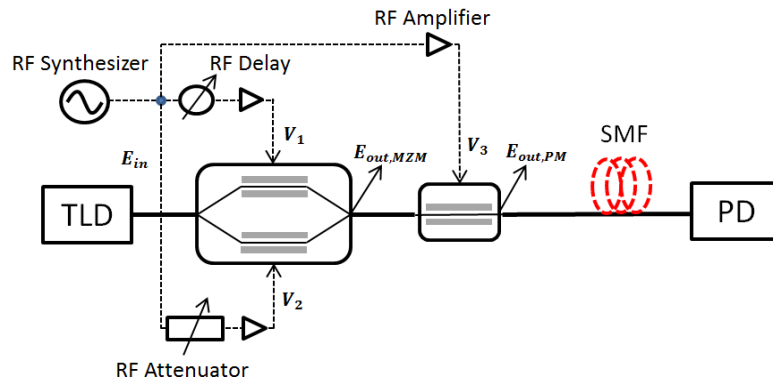


Figure 3-32: Comb generation setup.

where $\varphi_i(t) = \pi V_i(t)/V_\pi$ and V_π is the necessary driving voltage for achieving a phase shift of π . The RF modulation voltage can be expressed as:

$$V_i(t) = V_{ac,i}(t) + V_{dc,i} \quad 3-46$$

where $V_{ac,i}(t) = \frac{V_{ptp,i}}{2} \sin(2\pi ft)$, $V_{ptp,i}$ is the i th peak-to-peak voltage and $f = 12.5 \text{ GHz}$. The DD-MZM will work in the asymmetric mode in order to obtain a chirped signal. Modifying we obtain the asymmetric mode expression:

$$E_{out,MZM}(t) = E_{in}(t) \cos\left(\frac{\varphi_1(t) - \varphi_2(t)}{2}\right) e^{-j \frac{(\varphi_1(t) + \varphi_2(t))}{2}} \quad 3-47$$

where it is observed the chirp factor originated by the exponential term.

To obtain a flat comb generation from a Jacobi Anger expansion which gives the Fourier coefficient of $e^{jz \sin(\varphi)}$ is used, $\sum_{n=-\infty}^{+\infty} J_n(z) e^{jn\varphi} = e^{jz \sin(\varphi)}$, with $J_n(z)$ the n th Bessel function of the first kind. is then written as:

$$E_{out,MZM}(t) = \frac{1}{2} E_{in}(t) \left\{ \sum_{n=-\infty}^{+\infty} J_n\left(\frac{\pi V_{ptp,1}}{V_\pi}\right) e^{j(n\omega t + \frac{\pi}{V_\pi} V_{dc,1})} + J_n\left(\frac{\pi V_{ptp,2}}{V_\pi}\right) e^{j(n\omega t + \frac{\pi}{V_\pi} V_{dc,2})} \right\} \quad 3-48$$

with $\omega = 2\pi f$. It is observed that the magnitude and number of comb lines depend on $V_{ptp,i}$ voltage.

To obtain a flat spectrum condition the following expressions should be respected derived in [50]:

$$\begin{aligned} \frac{\pi}{V_\pi} \frac{\Delta V_{ptp}}{2} &= \frac{\pi}{4} \\ \frac{\pi}{V_\pi} \frac{\Delta V_{dc}}{2} &= \frac{\pi}{4} \end{aligned} \quad 3-49$$

with $\Delta V_{ptp} = V_{ptp,1} - V_{ptp,2}$ and $\Delta V_{dc} = V_{dc,1} - V_{dc,2}$. Eq. 3-49 is further simplified as:

$$\frac{\Delta V_{ptp}}{2} \pm \Delta V_{dc} = V_\pi \quad 3-50$$

In experimental laboratory two identical RF amplifier where available working at 12.5 GHz with a maximum of $V_{ptp,i} = 11.5 \text{ V}$. The first step to obtain a flat comb spectrum together with a Gaussian-like optical pulse in time domain is to fix ΔV_{ptp} in Eq. 3-50. The plus sign is chosen arbitrary from this condition. A rule of thumb is to have different amplitude of $V_{ptp,1}$ and $V_{ptp,2}$ in order to have a well-defined Gaussian pulse with no distortion. Let's fixed this value first as: $V_{ptp,1} = 11 \text{ V}$, $V_{ptp,2} = 8.3 \text{ V}$. Next step it is needed to derive ΔV_{dc} from Eq. 3-50. First it is fixed $V_{dc,1} = 3 \text{ V}$ and finally it is derived

$V_{dc,1} = 0.65$ with $V_{\pi} = 5$ V taken from the DD-MZM datasheet. With all this values fixed at a frequency $f = 12.5$ GHz, Eq. 3-47 is then evaluated by numerical simulation and the normalized output power function $P_{out,MZM}(t) = |E_{out,MZM}(t)|^2$ together with the power spectral distribution (PSD) is shown in Figure 3-33(a) and (b), respectively.

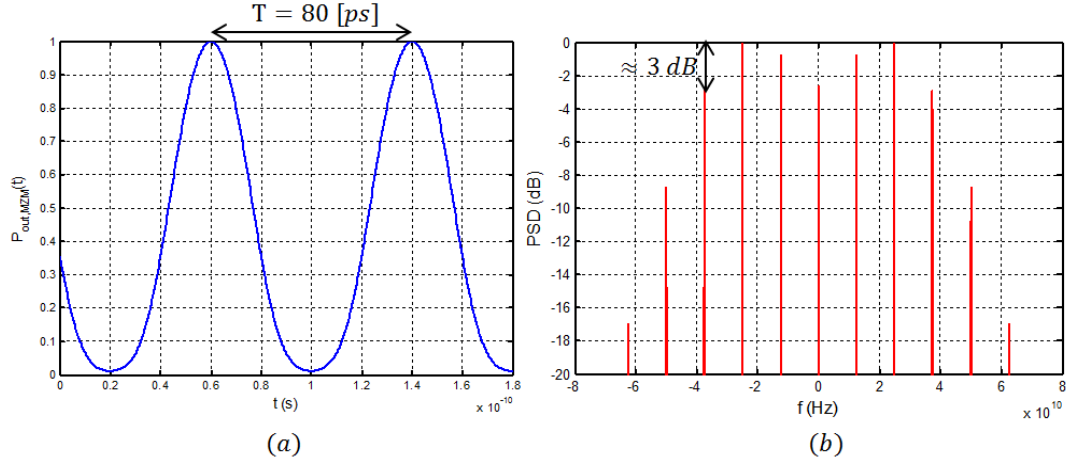


Figure 3-33: (a) Simulated output pulses from the DD-MZM, (b) and its PSD.

From Figure 3-33 it is concluded that in order to use at least 7 subcarriers at 12.5 GHz a DD-MZM is not enough because there is a 3 dB power difference between them. Another optical component is needed to increase the peak-to-peak overall voltage in order to increase the chirp factor. A phase modulator (PM) is used after the DD-MZM as shown in Figure 3-32. The PM is driven by the same RF sinusoidal signal generated from the synthesizer and have no bias voltage. is now written as:

$$E_{out,PM}(t) = \frac{E_{in}(t)}{2} (e^{-j\varphi_1(t)} + e^{-j\varphi_2(t)}) e^{-j\varphi_3(t)} \quad \text{Eq. 3-51}$$

with $\varphi_3(t) = \pi V_3(t)/V_{\pi,PM}$, $V_3(t) = \frac{V_{ptp,3}}{2} \sin(2\pi f t)$ and $V_{\pi,PM} = 6$ V. is written approximately as:

$$E_{out,PM}(t) \cong \frac{1}{2} E_{in}(t) \left\{ \sum_{n=-\infty}^{+\infty} J_n \left(\frac{\pi(V_{ptp,1} + V_{ptp,3})}{V_{\pi}} \right) e^{j(n\omega t + \frac{\pi}{V_{\pi}} V_{dc,1})} + J_n \left(\frac{\pi(V_{ptp,2} + V_{ptp,3})}{V_{\pi}} \right) e^{j(n\omega t + \frac{\pi}{V_{\pi}} V_{dc,2})} \right\} \quad \text{Eq. 3-52}$$

It is expected an increase on the number of comb lines due to the increase of the amplitude ($V_{ptp,i} + V_{ptp,3}$) inside the Bessel functions.

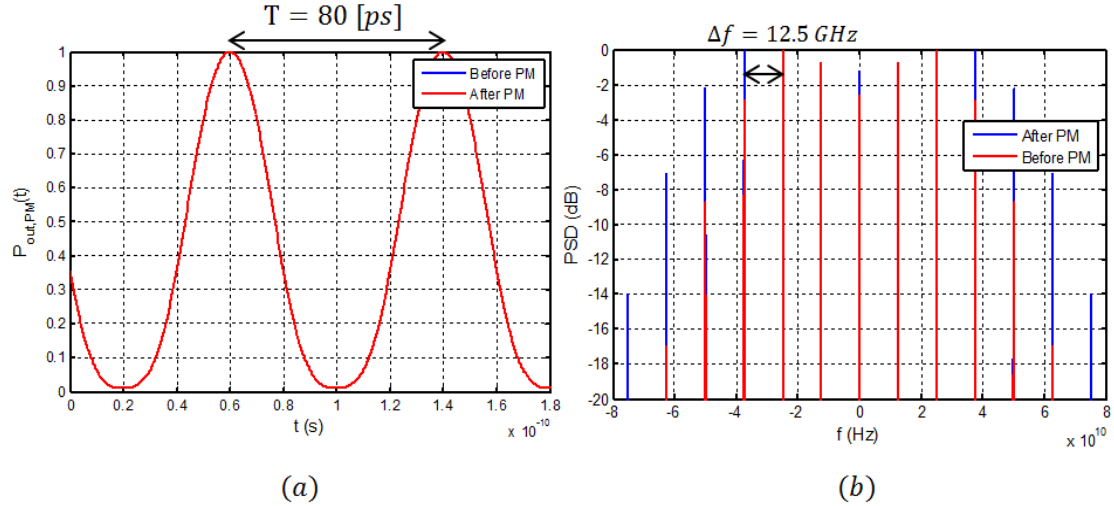


Figure 3-34: (a) Simulated output pulses from the DD-MZM + PM (red line) and only DD-MZM (blue line), (b) and its PSD after the DD-MZM + PM (blue line) and before PM (red line).

Important to note is that flat spectrum condition expressed in will not change from the previous calculation because ΔV_{ptp} is the same. Same simulation is run with $V_{ptp,3} = 5.6$ V and the results after the PM and before is shown in Figure 3-34.

From Figure 3-34(a) it is concluded that if a PM is added there is no change on the output Gaussian-like pulse with same $T = 80$ [ps] and same temporal full width at half maximum (FWHM) $T_{FWHM} = 33.14$ [ps]. For this reason they are totally overlapped in Figure 3-34(a). On the other side from Figure 3-34(b) it is obtained the target number of 7 comb lines with power fluctuation less than 1.6 dB.

Next step is to use a piece of SMF for pulse compression and chirp compensation. In order to estimate analytically the length of the SMF the chirp factor C should be estimated first. For an analytically estimation the chirped Gaussian formula is used to describe the optical pulse after the DD-MZM+PM and it is given as in [51]:

$$U_{out,PM}(0, t) = \exp\left(\frac{-(1 + jC) t^2}{2 T_0^2}\right) \quad \text{Eq. 3-53}$$

where $U_{out,PM}$ is a normalized adimensional amplitude and T_0 is the half width (at $1/e$ intensity point) which is related to T_{FWHM} as: $T_{FWHM} \cong 1.665 \cdot T_0$. The change on the instantaneous angular frequency in Eq. 3-53 is given as:

$$\delta\omega(t) = -\frac{\partial\varphi}{\partial t} = C \frac{t}{T_0^2} \quad \text{Eq. 3-54}$$

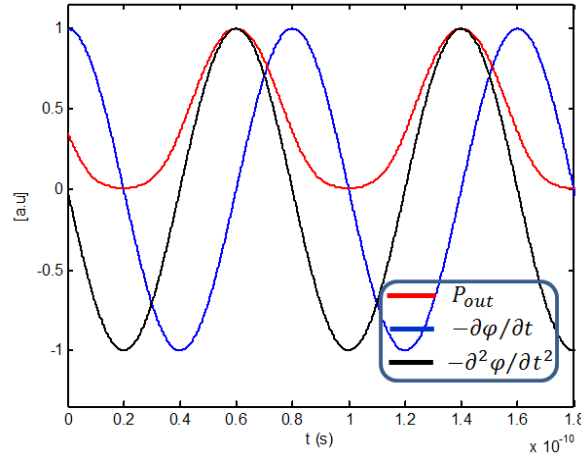


Figure 3-35: Pout (red line), first derivative phase (blue line) and second derivative phase (black line).

with second derivative equal to: C/T_0^2 . The target is the estimation of chirp factor C . To do this it is first simulated in Figure 3-35 the output normalize power, P_{out} , from PM (red line), the first derivative phase, $-\partial\varphi/\partial t$, of $E_{out,PM}$ given in Eq. (blue line) and second derivative phase, $-\partial^2\varphi/\partial t^2$, of $E_{out,PM}$ (black line). It is observed a linear change of $\delta\omega(t)$ in correspondence of Gaussian peak pulse with a second derivative having a maximum. Due to this observation, C is simply find as:

$$C = T_0^2 \cdot \max \left\{ \frac{-\partial^2\varphi}{\partial t^2} \right\} \quad \text{Eq. 3-55}$$

First it is needed to calculate $T_0 = \frac{T_{FWHM}}{1.665} = \frac{33.14 [ps]}{1.665} = 19.904 [ps]$, then from simulation results the $\max \left\{ \frac{-\partial^2\varphi}{\partial t^2} \right\} = 2.5935 \cdot 10^{22}$ is find and finally applying Eq. 3-55 it is found a chirp factor of: $C = 10.2747$.

Once the chirp factor is found, the length of the SMF must be estimated. The width after propagation T_1 is related to the initial width T_0 by the relation [52]:

$$\frac{T_1}{T_0} = \sqrt{\left(1 + \frac{C\beta_2 z}{T_0^2}\right)^2 + \left(\frac{\beta_2 z}{T_0^2}\right)^2} \quad \text{Eq. 3-56}$$

For $C\beta_2 < 0$ the width of the signal initially decrease to a minimum where the chirp factor equal zero and after is monotone increasing. This is due to different contribution chirp sign from second order dispersion and signal chirp. In Figure 3-36 is shown the broadening factor versus the SMF length, in case of a single DD-MZM (blue line) and when employing a DD-MZM plus a PM.

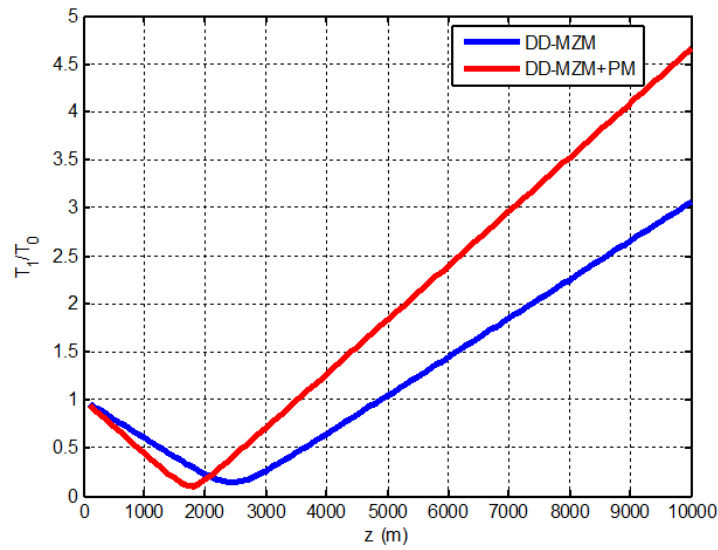


Figure 3-36: Variation of broadening factor T_1/T_0 versus the fiber length z (m) in case of a single DD-MZM (blue line) and cascaded DD-MZM + PM (red line).

To find the required length for a minimum T_1 the following formula is applied:

$$z_{min} = \frac{C}{1 + C^2} L_D \quad \text{Eq. 3-57}$$

where the dispersion length is given as: $L_D = T_0^2/|\beta_2|$. Knowing $C = 10.2747$, $T_0 = 19.904$ [ps] and $\beta_2 = -2.1668 \cdot 10^{-26}$ [s²/m], the required length of SMF is found $z_{min} = 1828.4$ [m] in case of DD-MZM plus PM.

In experimental setup a 2 [km] SMF is chosen and the results are compared with the numerically one shown in Figure 3-37.

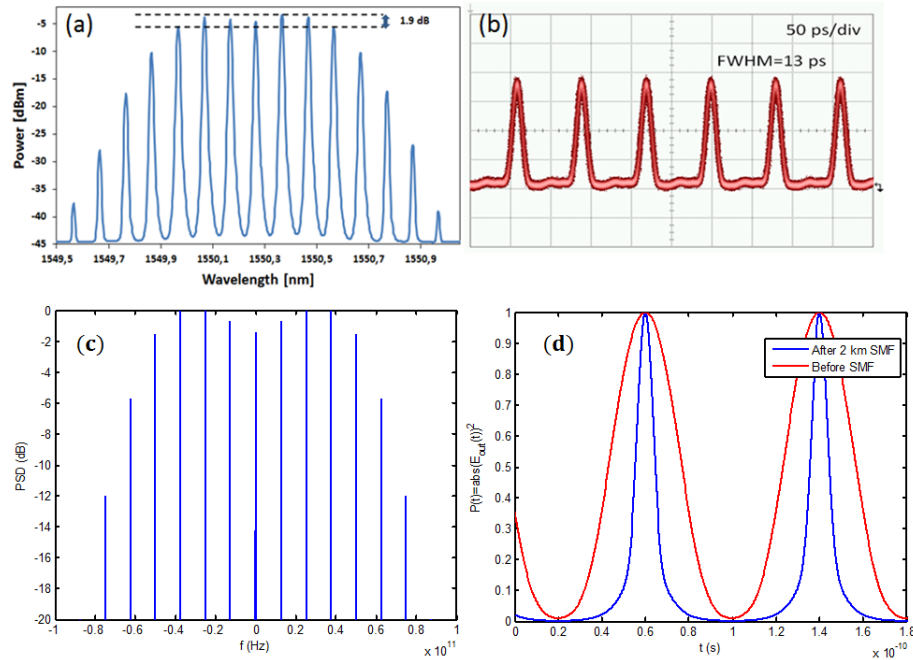


Figure 3-37: (a) Experimental measure optical comb spectrum, (b) time domain Gaussian pulse. (c) Numerical simulation of optical comb PSD and (d)

In Figure 3-37 (a) & (b) is shown the experimental measured optical comb spectrum and Gaussian time domain waveform; in (c) & (d) their numerically simulation results. This result confirm the accuracy of the proposed flat optical comb generation.

3.5.2 Experimental performance evaluation

The Tx and Rx experimental setup was shown in Figure 3-30 & Figure 3-31. The measured eye diagrams for a seven channel system in B2B and after 35-km SMF are reported in Figure 3-38(a) and (b), respectively.

The effect of ICI can be estimated by an inspection of Figure 3-39, where the spectrum at the AWG matched port is shown. Figure 3-39(a) reports the received spectrum at an AWG output port for a transmission of seven AO-

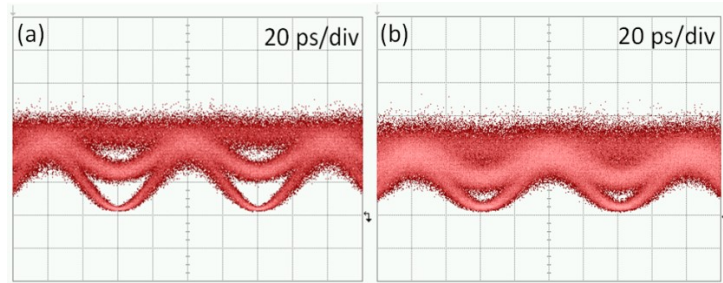


Figure 3-38: Measured eye diagrams of a 7 ch-transmission (a) B2B (b) after 35-km SMF.

OFDM subcarriers, and Figure 3-39(b) refers to the case when the target subcarrier is not transmitted, i.e. measures the ICI at the same port from the other six carriers. The measured crosstalk is -35.6 dBm.

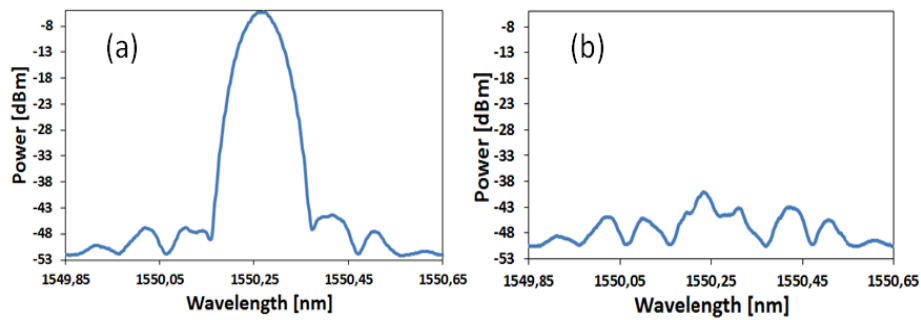


Figure 3-39: Spectrum measured at an AWG output port transmitting (a) seven AO-OFDM carriers (b) six subcarriers (the target subcarrier has been switched off)

Finally, Figure 3-40 and Figure 3-41 report the BER measurements as a function of the total received power. At first, the B2B behavior is compared with the performance obtained with the same setup, but exploiting QPSK modulation and coherent detection. In case of coherent detection, five adjacent subcarriers, spaced 12.5 GHz each, are taken into account

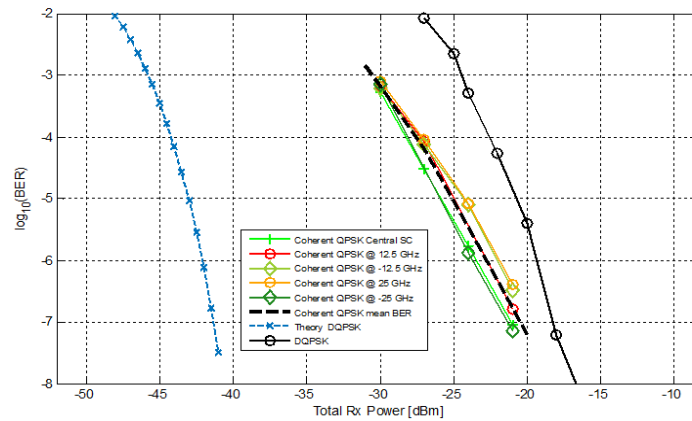


Figure 3-40: BER vs received power in BTB for the DQPSK-modulated subcarrier received with direct detection compared with five QPSK subcarriers received by coherent detection (the dashed line corresponds to the mean BER curve of the five subcarriers). A theoretical curve of BER with direct detection is also shown for reference..

Figure 3-41 reports BER measurements after 20-km, 28-km and 35-km SMF for the single DQSPK modulated subcarrier, without any dispersion compensation. Error-free transmission is achieved for all the experimented subcarriers.

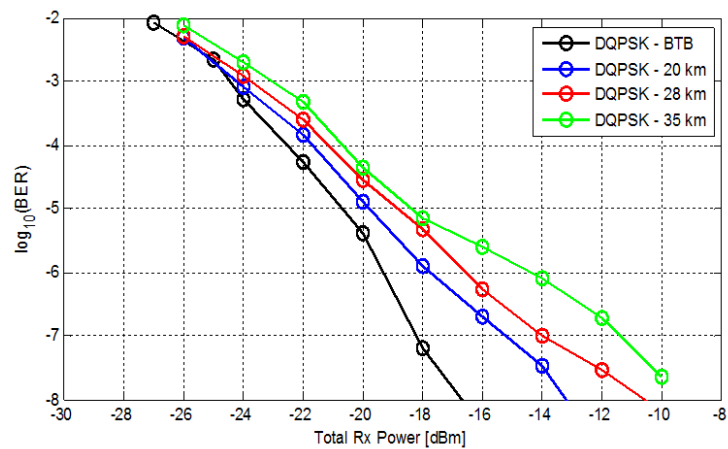


Figure 3-41: BER vs received power for a DQPSK-modulated subcarrier for B2B, 20-km, 28-km, and 35-km transmission over uncompensated SMF.

3.5.3 Experimental comparison between FBG and an AWG

The AO-OFDM analysis is extended considering either an AWG or a fiber Bragg grating (FBG) to demultiplex the AO-OFDM signal. The AWG is used to demultiplex all the subcarriers in parallel, whereas a FBG allows us to select only one subcarrier from the received superchannels. The use of a FBG is advantageous to reduce the costs in optical access networks RXs, or in optical add/drop multiplexer [53].

In Figure 3-42(a) is shown the measured transfer function of an AWG and in Figure 3-42(b) of the FBG. The AWG has 16 ports, 200 GHz free spectral range, 12.5 GHz subcarrier spacing, 10 dB insertion loss and side lobes level 14.1 dB down. FBG has same subcarrier spacing, 20 dB insertion loss and side lobes level 15.6 dB down.

The design of the FBG to perform the DFT operation can be found in [54]. The reflected signal from the FBG has duration equal to the OFDM symbol and consist in a number of short pulses with same amplitude which depend on the number of FBG sub grating and different phases equal to DFT principle. The impulse response of the FBG is approximately equal to refractive index spatial modulation function and the FBG is assumed weakly reflective [55]. For this reason the FBG shows very high insertion loss.

The Tx experimental setup is same as in Figure 3-30. The Rx is different from Figure 3-31 because the VOA which is used to vary the received optical power now is placed

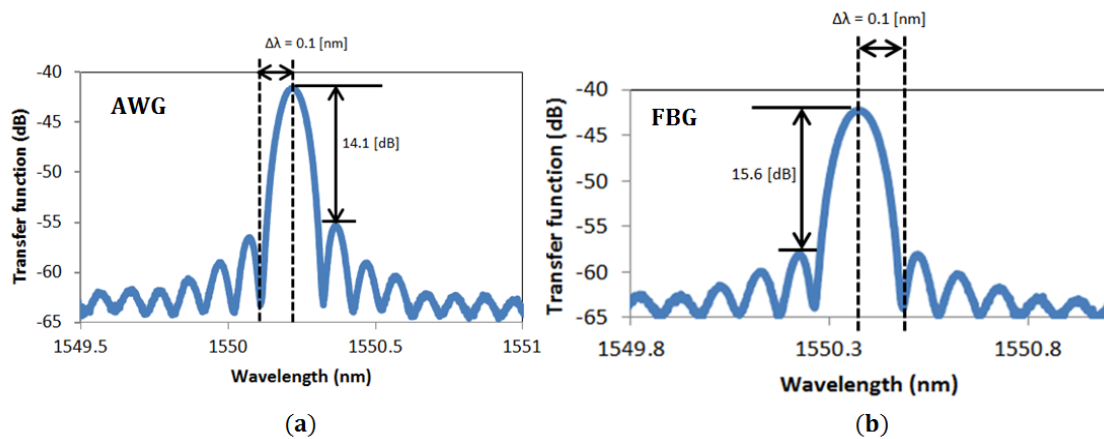


Figure 3-42: Experimental comparison measured transfer function between (a) an AWG and (b) FBG.

after the AWG/FBG DFT filter. A one bit delay line interferometer, followed by a balanced photo-detector with 45 GHz of bandwidth and a limit electrical pre-amplifier, are used to measure the bit error rate (BER). The system performances are evaluated using a bit error rate tester (BERT), which supports data rate up to 32 Gb/s.

Figure 3-43(a) reports the BER measurements as a function of the total received power, when a FBG is used at the RX to extract a single optical subcarrier. The red line refers to the case when only one subcarrier is transmitted in a back-to-back (B2B) setup. In this case, the received optical power for $\log(BER) = -4$ is -17.5dBm . The blue line reports the system performance when two adjacent subcarriers are transmitted in a B2B configuration. From a comparison, we observe that the ICI penalty is 1.5 dB at $\log(BER) = -4$. Adding another subcarrier in the B2B setup, an error floor is reached for $\log(BER) = -8.3$ due to ICI and high loss of the FBG (see green curve). Two and three AO-OFDM subcarriers have been transmitted also over 40 km SMF. In the case of two subcarriers (black curve), error free transmission has been achieved, with a penalty of 2.5 dB , with respect to the B2B case. The same penalty is observed transmitting three subcarriers (cyan curve), but in this case an error floor for $\log(BER) = -7.3$ is reached

Figure 3-43(b) shows the performance of the same system, using an AWG at the RX (instead of a FBG). In this case, we have used either DPSK or differentially quadrature phase shift keying (DQPSK) modulation. In the latter case, the PM in the TX has been replaced by an I/Q modulator, and use the same PRBS. Blue line refers to the DPSK modulation and B2B case, for the center subcarrier, and black and red lines to the other two adjacent subcarriers. As expected, the center subcarrier presents a 1 dB penalty compared to the other two subcarriers, for $\log(BER) = -4$. Also in this case, we have tested the system performance by transmitting over 40 km of SMF. The adjacent subcarriers (green and cyan curves) present about 1.3 dB penalty with respect to the B2B case. For the center subcarrier (yellow curve), the penalty is 2.2 dB . However, in all case, the BER does not present any floor and error-free transmission has been demonstrated using an AWG at the RX. Finally, the last two black curves refer to DQPSK modulation, in B2B and after 20 km SMF; in this case the power penalty after transmission is 1.3 dB for a $\log(BER) = -4$.

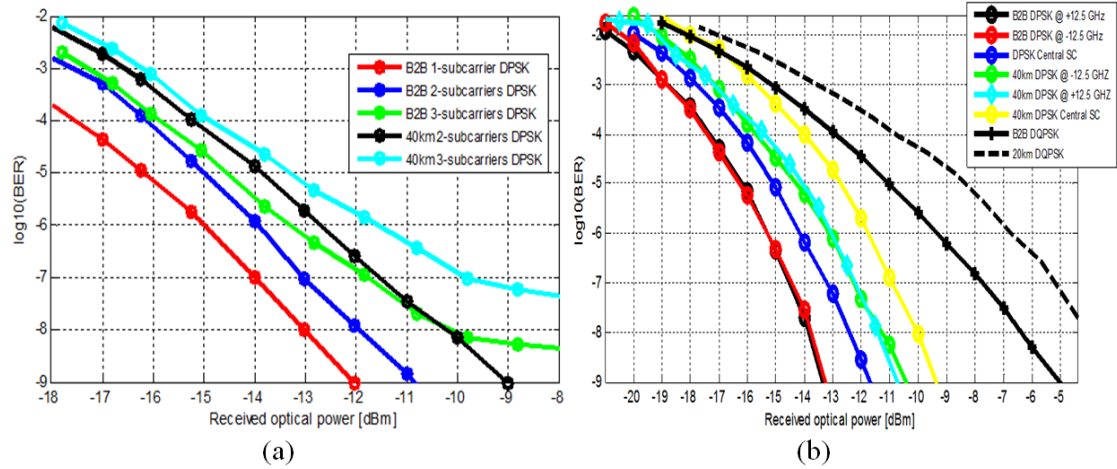


Figure 3-43: (a) BER versus the received optical power for DPSK modulated subcarriers, when a FBG is used at the RX, (b) BER vs. received optical power for DPSK and DQPSK modulation, when an AWG is used at the RX.

3.6 Conclusions

In this chapter, the optical IDFT/DFT principle was investigated. Simulations and experimental performance evaluation have been performed for an AO-OFDM setup with both direct and coherent detection.

The insertion of CP by a WSS largely increase the system performance in direct detection setup with disadvantage of a reduced spectral efficiency. Different number of subcarriers with different modulation where investigated. The AO-OFDM with direct detection can be run online and does not need a DSP circuit. The Rx DFT filter can be integrated in a planar lightwave circuit (PLC). There is no bandwidth limitations either in Tx or Rx.

A carefully investigation of PM AO-OFDM system was performed, using both analytical models and numerical simulations. By using a WSS we can also achieve a flexibility compare to that of a N-WDM. It was experimentally demonstrated, measuring

BER as a function of received optical power, that AWG or WSS must be placed after the passive splitter. Using an AWG at the RX side, 1 GHz of frequency offset with 1 dB penalty can be tolerated, demonstrated analytically and by simulation. It is shown that AO-OFDM suffer less the phase noise and EEPN effects than CO-OFDM, and find out that EEPN is the main limitations for AO-OFDM. It is demonstrated by simulation that in AO-OFDM it is not mandatory to compensate for CD before the demultiplexed subcarrier, which was non trivial result. Using an AWG, as an optical demultiplexer, there is no need for fast adaptive filter or over-sampling in DSP and by using a FDE filter there is no need to introduce CP. FFCPE filter was used for phase noise estimation to evaluate the system performance. Computation complexity of the FDE filter together with estimated power consumption of CD and PMD is investigated. Analytically formula where used to carefully predict the AO-OFDM performance in terms of required OSNR and maximum number of spans using the well-known Poggiolini and Shieh models. Simulation of an AO-OFDM system with 21 subcarriers PM-QPSK and 7 subcarriers PM-16-QAM is performed, finding the optimal launch power and maximum number of span for the center/outmost subcarrier. The results are in very good agreement with the analytically formula, and it is shown that both models are needed for the estimation of the performance in PM AO-OFDM DU links.

It is experimentally demonstrated an error-free real-time transmission of seven DQPSK-modulated AO-OFDM subcarriers, using a WSS in the TX and an AWG at the RX. This configuration allows us to reduce ICI, when optical time gating is not applied and chromatic dispersion is not compensated. In addition, the use of the WSS at TX introduces flexibility in bandwidth assignment, whereas the AWG at the RX can simultaneously demultiplex a large number of subcarriers, presenting a better filtering behavior and maintaining the advantages of AO-OFDM in terms of cost and complexity.

Optical comb generation was evaluated both numerically and by experimental results, showing very good agreement result.

Finally, it was also performed an experimental comparison of an AO-OFDM system, an AWG or a FBG at the RX. It was shown that both systems can achieve 40-km error free transmission, and the power penalty due to ICI has been carefully investigated.

References

- [1] O. Gerstel, M. Jinno, A. Lord, and S. J. B. Yoo, "Elastic optical networking: a new dawn for the optical layer?" *Communications Magazine*, IEEE, vol. 50, no. 2, pp. s12–s20, 2012.
- [2] G. Zhang, M. De Leenheer, A. Morea, and B. Mukherjee, "A survey on OFDM-based elastic core optical networking," *Communications. Surveys Tutorials*, IEEE, vol. 15, no. 1, pp. 65–87, 2013.
- [3] G. Bosco, V. Curri, A. Carena, P. Poggiolini, and F. Forghieri, "On the performance of Nyquist-WDM Terabit superchannels based on PM-BPSK, PM-QPSK, PM-8QAM or PM-16QAM subcarriers," *J. Lightwave Technol.* 29(1), 53-61 (2011).
- [4] G. Bosco, A. Carena, V. Curri, P. Poggiolini and F. Forghieri, "Performance limits of Nyquist-WDM and CO-OFDM in high-speed PM-QPSK systems," *Photon. Technol. Lett.* 22(15), 1129 -1131 (2010).
- [5] A. Napoli, et al., "Next Generation Elastic Optical Networks: the Vision of the European Research Project IDEALIST," *IEEE Communications Magazine*, Vol. 53, No. 2, February 2015.
- [6] J. Hoxha, G. Cincotti, N.P. Diamantopoulos, P. Zakyntinos, I. Tomkos, "All-optical implementation of OFDM/NWDM Tx/Rx", *ICTON 2013*, paper We.D3.1.
- [7] J. Hoxha, G. Cincotti, M. Nazarathy, P. Zakyntinos, I. Tomkos, "Software defined transceivers for high-speed flexible optical networks," *Future Network & Mobile Summit 2013*, Lisbon, Portugal 2013.
- [8] S. Chandrasekhar and X. Liu, "Experimental investigation on the performance of closely spaced multi-carrier PDM-QPSK with digital coherent detection," *Opt. Express*, vol. 17, no. 24, pp. 21350-21361, 2009.
- [9] A. Sano, et al., "30 x 100-Gb/s all-optical OFDM transmission over 1300 km SMF with 10 ROADMs nodes," *ECOC. Berlin, Germany, 2007*, Paper PDS1.7.
- [10] D. Hillerkuss, et al., "26 Tbit s⁻¹ line-rate super-channel transmission utilizing all-optical fast Fourier transform processing," *Nat. Photonics* vol 5, no. 6, pp. 364-371, 2008.
- [11] S. Shimizu, G. Cincotti, and N. Wada, "Demonstration and performance investigation of all-optical OFDM systems based on arrayed waveguide gratings," *Opt. Express*, vol. 20, no. 26, pp. 525-534, 2012.
- [12] A. J. Lowery, J. Schronder, and L. B. Du, "Flexible all-optical frequency allocation of OFDM subcarriers," *Opt. Express*, vol. 22, no. 1, pp. 1045-1057, 2014.
- [13] H. Chen, M. Chen, and S. Xie, "All-optical sampling OFDM scheme for high speed transmission system," *J. Lightwave Technol.* vol. 27, no. 21, pp. 4848-4854, 2009.
- [14] A. Sano, et al., "No-guard-interval coherent optical OFDM for 100 Gb/s long haul WDM transmission," *J. Lightwave Technol.*, vol. 27, no. 16, pp. 3705-3713, 2009.
- [15] Z. Wang, K. S. Kravtsov, Y. K. Huang, and P. R. Prucnal, "Optical FFT/IFFT circuit realization using arrayed waveguide gratings and the applications in all-optical OFDM system," *Opt. Express* 19(5), 4501–4512 (2011).
- [16] G. Cincotti, "What else can an AWG do?," *Opt. Express* 20, B288-B298 (2012).

- [17] G. Cincotti, N. Wada, K.-i. Kitayama, "Characterization of a full encoder/decoder in the AWG configuration for code-based photonic routers-Part I: modelling and design" *J. Lightwave Technol.*, 24, 1, 103-112 (2006).
- [18] A. J. Lowery, and L. B. Du, "All-optical OFDM transmitter design using AWGRs and low-bandwidth modulators," *Opt. Express* **19**(17), 15696-15704 (2011).
- [19] A. J. Lowery, "Inserting a cyclic prefix using arrayed-waveguide grating routers in all-optical OFDM transmitters," *Opt. Express* **22**(9), 9742-9754 (2012).
- [20] A. J. Lowery, J. Schröder, and L.B. Du, "Flexible all-optical frequency allocation of OFDM subcarriers," *Opt. Express* **22**, 1045-1057 (2014).
- [21] J. M. Kahn and K.-P. Ho, "Spectral Efficiency Limits and Modulation/Detection Techniques for DWDM Systems," *IEEE J. Sel. Topics Quantum Electron.*, vol. 10, no. 2, pp. 259–272, Mar/Apr. 2004
- [22] A. Papoulis, *Probability, Random Variables, and Stochastic Processes*, third edition ed. McGraw-Hill, Inc., 1991.
- [23] J. Proakis, *Digital Communications*, 4th ed. McGraw-Hill Engineering/Math, 2000.
- [24] C. Peucheret, "Generation and Detection of Optical Modulation Formats" cpeu@fotonik.dtu.dk.
- [25] Y. Konishi, K. Ishida, K. Kubo, and T. Mizuochi, "True PRBS Transmission of DQPSK by Differential Precoder Employing Parallel Prefix Network," in *Proc. Optical Fiber Commun. Conf. (OFC)*, Anaheim, CA, U.S.A., Feb. 2006, paper OThR3.
- [26] G. Cincotti, "Enhanced functionalities of AWGs," *J. Lightwave Technol.* **33**(5), 998-1006 (2015).
- [27] N. Kataoka, N. Wada, X. Wang, G. Cincotti, A. Sakamoto, Y. Terada, T. Miyazaki, K.-I. Kitayama, "Field trial of duplex, 10 Gbps \times 8-user DPSK-OCDMA system using a single 16×16 multi-port encoder/decoder and 16-level phase-shifted SSFBG encoder/decoders," *J. Lightwave Technol.* **27** (3), pp. 299-305 (2009).
- [28] K. Ishihara, T. Kobayashi, R. Kudo, Y. Takatori, A. Sano, E. Yamada, H. Masuda, M. Matsui, M. Mizoguchi, and Y. Miyamoto, "Frequency-domain equalization without guard interval for optical transmission systems," *Electron. Lett.* **44**(25), 1480-1482 (2008).
- [29] S. J. Savory, "Digital coherent optical receivers: Algorithms and Subsystems," *Selected Topics in Quantum Electronics* **16**(5), 1164-1179 (2010).
- [30] W. Shieh and I. Djordjevic, *OFDM for Optical Communications* (Academic press, 2010).
- [31] G.J. Foschini and G. Vannucci. "Characterizing filtered light waves corrupted by phase noise," *IEEE Trans. Inf. Theory* **34**(6), 1437-1444 (1988).
- [32] M. Sharif and J. M. Kahn, "Variable-bandwidth superchannels using synchronized colorless transceivers," *J. Lightwave Technol.* **32**(10), 1921-1929 (2014).
- [33] S. Benedetto and E. Biglieri, *Principles of Digital Transmission: With Wireless Applications* (Springer US 1999).
- [34] T. Pollet, M. Van Bladel, and M. Moeneclaey, "BER sensitivity of OFDM systems to carrier frequency offset and Wiener phase noise," *IEEE Trans. Commun.* **43**(234), 191–193 (1995).

- [35] W. Shieh and K. P. Ho, "Equalization-enhanced phase noise for coherent detection systems using electronic digital signal processing," *Opt. Exp.* 16(20), 15718–15727 (2008).
- [36] E. Ip and J. Kahn, "Feedforward carrier recovery for coherent optical communications," *J. Lightwave Technol.* 25(9), 2675–2692 (2007).
- [37] F.A. C. Garcia, D. A. A. Mello, and H. Waldman, "Feedforward carrier recovery for polarization demultiplexed signals with unequal signal to noise ratios," *Opt. Exp.* 17(10), 7958–7969 (2009).
- [38] I. Fatadin, and S. J. Savory, "Laser Linewidth Tolerance for 16-QAM Coherent Optical Systems Using QPSK Partitioning," *Photon. Technol. Lett.* 22(2), 631–633(2010).
- [39] S. J. Savory, "Digital signal processing for coherent systems," in *Proc. Optical Fiber Communication Conference (Los Angeles, USA, 2012)*, paper OTh3C7.
- [40] A. Carena, V. Curri, G. Bosco, P. Poggiolini, and F. Forghieri, "Modeling of the impact of non-linear propagation effects in uncompensated optical coherent transmission links," *J. Lightwave Technol.* 30(10), 1524–1539 (2012).
- [41] X. Chen and W. Shieh, "Closed-form expressions for nonlinear transmission performance of densely spaced coherent optical OFDM systems," *Opt. Exp.* 18(18), 19039–19054 (2010).
- [42] A. Bononi, P. Serena, N. Rossi, E. Grellier, and F. Vacondio, "Modeling nonlinearity in coherent transmissions with dominant intrachannel-four-wave-mixing," *Opt. Exp.* 20(7), 7777–7791 (2012).
- [43] L. Beygi, E. Agrell, P. Johannisson, M. Karlsson, H. Wymeersch, and P. Andrekson, "A discrete-time model for uncompensated single-channel fiber-optical links," *IEEE Trans. Commun.* 60(11), 3440–3450 (2012).
- [44] P. Poggiolini, G. Bosco, A. Carena, V. Curri, Y. Jiang, and F. Forghieri, "The GN-model of fiber non-linear propagation and its applications," *J. Lightwave Technol.* 4(32), 100–127 (2014).
- [45] W. Shieh and X. Chen, "Information spectral efficiency and launch power density limits due to fiber nonlinearity for coherent practical OFDM systems," *Photon. Journal* 3(2), 158–173 (2011).
- [46] S. Shimizu, G. Cincotti, and N. Wada, "Chromatic dispersion monitoring and adaptive compensation using pilot symbols in an 8 x 12.5 Gbit/s all-optical OFDM system," *Optics Express*, 22(7), 8734–8741 (2014).
- [47] J. Hoxha, J. Morosi, S. Shimizu, P. Martelli, P. Boffi, N. Wada, and G. Cincotti, "Spectrally-efficient all-optical OFDM by WSS and AWG," *Opt. Exp.*, vol. 23, pp. 10986–10996 (2015).
- [48] L. B. Du, and A. J. Lowery, "The validity of "odd and even" channels for testing all-optical OFDM and Nyquist WDM long-haul fiber systems," *Opt. Express* 20(26), B445–B451 (2012).
- [49] J. C. Cartledge, "Performance of 10 Gb/s lightwave systems based on lithium niobate Mach-Zehnder modulators with asymmetric Y-branch waveguides," *Photon. Technol. Lett.*, vol. 7, pp. 1090–1092, 1995.
- [50] T. Sakamoto, T. Kawanishi, and M. Izutsu, "Asymptotic formalism for ultraflat optical frequency comb generation using a Mach-Zehnder modulator," *Opt. Lett.*, vol. 32, pp. 1515–1517, 2007.

- [51] G. P. Agrawal. "Nonlinear Fiber Optics". Academic Press, third ed., 2001.
- [52] D. Marcuse, "Pulse distortion in single-mode fibers. 3: Chirped pulses," Appl. Opt. 20, 3573-3579 (1981).
- [53] J. Hoxha, G. Cincotti, S. Shimizu and N. Wada, "FBG- and AWG-based AO-OFDM demultiplexing," Photonics in Switching (PS), 2015 International Conference on, Florence, 2015, pp. 82-84.
- [54] H.Chen, M. Chen, and Sh. Xie, "All-Optical Sampling Orthogonal Frequency-Division Multiplexing Scheme for High-Speed Transmission System," J. Lightwave Technol. 27, 4848-4854 (2009).
- [55] P. C. Teh, P. Petropoulos, M. Ibsen, and D. J. Richardson, "A comparative study of the performance of seven and 63-chip optical code division multiple-access encoders and decoders based on superstructured fiber Bragg gratings," J. Lightw. Technol., vol. 19, no. 9, pp. 1352–1365, May 2001.

CHAPTER 4

OFDM BASED ON THE FRACTIONAL FOURIER TRANSFORM

In this chapter we introduce the fractional Fourier transform (FrFT) with applications for optical communications. An introduction to continuous fractional Fourier is given first with its main propriety which will help to understand how to use it in optical communications. A derivation of time lens effect is given and a discrete formula for the FrFT is derived. The performance of polarization multiplexing FrFT with coherent detection is carefully evaluated.

4.1 Continues fractional Fourier transform

The FrFT was first proposed by Namias in [1] and later proper defined in [2]. The FrFT is the generalization of the traditional Fourier transform. Let's define \mathcal{F} as Fourier transform operator and $s(t)$ a time domain signal. $S(f) = \mathcal{F}\{s(t)\}(f)$ is a function of the frequency domain which lie on an axes orthogonal to time domain axes. So operator \mathcal{F} correspond to a rotations by an angle $\alpha = 1\pi/2$ from time to frequency axes. If we apply the operator twice we obtain the original function reversed in time; three time we obtain the Fourier transform with frequency axes reversed and four time we obtain the initial time domain function. This is shown in Figure 4-1.

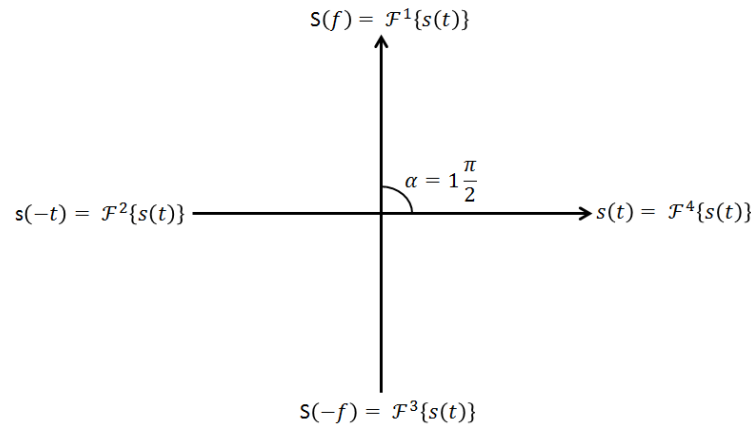


Figure 4-1: Fourier transform of a function in time-frequency plane.

Generalizing this concept over an arbitrary angle $\alpha = p\pi/2$, we can define the FrFT operator as \mathcal{F}^p with $p \in \mathbb{R}$. The p th order of FrFT is the p -th power of Fourier transform. We also suppose that this definition of FrFT is limited to all function that belong to $L^2(\mathbb{R})$ space. In all area of applications where the standard Fourier transform is used, the FrFT find its potential application [3].

In order to exist, \mathcal{F}^p should satisfy 4 propriety: 1) Linear operator 2) Additivity $\mathcal{F}^{a+b} = \mathcal{F}^a + \mathcal{F}^b$ 3) Consistent with Fourier transform operator $\mathcal{F}^1 = \mathcal{F}$ 4) Identity operator $\mathcal{F}^4 = I$. Last propriety is also verified for $p = 0$ due to the periodicity of the operator. To find a definition for the FrFT, where the above propriety are satisfied, we need a complete orthonormal basis defined on $L^2(\mathbb{R})$. We start from the eigenfunctions (eigenvectors) of the

Fourier transform φ , which by definition it is an eigenfunctions if its Fourier transform is equal to the function itself multiply with the eigenvalue (eigenspace) μ : $\mathcal{F}\varphi = \mu\varphi$. To find the possible eigenvalue we re-call the last property of identity and express the eigenvalue as: $\mathcal{F}^4\varphi = \mu^4\varphi \rightarrow I = \mu^4$ finding the four roots of unity: $\mu \in \{1, -j, 1, j\}$ where $j = \sqrt{-1}$. Once we have this eigenvalue we need to define the eigenvector, expressed usually as the Hermite-Gauss orthonormal functions [4]:

$$\varphi_n(t) = \frac{2^{1/4}}{\sqrt{2^n n!}} e^{-t^2/2} H_n(t) \quad 4-1$$

where $H_n(t)$ is the n -th Hermit polynomial and $n \in \mathbb{N}$. There must exist eigenvalues for the corresponding eigenvector to relate them: $\mathcal{F}\varphi_n = e^{jn\frac{\pi}{2}}\varphi_n$ and by taking the p -th power we obtain $\mathcal{F}^p\varphi_n = e^{jpn\frac{\pi}{2}}\varphi_n$. Last relation enable us to express the FrFT using the Hermite-Gauss function. We first expand the function $s(t)$ using the completeness of Hermite-Gauss functions as:

$$s(t) = \sum_{n=0}^{\infty} c_n \varphi_n(t) \quad 4-2$$

where:

$$c_n = \frac{1}{\sqrt{2^n n!} \pi \sqrt{2}} \int_{-\infty}^{+\infty} s(t) H_n(t) e^{\frac{t^2}{2}} dt \quad 4-3$$

We then apply the FrFT operator on both side of Eq. 4-2 and use Eq. 4-3 & Eq. 4-1 to obtain:

$$\begin{aligned} \mathcal{F}^p[s(t)](u) &= \sum_{n=0}^{\infty} \left[\frac{1}{\sqrt{2^n n!} \pi \sqrt{2}} \int_{-\infty}^{+\infty} s(t) \varphi_n(t) e^{\frac{t^2}{2}} dt \right] e^{jpn\frac{\pi}{2}} \varphi_n(u) \\ &= \int_{-\infty}^{+\infty} \sum_{n=0}^{\infty} \frac{e^{jpn\pi/2}}{2^n n! \sqrt{\pi}} H_n(u) H_n(t) e^{-(t^2+u^2)/2} s(t) dt \end{aligned} \quad 4-4$$

Eq. 4-4 can be further simplify if we use the Mehler formula as in [1] in order to obtain a linear integral definition of the FrFT as:

$$S^p(u) = \mathcal{F}^p[s(t)](u) = A^p \int_{-\infty}^{+\infty} s(t) K^p(t, u) dt \quad 4-5$$

where $A^p = \sqrt{1 - j\cos(\alpha)}$ and the kernel defined with constrain $p \notin 2\mathbb{Z}$ as:

$$K^p(t, u) = e^{j\pi t^2 \cot(\alpha)} e^{j\pi u^2 \cot(\alpha)} e^{-j2\pi t u \csc(\alpha)} \quad 4-6$$

The arbitrary rotation takes value on the interval $0 < |\alpha| < 2\pi$ only if $\mathcal{F}^{p=0}[s(t)] = s(t)$ and $\mathcal{F}^{p=\pm 2}[s(t)] = s(-t)$. The kernel is defined in such a way that: $K^{p=4\mathbb{Z}}(u, t) = \delta(t - u)$ and $K^{p=4\mathbb{Z}\pm 2}(u, t) = \delta(t + u)$. It can also be shown that $\lim_{p \rightarrow 0} K^p = \delta(t - u)$, in order to maintain the continuity. When $p = 1$ we obtain the traditional Fourier transform where u , the independent variable of the FrFT, denote this time the frequency domain variable written usually as f .

The inverse FrFT of Eq. 4-5 is:

$$s(t) = \mathcal{F}^{-p}[S^p(u)](t) = A^{-p} \int_{-\infty}^{+\infty} S^p(u) K^{-p}(t, u) du \quad 4-7$$

From Eq.4-7 we conclude that any function who belong to $L^2(\mathbb{R})$ space can be expressed as a linear combination of chirped orthogonal basic function $K^{-p}(t, u)$ with chirp rate $\cot(\alpha)$. For different value of u the basic kernel functions differ by a time shift and a phase factor as:

$$K^p(t, u) = e^{-j\pi u^2 \tan(\alpha)/2} K^p(t - u \sec(\alpha), 0) \quad 4-8$$

We recall some propriety of FrFT [5]-[6] in Table 4-1:

Table 4-1: Propriety of the FrFT..

	$s(t)$	$S^p(u) = \mathcal{F}^p[s(t)](u)$
1	$\delta(t - a)$	$A^p e^{j\pi a^2 \cot(\alpha)} e^{j\pi u^2 \cot(\alpha)} e^{-j2\pi a u \csc(\alpha)}$
2	$\exp(j2\pi t a)$	$\sqrt{1 + j\tan(\alpha)} e^{-j\pi t^2 \tan(\alpha)} e^{-j\pi a^2 \tan(\alpha)} e^{j2\pi t a \sec(\alpha)}$
3	1	$\sqrt{1 + j\tan(\alpha)} e^{-j\pi u^2 \tan(\alpha)}$
4	$y(t) = s(t + a)$	$e^{i\pi \sin(\alpha)(u + a \cos(\alpha)/2)} S^p(u + a \cos(\alpha))$
5	$y(t) = e^{iat} s(t)$	$e^{i\pi \cos(\alpha)(u + a \sin(\alpha)/2)} S^p(u + a \sin(\alpha))$

FrFT is also related to the Wigner distribution (\mathcal{W}) and can be demonstrated the relation: $\mathcal{W}(S^p(u)) = \mathcal{R}^p(\mathcal{W}(s(t)))$ where \mathcal{R}^p is a rotation matrix with an angle α . We give a

graphical interpretation of FrFT in Fig. 4-2, where Wigner distribution $\mathcal{W}\left(\mathcal{F}^p(\delta(t-a))\right)(t, f)$ as a function of original axes (t, f) is shown.

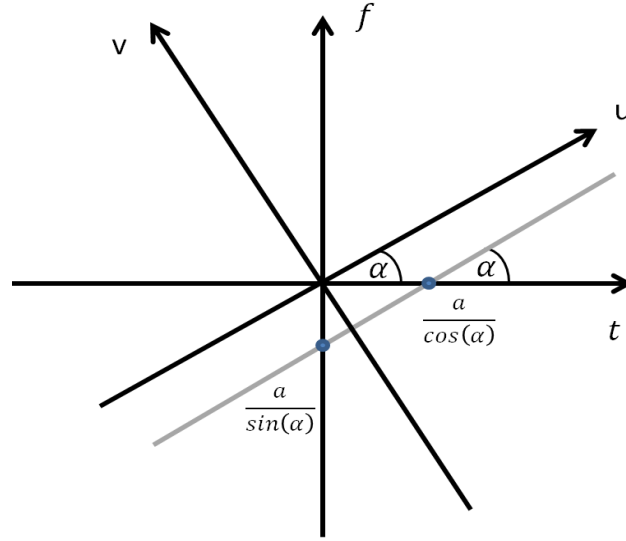


Figure 4-2: Wigner distribution of FrFT kernel function.

We observe the chirp behavior of FrFT kernel in (t, f) plane, where the Wigner distribution is given as: $\mathcal{W}\left(\mathcal{F}^p(\delta(t-a))\right)(t, f) = \delta(tc\cos(\alpha) - a - f\sin(\alpha))$ with a sweep rate equal to $\cot(\alpha)$ [7]. It is evident, from the above relation, that Wigner distribution of $\mathcal{F}^p(\delta(t-a))$ is equal to Wigner distribution of $\delta(t-a)$ rotated by an angle α counterclockwise. This effect of FrFT to rotated the Wigner distribution of the signal is used for filtering in digital signal processing [8].

The last propriety to recall is integral projections of Wigner distribution [9]:

$$|s(t)|^2 = \int_{-\infty}^{+\infty} \mathcal{W}(s(t))(t, f) df \quad \text{Eq. 4-9}$$

Eq. 4-9 state that the integral projections of Wigner distribution, on time domain axes t , is equal to the magnitude square of $s(t)$ on axes t . Same relation can be written for its FrFT, $S^p = \mathcal{F}^p[s(t)](u)$, where Wigner distribution is given as a function of reference axes (u, v) rotated by α :

$$|S^p(u)|^2 = \int_{-\infty}^{+\infty} \mathcal{W}(S^p(u))(u, v) dv \quad \text{Eq. 4-10}$$

Since $\mathcal{W}(S^p(u))(u, v) = \mathcal{W}(s(t))(u \cos(\alpha) - v \sin(\alpha), u \sin(\alpha) + v \cos(\alpha))$ it follows that the integral projections of the Wigner distribution $\mathcal{W}(s(t))$ on u axes, rotated by an angle α with respect to t axes, is equal to the magnitude square of the FrFT function $|S^p(u)|^2$.

4.2 FrFT and the time lens effect

Current optical communications research is mainly focused on two complementary approaches, based on frequency or time multiplexing; orthogonal frequency division multiplexing (OFDM) generates multiple subcarriers, that are transmitted and received in parallel, using (inverse) fast Fourier transform ((I)-FFT) blocks, and Nyquist single carrier time domain scheme, where *sinc*-shaped pulses are spread into adjacent time slots with their rectangular spectra occupying Nyquist bandwidth. These two approaches are complementary and can be describe by the same formalism [10].

The majority complexity and power consumption comes from CD compensation and forward error correction (FEC) module for both optical transmission systems [11,12]. In [13] was demonstrated that both, multicarrier based-OFDM and single carrier, shows same performance in terms of real multiplication and addition per bit if a low over-sampling rate is chosen.

The purpose of this section is to investigate a novel digital multicarrier trasmission system based FrFT [14] for optical communications, which does not require a match filter or a CD compensation module at the receiver (Rx) side. The proposed transmission make use of the time lens effect and CD to convert a multicarrier signal to Nyquist OTDM signal at Rx [15-17], but with no extra optical component or mode-locked laser diode (MLLD) for comb generation.

Compare to OFDM, digital FrFT have approximately equal complexity implementation at the transmitter (Tx) but does not require cyclic prefix, a high number of preambles for channel estimation and pilot tone for phase noise estimation. At Rx it does not require a match filter and CD compensation.

Compare to single carrier transmission, Tx complexity depends on the number of taps from the finite impulse response (FIR) filter if square root raised cosine pulse is used. At Rx, as for OFDM, the proposed approach show less computational complexity.

FrFT should also provide a two-fold benefits; at Tx side adaptive modulation and power assignment for different subcarriers can be chosen easily like in OFDM, which is also the main requirements for a software defined optical network [18], and on the other hand at Rx a compressed optical time domain pulse is obtain making the system more robust to phase noise due to local oscillator. Overall, the proposed FrFT take the best propriety from both traditional transmission but without the need for a CD compensation module.

The signal in a generic multicarrier system is expressed as:

$$s(t) = \sum_{i=-\infty}^{+\infty} \sum_{n=0}^{N-1} S_{i,n} g_n(t - iT) \quad 4-11$$

where T is the symbol period, $S_{i,n}$ is the i th complex information symbol at the n th subcarrier, N total number of subcarriers and $g_n(t)$ is the transmitted waveform for the n th subcarrier given as:

$$g_n(t) = \text{rect}_T(t) \phi_n \quad 4-12$$

with ϕ_n the fundamental basis waveform. This basis are the complex exponential functions, also called harmonics, in case of OFDM transmission. They can easily be recovered if we take the IFFT of a delta function as: $IFFT[\delta(f - f_n)] = e^{-j2\pi t f_n}$.

In optical fiber communications we have a time-invariant frequency selective channel, meaning that different harmonics will travel with different speed which leads to temporal pulse broadening. To avoid ISI and ICI a cyclic prefix (CP) or guard interval is used. The amount of CP depend on symbol rate and fiber length and more it is lower will be the spectral efficiency. To avoid this CP different basis waveform can be used with a precise sweep rate depending on the fiber length. FrFT kernel is used as basis waveform allowing a CD compensation. It turns out that a frequency-to-time conversion is observed at a particular angle α . To find the FrFT basis waveform we must calculate $\mathcal{F}^{-p}(\delta(u - u_n))$, given as:

$$\phi_n = K^{-p}(t, u_n) = A^{-p} e^{j\pi t^2 \cot(\alpha)} e^{j\pi (u_n)^2 \cot(\alpha)} e^{-j2\pi t u_n \csc(\alpha)} \quad 4-13$$

The multicarrier FrFT Tx proposed is shown in Figure 4-3:

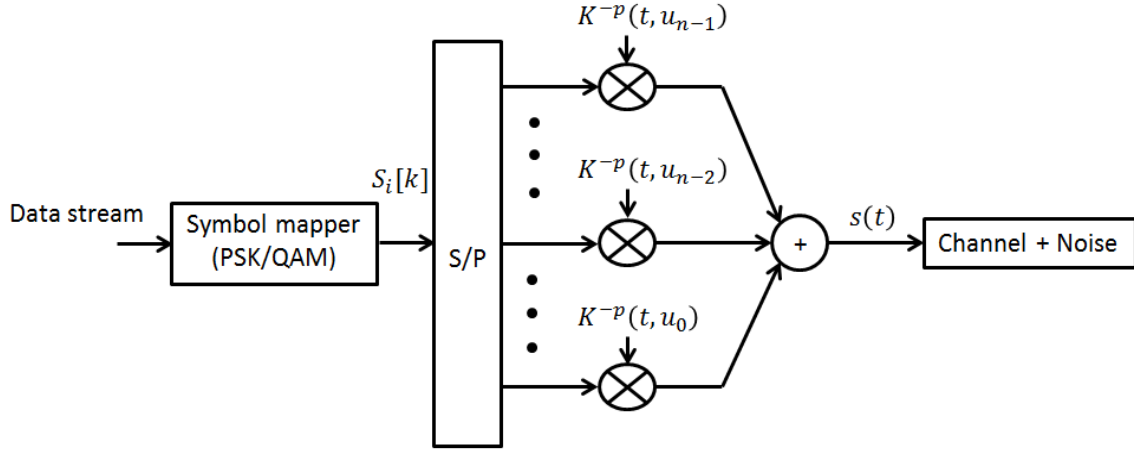


Figure 4-3: Tx Schematic of FrFT multicarrier system.

The FrFT kernel, given in 4-13, is used to replace the harmonics function of the OFDM multicarrier transmission. If time domain is replaced by $\tilde{t} = t \csc(\alpha)$ and Kernel orthogonality is satisfied, $\int_0^{T \csc(\alpha)} K^{-p}(\tilde{t}, u_n) K^p(\tilde{t}, u_m) d\tilde{t} = 0$ for $m \neq n$, we obtain the subcarrier spacing in frequency domain equal to $u_n = \sin(\alpha)/T$ as in [19]. The chirped subcarriers spacing, seen in frequency domain, depend on p -th FrFT domain as a function of $\sin(\alpha)/T$. If $p = 1$ we obtain the OFDM subcarriers spacing $1/T$. If $0 < p < 1$ the subcarriers are more overlapped in frequency domain because the spacing become smaller and in time domain they should become more distant in order to maintain the orthogonality. In the last limit case, when $p = 0$, the subcarriers are totally overlapped in frequency domain and separated in time domain as in a single carrier transmission. So we can conclude that Tx FrFT is the generalization of multicarrier and single carrier transmission.

In this section a novel transmission based on digital FrFT for frequency-to-time conversion (temporal Fraunhofer regime) is proposed. Using the space-time duality theory [15] we can show that the effect of a thin lens in spatial domain is equivalent to a quadratic phase modulation in time domain called *time-lens* effect. It can also be shown

that both dispersive propagation and Fresnel diffraction obey to same parabolic differential equation from a mathematical point of view [20]. Using the space-time duality theory we can better understand the following phenomena which leads to the time-lens effect.

The time lens effect can be used in two regimes, shown in Figure 4-4: a) frequency-to-time conversion and b) time-to-frequency conversion [21]. In the former cases, the time lens is performed before the transmission in optical fiber and this is the fundamental difference between the two regime of operation.

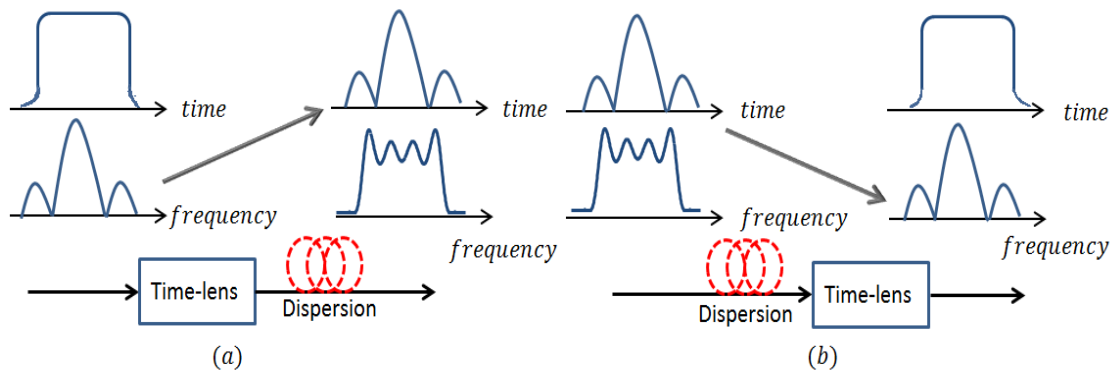


Figure 4-4: (a) Frequency-to-time conversion, (b) time-to-frequency conversion.

To generate a quadratic phase modulation in optical domain, an electro-optic phase modulator or non-linear effects (cross phase modulation or four wave mixing) are usually used. [22].

Electrical FrFT can also generate a quadratic phase modulation. In order to find ‘how much’ should be this phase-modulation for time lens effect, we need to relate the chirp rate with total dispersion consider in the setup. To find this relation the FrFT output is convolved with impulse response of the fiber. Only one subcarrier is consider (one basis $K^{-p}(t, u_0)$) with index $n = 0$ meaning that the spectrum is center in the baseband. The transmitted signal at the end of the optical fiber considering only the second order dispersion is calculated as:

$$\begin{aligned}
g(L, t) &= A^{-p} \int_{-\infty}^{+\infty} g(0, t) e^{j\pi t^2 \cot(\alpha)} e^{-j\frac{\pi c(t-\hat{t})^2}{D\lambda^2}} d\hat{t} \\
&= A^{-p} \int_{-\infty}^{+\infty} g(0, t) e^{j\pi t^2 \cot(\alpha)} e^{-j\frac{\pi c t^2}{D\lambda^2}} e^{j\frac{2\pi c t \hat{t}}{D\lambda^2}} e^{-j\frac{\pi c \hat{t}^2}{D\lambda^2}} d\hat{t} \\
&= A^{-p} e^{-j\frac{\pi c t^2}{D\lambda^2}} \int_{-\infty}^{+\infty} g(0, t) e^{j2\pi c \cot(\alpha) t \hat{t}} d\hat{t} \\
&= A^{-p} e^{j\pi c \cot(\alpha) t^2} g(0, f)
\end{aligned}$$

4-14

where c is the light velocity [m/s], D total dispersion [ps/nm], λ carrier wavelength [nm], L fiber length [m] and $g(0, t) = \text{rect}_T(t)$ pulse envelope. If the condition: $\cot(\alpha) = c/(D\lambda^2)$ [s⁻²] is satisfied we get in last integral expression, the Fourier transform of the initial pulse shape with frequency parameter $f = t\cot(\alpha)$ [Hz]. In the last expression of 4-14, a frequency-to-time conversion is obtained with a time domain waveform at the output of the fiber proportional to initial spectrum multiplied by a phase factor. If we consider all the other subcarriers we obtain the general solution given as:

$$g(L, t) = A^{-p} e^{j\pi c \cot(\alpha) t^2} \sum_{n=0}^{N-1} e^{j\pi (u_n)^2 \cot(\alpha)} g(0, f - f_n) \quad 4-15$$

with $f_n = u_n \csc(\alpha)$. In the next section a discrete FrFT is obtain with same complexity performance like traditional OFDM and simulation results are presented to validate the theory.

4.3 Implementation of digital FrFT

An algorithm to implement the continues FrFT in digital domain is derived based on the method presented in [23]. This algorithm is based on the FFT techniques with a computational complexity $N \log N$. The idea behind this algorithm is to approximate the continuous integral in 4-5 with a sum by sampling the function we want to transform. Do to this we first need to have a definite integral meaning that our function should be restricted in both domains time and frequency plane. This also means that the Wigner distribution of the consider function is limit to a circle by Eq. 4-9. We assume that our

functions $s(t)$ to be transformed is confined to the interval $[-T/2, +T/2]$ in time domain and $[-B/2, +B/2]$ in frequency domain. The limitations on both domains is supported by a *large product* $T \cdot B = N$ which is greater than unity due to uncertainty principle.

A scaling parameter $\xi = \sqrt{T/B}$ is used to normalize both dimensions in order to have the same lengths. Time domain is now scaled as $\bar{t} = t/\xi$ and frequency domain as $\bar{f} = f\xi$. In the new dimensionless domain our signal $s(t)$ is represented in both domains with a length equal to $\sqrt{TB} = \sqrt{N}$. The intervals have length $T = \sqrt{N}$ and $B = \sqrt{N}$, respectively, with sample spaced of $1/\sqrt{N}$ as shown in Figure 4-5.

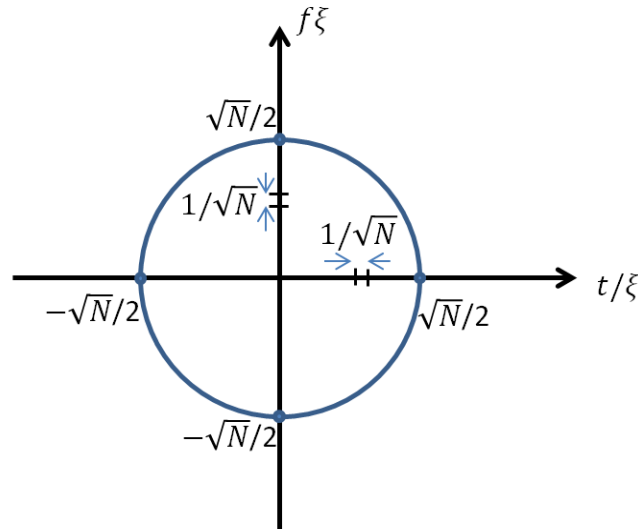


Figure 4-5: Representation of the signal domain in the normalized time-frequency plane.

If the signal have same length in both domains it means that the energy of the signal or its Wigner distribution is confined inside a circle with diameter \sqrt{N} .

Equation 4-5 is re-written as:

$$S^p(u) = A^p e^{j\pi u^2 \cot(\alpha)} \int_{-\infty}^{+\infty} s(t) e^{j\pi t^2 \cot(\alpha)} e^{-j2\pi t u \csc(\alpha)} dt \quad \text{Eq. 4-16}$$

applying the following substitution:

$$\begin{aligned}
& t^2 \cot(\alpha) - 2tu \csc(\alpha) + u^2 \cot(\alpha) \\
&= t^2 (\cot(\alpha) - \csc(\alpha)) + (t - u)^2 \csc(\alpha) + u^2 (\cot(\alpha) - \csc(\alpha)) \\
&= -t^2 \tan(\alpha/2) + (t - u)^2 \csc(\alpha) - u^2 \tan(\alpha/2)
\end{aligned}$$

we obtain:

$$S^p(u) = A^p e^{-j\pi u^2 \tan(\alpha/2)} \int_{-\infty}^{+\infty} e^{-j\pi(t-u)^2 \csc(\alpha)} [s(t) e^{-j\pi t^2 \tan(\alpha/2)}] dt \quad \text{Eq. 4-17}$$

where the signal $s(t)$ is first multiplied by a quadratic phase modulation $e^{-j\pi t^2 \tan(\alpha/2)}$ which results in a almost double bandwidth. This mean that the signal is stretched in opposite direction on frequency domain as shown in Figure 4-6 . This can easily been demonstrated if we consider the bandwidth of the chirp equal to $\tan(\alpha/2)\sqrt{N}$ and take the convolution between Fourier transform of this chirp and our function $s(t)$ (which has bandwidth \sqrt{N}), obtaining a bandwidth of $(1 + |\tan(\alpha/2)|)\sqrt{N} \leq 2\sqrt{N}$ where $|\alpha| \leq \pi/2$.

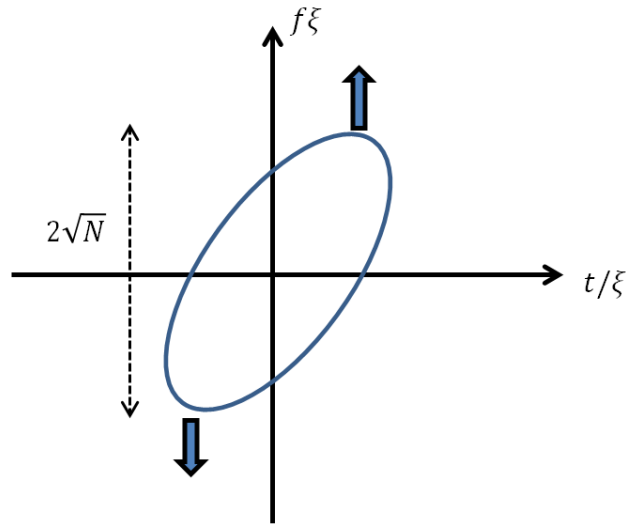


Figure 4-6: Chirp modulation effect on time-frequency plane.

Shannon interpolation is used to represent the discrete sample of $s(t)e^{-j\pi t^2 \tan(\alpha/2)}$, sampled $1/(2\sqrt{N})$ apart to avoid aliasing as:

$$\begin{aligned}
& s(t)e^{-j\pi t^2 \tan(\alpha/2)} \\
& \cong \sum_{n=-N}^N e^{-j\pi \left(\frac{n}{2\sqrt{N}}\right)^2 \tan(\alpha/2)} s\left(\frac{n}{2\sqrt{N}}\right) \text{sinc}\left(2\sqrt{N}\left(t - \frac{n}{2\sqrt{N}}\right)\right)
\end{aligned} \tag{4-18}$$

Performing the integration in Eq. 4-17 after the substitution of 4-18 gives:

$$\begin{aligned}
& S^p(u) \\
& = \frac{A^p}{2\sqrt{N}} e^{-j\pi u^2 \tan(\alpha/2)} \sum_{n=-N}^N e^{-j\pi \left(\frac{n}{2\sqrt{N}} - u\right)^2 \csc(\alpha)} e^{j\pi \left(\frac{n}{2\sqrt{N}}\right)^2 \tan(\alpha/2)} s\left(\frac{n}{2\sqrt{N}}\right)
\end{aligned} \tag{4-19}$$

where the integral is performed over the limit range $0.5 \leq p \leq 1.5$.

In the final step, the sampling is performed on the FrFT domain which gives the desired result:

$$\mathcal{F}^p[s(n)](m) = \tilde{S}^p(m) = \frac{A^p}{2\sqrt{N}} e^{-j\pi \left(\frac{m}{2\sqrt{N}}\right)^2 \tan(\alpha/2)} \sum_{n=-N}^N x(m-n)h(n) \tag{4-20}$$

where $h(n) = s\left(\frac{n}{2\sqrt{N}}\right) e^{-j\pi \left(\frac{n}{2\sqrt{N}}\right)^2 \tan(\alpha/2)}$ and $x(m-n) = e^{-j\pi \left(\frac{n}{2\sqrt{N}} - \frac{m}{2\sqrt{N}}\right)^2 \csc(\alpha)}$. The sum in 4-20 is a discrete convolution that can be performed as a multiplication in Fourier domain using the fast algorithm FFT with computational complexity $N \log N$. Because the summation goes from $-N$ to N an interpolation and decimation of factor 2 is needed. The implementation begins with N samples spaced $1/(\sqrt{N})$, then an interpolation matrix \mathbf{J} of 2 is performed to obtain $2N$ samples spaced $1/(2\sqrt{N})$. After performing 4-20 a decimation matrix \mathbf{D} of 2 will return N samples, because the procedure should start and finish with the same number of samples. This can all be written as:

$$S^p(k) = \mathbf{D} \mathcal{F}^p(m) [\mathbf{J} s(k)] \tag{Eq. 4-21}$$

As stated before, this procedure is derived based on a reduced interval $0.5 \leq p \leq 1.5$. For p outside this interval the additivity property is applied. For $p < 0.5$ the operator is $\mathcal{F}^p = \mathcal{F}^{-1} \mathcal{F}^{p+1}$ and $p > 1.5$ then $\mathcal{F}^p = \mathcal{F}^1 \mathcal{F}^{p-1}$. For this interval the complexity is increased to $2N \log N$ because we need one more FFT. Overall, the discrete FrFT can be reassumed in three main operations: 1) A pre-chirp multiplications 2) A chirp convolution 3) Post-chirp multiplications.

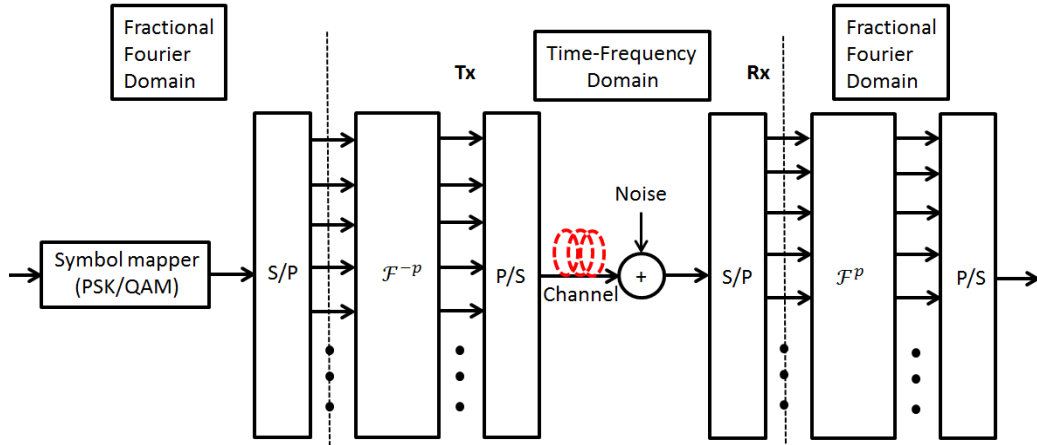


Figure 4-7: Multicarrier FrFT for optical communications.

A multicarrier transmission is then proposed based on 4-20 and Eq. 4-21, shown in Figure 4-7, with the help of the operator \mathcal{F} which perform the operation in Eq. 4-21. At Tx an inverse FrFT (\mathcal{F}^{-p}) is performed after the serial-to-parallel (S/P) block and at Rx the FrFT (\mathcal{F}^p) as a match filter is applied to recover the Tx symbols [14].

However, as explained in section 4.2, if we apply the frequency-to-time conversion we can drastically reduce the computational complexity because it is no needed to apply at Rx the FrFT as the frequency information is now in time domain. For $p < 0.5$ we immediately save $2N \log N$ complex multiplication. As shown later, this is not the only benefit. Due to the pulse compression, the proposed system is very robust to local oscillator phase noise in a coherent detection Rx. On the other hand, for both the benefits there are some constrain. For instance, the length of the fiber should be relatively fixed to same value in relation to the symbol rate consider because the amount of chirp is directly related to it. To estimate the phase noise we should first estimate a different phase offset for each subcarrier in parallel before any other algorithm which estimate phase noise is applied. In case of polarization multiplexing (PM) transmission, the equalization algorithm, which is applied before the phase noise, is not effected by the phase offset because it works on modulus of the received signal. Chromatic dispersion algorithm is not required.

4.4 Coherent optical communications based on PM-FrFT

In this section a novel coherent optical communications based on digital polarization multiplexing (PM) FrFT with time lens effect is investigated, shown in Figure 4-8.

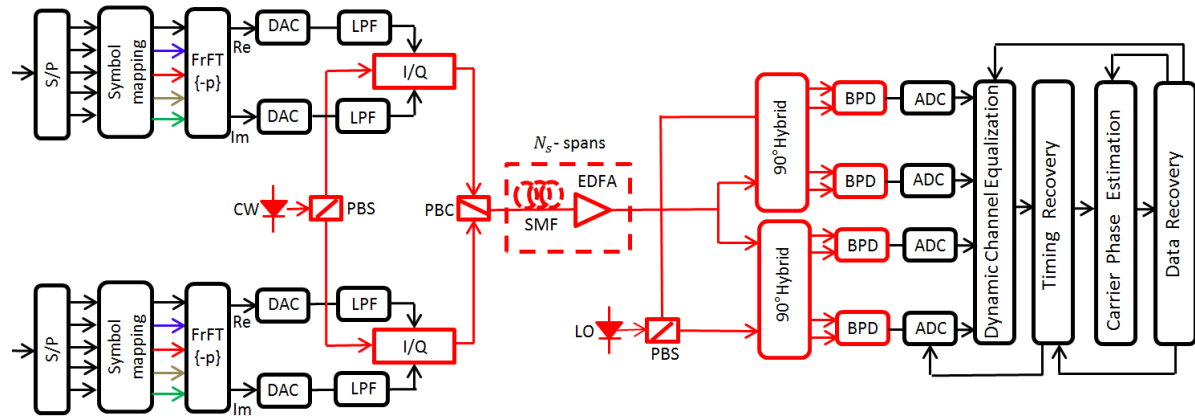


Figure 4-8: Coherent PM-FrFT setup.

Two different data stream, X and Y polarization, are first converted in parallel by S/P, then a symbol mapping is performed in case of complex modulation and finally digital inverse FrFT is taken. A DAC and LPF for aliasing suppression is used to generate an analog waveform. Two different I/Q optical modulator are used to modulate the optical carrier for each polarization. A PBC combine both signals which are transmitted in optical fiber. At the Rx, a LO laser is first separated in two orthogonal polarization which then interfere with the incoming light in a 2x4 90° hybrid whose outputs are detected by two balanced photo-detectors (BPD). In phase and quadrature signals after being low pass filter are sampled by the ADC. In the digital signal processing part the first operation is a dynamic channel equalization which compensate for the polarization mode dispersion (PMD) [24]. Afterwards, timing recovery is performed to synchronize with the symbol rate [25], followed by a digital phase estimation which work with only one sample per symbol. Finally a data recovery is performed. In Figure 4-8 different possible feedback path between the algorithm are also shown. Before evaluating the system performance we first need to estimate the

‘amount’ of chirp rate to compensate for total CD. After frequency-to-time conversion, at Rx Nyquist pulses in time domain are observed and time separation between them need also to be estimated. From 4-14 the condition $\cot(\alpha) = c/(D_t\lambda^2)$ is derived, which relate the total dispersion accumulated with angle α . This condition is not dimensionless and $\cot(\alpha)$ should be dimensionless in order to have a direct relation between total dispersion $D_t = DL$ and $\alpha = p\pi/2$, so a normalization factor is needed. An intuitive way to answer is considering the unit of measurements which is $[1/s^2]$ and realizing that we need a normalize square sampling rate at numerator in order to cancel out. However a proof is given. First it is needed the normalization of time axes $\tau = t/\xi \Rightarrow \tau\xi = t$, same normalization as in section 4.3, and substitute it in fiber impulse response: $e^{-j\frac{\pi c t^2}{D_t \lambda^2}} \Rightarrow e^{-j\frac{\pi c \xi^2 \tau^2}{D_t \lambda^2}}$. Normalization factor is equal to $\xi = \sqrt{T/B} = (T/N)\sqrt{N}$, where T/N is the sampling rate or symbol rate in our case, and when substitute to fiber impulse response: $e^{-j\frac{\pi c T^2 \tau^2}{N D_t \lambda^2}}$ the condition for frequency-to-time conversion is found for a fixed fiber length and symbol rate, given as:

$$\tan(\alpha) = \frac{D_t \lambda^2 N}{T^2 c} \quad 4-22$$

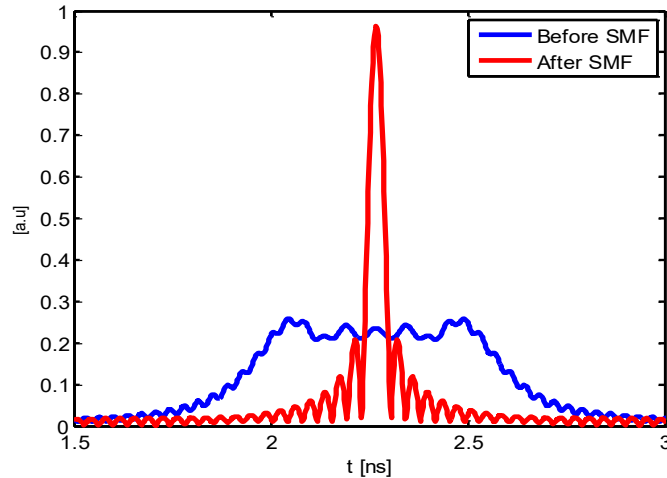


Figure 4-9: Single subcarrier in time domain before and after SMF transmission. To demonstrate this relation a simulation is carry out. The symbol rate is fixed to 28 [Gbaud], the number of subcarriers is $N = 128$ and $p = 0.1$. Only one subcarrier is

transmitted and the result before and after transmission in SMF is shown in Figure 3-43. The total dispersion D_t consider is find inverting 4-22. A compressed *sinc*-shaped Nyquist pulse in red line is obtained as predicted also by 4-14.

Next step is estimation of time separation between Nyquist pulses. Before doing this, it is needed to understand how much the FrFT subcarriers are separated in both frequency and time domain. The subcarriers are orthogonal if they are separated by $\Delta f_p = \sin(\alpha)/T$ in frequency domain, demonstrated in section 4.1. To understand how much they are separated in time domain we recall the 4th propriety on Table 4-1 $y(u) = s(u + T_s) \Rightarrow e^{i\pi \sin(\alpha)(t+T_s \cos(\alpha)/2)} Y(t + T_s \cos(\alpha))$ and conclude that adjacent subcarriers in time domain, after the inverse FrFT, are separated by $\Delta t_p = T_s \cos(\alpha) = T/\cos(\alpha)N$. This separation is also shown in Figure 4-10. To estimate the separation time between adjacent Nyquist pulse (the received symbol rate) the following equation is used, taking into account the fiber group delay:

$$\Delta t = \Delta t_p + \Delta f_p \frac{\lambda^2}{c} D_t = \frac{T}{N} \cos(\alpha) + \frac{\sin(\alpha) \tan(\alpha)}{N} = \frac{T}{N \cos(\alpha)} \quad 4-23$$

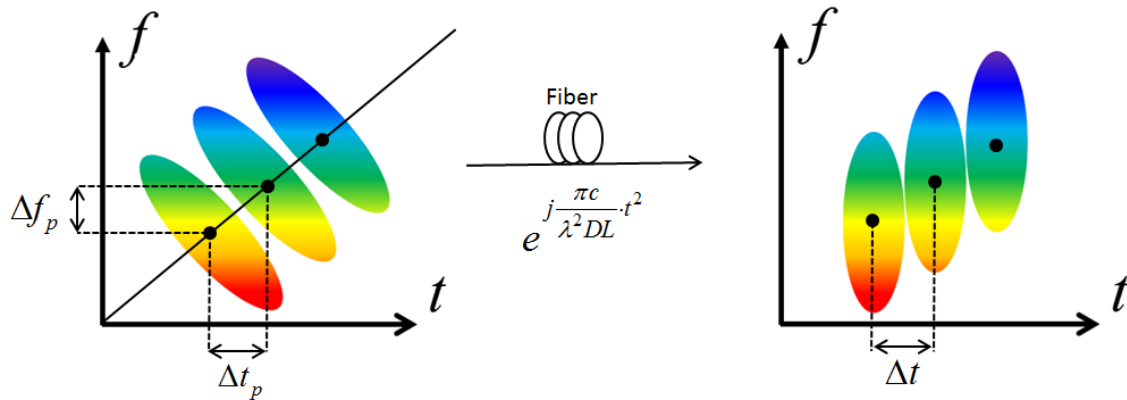


Figure 4-10: Subcarrier separation in frequency and time domain before and after transmission in optical fiber.

A simulation is performed to demonstrate the estimated formula shown in Figure 4-11.

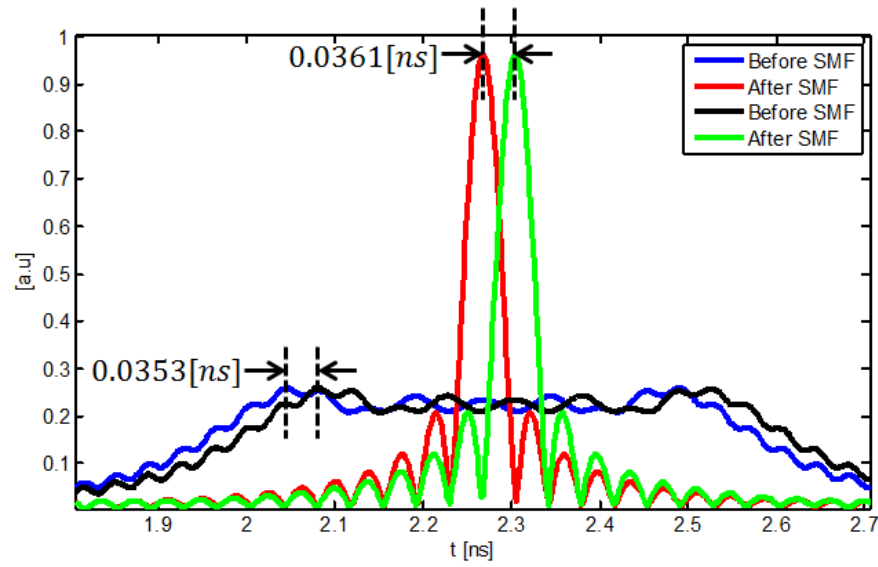


Figure 4-11: Temporal delay between two adjacent subcarrier before and after transmission on SMF.

The system parameters are same as for Figure 4-10. Using the estimated theoretical formula it is found a delay time between two Nyquist pulse after the transmission in SMF of: $\Delta t = 0.0361[ns]$ same as the simulation result shown in Figure 4-11. The delay time before the transmission is also shown which validate the theory prediction: $\Delta t_p = 0.0353[ns]$.

The conversion from multicarrier transmission in Tx to serial optical Nyquist pulse at Rx is obtained with a lower symbol rate because the temporal delay between pulses is higher. The initial symbol rate is 28 Gbaud and the received is 27.7 Gbaud, with a difference of 0.11%. This is related to cosine term in 4-23. If p is very small $\cos(p\pi/2) \approx 1$ the loss in spectral efficiency is very small. But p is related also with the number of subcarriers N and length of the fiber L . A FrFT symbol duration is defined as the number of subcarriers multiply the symbol duration, $T = NT_s$ where $T_s = 1/R_s$ and R_s symbol rate. Applying the frequency-to-time condition we should be aware of not introducing ISI in time and ICI in frequency because it may happen that the received Nyquist pulses in one FrFT symbol are delayed in a way that are received in another symbol FrFT. To avoid this effect the condition $N_{used} \leq N\cos(\alpha)$ must be respected, with N_{used} number of Nyquist pulses received inside one symbol FrFT, which

also correspond to the number of subcarriers to be used at the transmitter side. The number of useful subcarriers used in percent is shown in Figure 4-12(a) as a function of p-FrFT parameter for different total N consider. If p increase the used subcarriers decrease. When $p = 0.3$, the used subcarriers are about 90%. There is no dependence on the symbol rate. In Figure 4-12(b) the SMF (km) as a function of p-FrFT parameter for different N is shown with symbol rate of $R = 28$ Gbaud. It is observed the increased length of SMF if the number of subcarriers is increased. The length of SMF depend on the symbol rate consider.

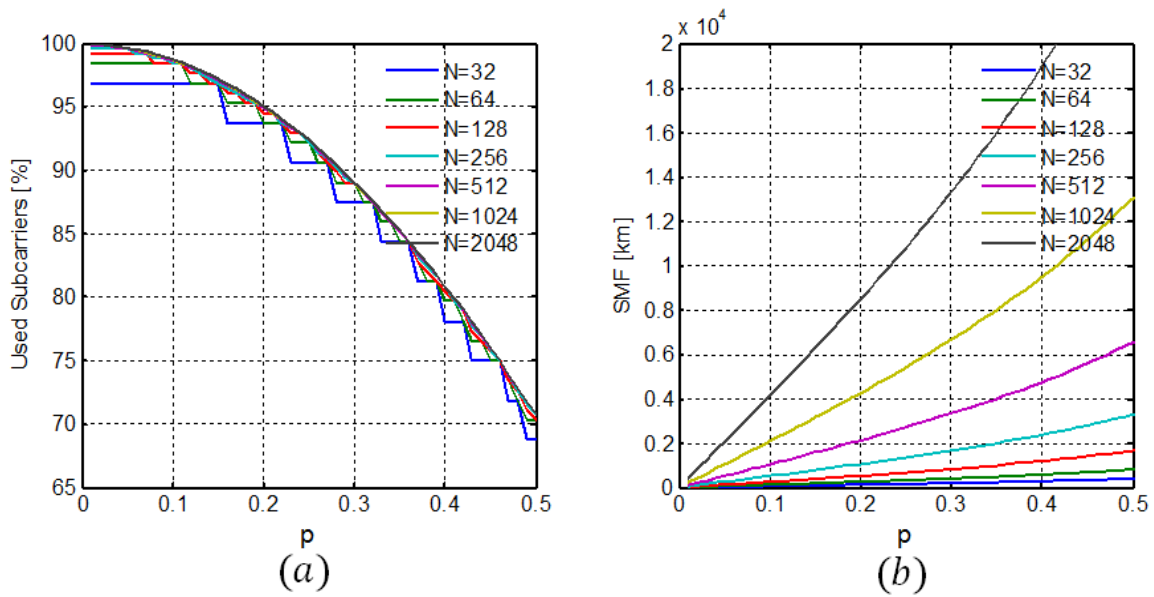


Figure 4-12: (a) Used subcarriers in percent, (b) SMF (Km) as a function of the p-FrFT parameter assuming different subcarrier number with symbol rate 28 Gbaud.

It is concluded that the relative useful subcarriers used expressed in percent does not change with the total number of subcarriers N transmitted. On the other hand if N increase the SMF length is increased. Simulation are needed to understand the performance of the proposed system due to the parameter trade-off.

A simulation is carry out with same transmitted symbol rate of $R = 28$ Gbaud, $N = 128$ and 4-QAM modulation to compare it with the theoretical formula in 4-23 varying p parameter. The simulation results are in very good agreement with the theory shown in Figure 4-13.

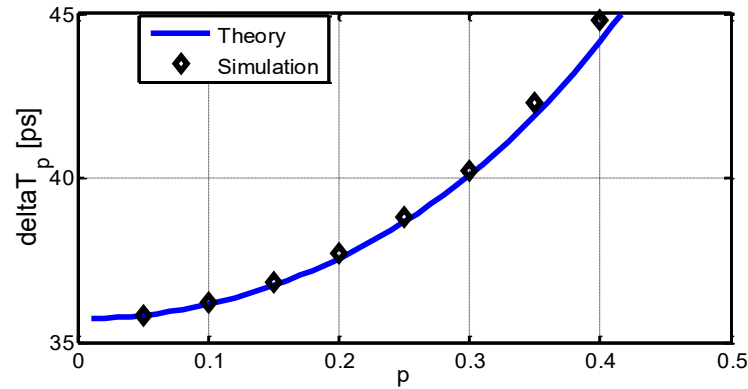


Figure 4-13: Received pulse repetition Δt [ps] as a function of p ; theoretical formula in blue line and simulation in black points for a symbol rate transmitted 28 [Gbaud].

The same parameters are used to evaluate the spectrogram of a single subcarrier before the SMF, shown in Figure 4-14(a), and after in Figure 4-14(b). It is observed the chirped behavior before the SMF and its compensation and pulse compression after the SMF.

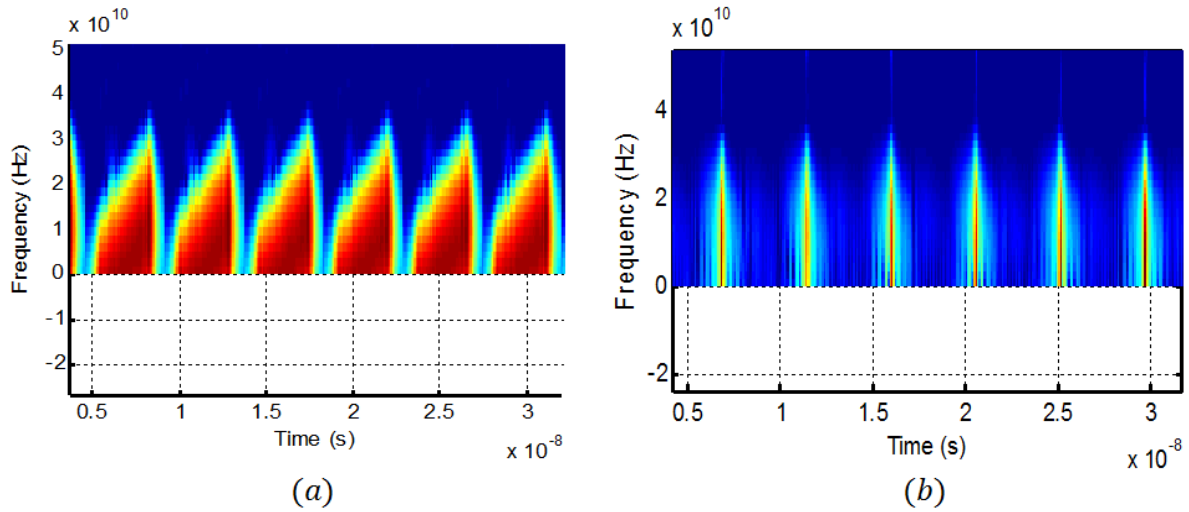


Figure 4-14: (a) Spectrogram of a single subcarrier 4-QAM modulated with 28 [Gbaud], $N = 128$, and $p = 0.1$ before the SMF fiber, (b) after the SMF.

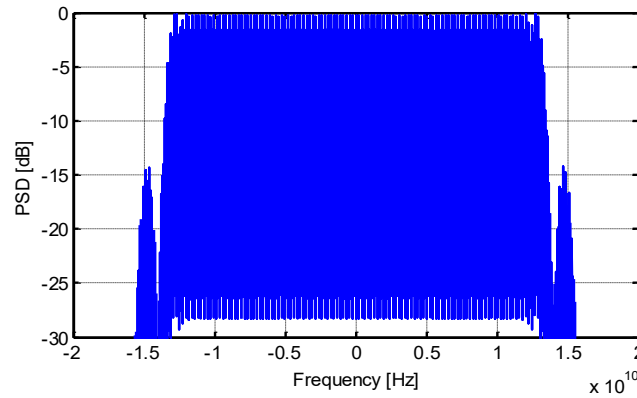


Figure 4-15: Power spectral distribution (PSD) [dB] of a single subcarrier.

The bandwidth of the subcarrier is also increased in frequency domain, as it can be observed also from the spectrogram above. In Figure 4-15 is shown the power spectral distribution (PSD) of a single subcarrier. Two small side lobes are observed at -15dB from the maximum. If total bandwidth of one subcarrier, consider at -15dB , is 26 GHz with subcarrier spacing equal to 34.2 MHz if $N = 128$, then the estimated total bandwidth occupied by $N_{used} = 128 * \cos\left(0.1 * \frac{\pi}{2}\right) \approx 126$ subcarriers is: $26\text{ GHz} + 26\text{ GHz} * \sin\left(0.1 * \frac{\pi}{2}\right) = 30\text{ GHz}$.

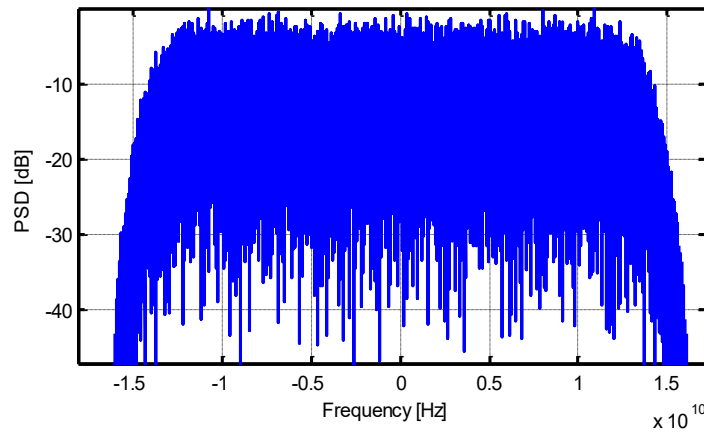


Figure 4-16: Power spectral distribution (PSD) [dB] of 126 subcarriers.

An increased of 7% to the total bandwidth of 28 GHz is found, as a drawback when using the proposed system. The total bandwidth of all subcarriers is shown in Figure 4-16 and confirm the simply estimation given above.

4.4.1 System performance

To evaluate the proposed system performance different symbol rate with different length of SMF are investigated with same setup as shown in Figure 4-8. The optical link is composed of N_s spans, each including a SMF of $L_{span} = 80 \text{ km}$ length and an erbium doped fiber amplifier (EDFA) with $NF = 6 \text{ dB}$ noise figure, whose gain completely recovers the span losses. The fiber attenuation is $\alpha = 0.2 \text{ dB/km}$, dispersion parameter $D = 17 \text{ ps/nm/km}$, dispersion slope $S = 0.07 \text{ ps/nm}^2/\text{km}$, non-linear parameter $1.3 \text{ (W}\cdot\text{km)}^{-1}$ and $PMD = 0.1 \text{ ps/(km)}^{1/2}$.

Additive white Gaussian noise (AWGN) is loaded at the RX, to simulate the amplified spontaneous emission (ASE) noise introduced by all the EDFAs in order to evaluate the BER versus the received OSNR defined in a reference optical bandwidth of 0.1 nm .

The phase noise is model as a Wiener process with zero mean and variance of the phase change $\sigma_\phi^2 = 2\pi\Delta\vartheta \cdot dt$, with $\Delta\vartheta$ being the laser linewidth, and dt the resolution time consider in the simulation [26]. Gaussian optical band pass filter with $2 \cdot R$ bandwidth is used after the noise loading. A five pole Bessel filter with $0.85 \cdot R$ bandwidth is used for Rx electronic limitations. ADC have a limit resolution of 6 bits.

The aim of the first algorithm is to equalize for PMD and time varying polarization rotation. For PM-QPSK/4-QAM modulation format the blind constant modulus algorithm (CMA) is used to estimate the inverse Jones matrix. This algorithm works only on the modulus of the received signal based on the fact that QPSK modulation have a constant power and was first introduce by Godard [27]. In standard DSP receiver a CD compensation module is required which also work with minimum 2 sample x symbol as CMA algorithm [28]. In FrFT based time lens there is no need for CD compensation as was explain in section 4.4, and saving power consumption. The CMA is followed by clock recovery [25] and carrier phase estimation. Carrier phase estimation is performed raising the symbol to the 4th power [24,29] to remove the modulation symbols. An

averaging over a block of symbols is used to reduce the AWGN noise. Blind phase search (BPS) proposed in [30] is also used for performance evaluation.

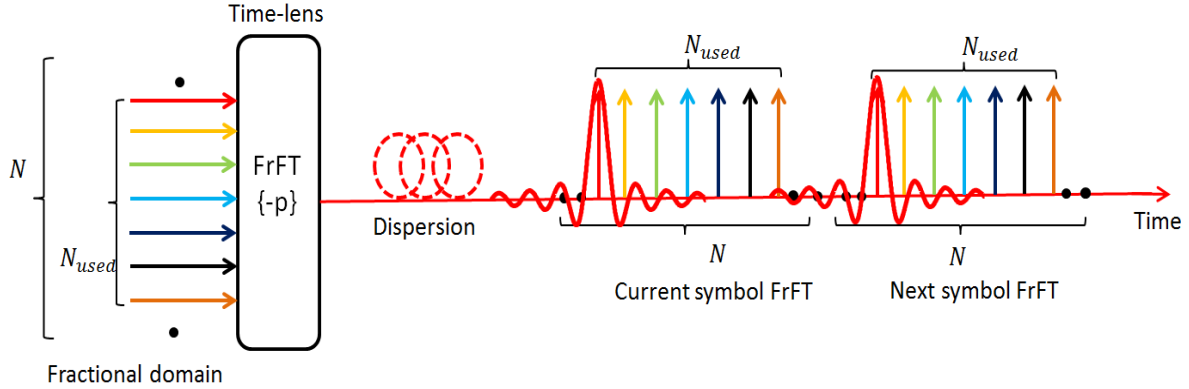


Figure 4-17: Schematic of FrFT based time lens to achieve frequency-to-time conversion. N is the total number of subcarriers or points of FrFT,

The idea behind this algorithm is to not remove the modulation but just try different angle constructed in one quadrant of signal constellation due to the rotational symmetry. This is also the major disadvantage of this algorithm and differential decoding is required to avoid cyclic slip. Also the computational complicity is increased. This algorithm was shown to approach the Cramer Rao limit [31]. This algorithm was originally proposed in [32]. Both algorithm are used for the proposed system in order to compare there performance. Last block of FrFT DSP is the data recovery where the error vector magnitude (EVM) is used for BER estimation to speed up the simulation time due to high number of subcarriers in the system.

In Figure 4-17, is shown the schematic of FrFT based on time-lens for frequency to time conversion. At the transmitter the total number of subcarriers is N where only N_{used} are filled with complex information, the other subcarriers are zero. They usually are called virtual subcarrier. After the transmission in SMF Nyquist optical pulse are received at Rx in time domain. Because no match filter exist for Nyquist pulse it is expected at least 2 dB of penalty from the theoretical curve. Same penalty as for non-return to zero (NRZ) pulse transmission.

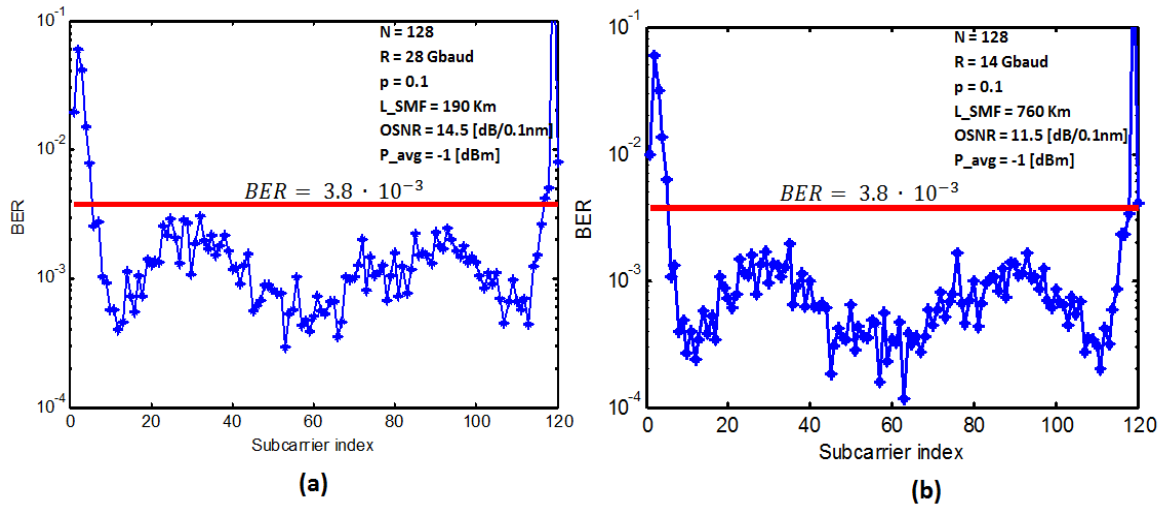


Figure 4-18: (a) BER versus the subcarrier index for $R = 28$ Gbaud, $p = 0.1$, $OSNR = 13.8$ dB, $P_{avg} = -1$ dBm, $N = 128$, and $L_{SMF} = 190$ km (b) $R = 14$ Gbaud, $OSNR = 11.5$ dB, $P_{avg} = -1$ dBm, $N = 128$, and $L_{SMF} = 760$ km. Total linewidth $\Delta\nu = 500$ kHz

To evaluate the performance of the proposed system, different scenarios are investigated first. At Tx a raised cosine filter with bandwidth equal to the symbol rate R is used for DAC bandwidth limitation. In Figure 4-18(a) BER versus the index subcarrier number is shown, with $p = 0.1$, $P_{avg} = -1$ dBm, $OSNR = 13.8$ dB and $R = 28$ Gbaud. Two span with length 80 km and one span of 20 km is used for a $L_{SMF} = 190$ km. The length is found by inverting 4-22. In Figure 4-18(b) the symbol rate is changed to $R = 14$ Gbaud, $OSNR = 11.5$ dB, $P_{avg} = -1$ dBm and $p = 0.1$. 9 spans with 80 km each is used with additional 40 km to have a total length of $L_{SMF} = 760$ km. Total laser linewidth is 500 kHz and window length of V&V equal to 32. 7 taps are used for fractionally spaced equalizer (FSE) blind CMA. The HD-FEC at $BER = 3.8 \cdot 10^{-3}$ is also shown as a reference. Manakov-PMD equation is used for short fiber simulation in order to speed up the time results, with the nonlinear terms reduced of a factor 8/9 [34]. From Figure 4-18 it is concluded that at least 10% of the edge subcarriers are not below the HD FEC limit, so it will be mandatory to have always more than 15% virtual subcarriers same in OFDM transmission. First target of the simulation is to evaluate the performance over 760 km with 28 Gbaud of symbol rate with different laser linewidth.

13 taps $\Delta t / 2$ spaced CMA is used for PMD compensation (Δt is given as in 4-23) and a window length of 16 is used for Viterbi & Viterbi algorithm phase noise estimation. 2^6 symbols are simulated for each subcarrier. The results are shown in Figure 4-19. In blue line it is shown the theoretical curve considering at Tx Gray coding.

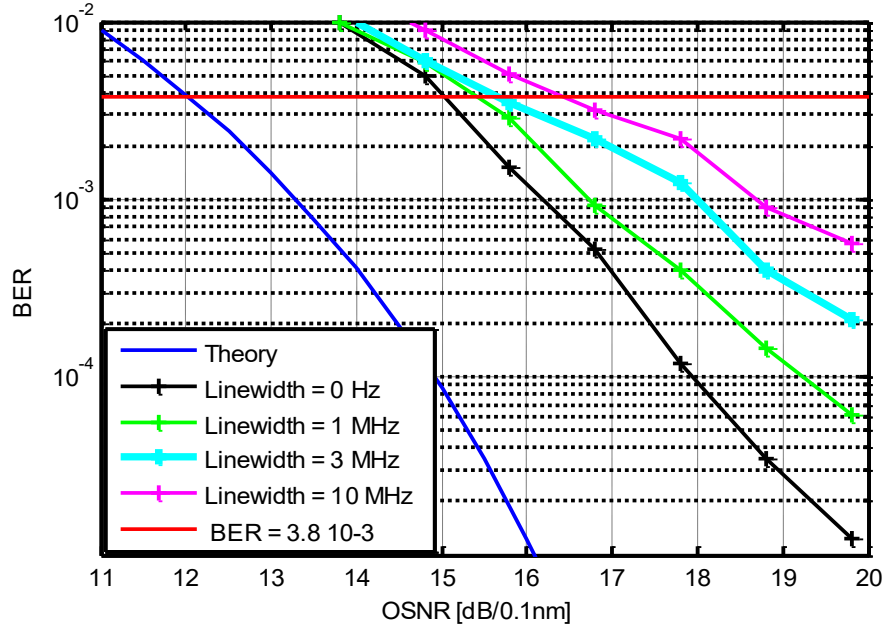


Figure 4-19: BER as a function of OSNR after 760 km of SMF with $R = 28$ Gbaud, $p = 0.1$ and $N = 512$ for different laser linewidth. In blue line is shown the theoretical curve.

The number of total subcarriers is $N = 512$, used subcarriers $N_{used} = 432$ and virtual subcarriers are 80. Parameter $p = 0.1$, in order to have 760 km of SMF. If the laser linewidth is zero the penalty from theoretical curve is approximately 3 dB for a $BER = 3.8 \cdot 10^{-3}$. When the linewidth increase to 1 MHz the penalty increase to 3.4 dB with a further increase to 3.7 if the linewidth increase to 3 MHz. In case of 10 MHz the penalty become 4.4 dB.

Figure 4-20 shows a comparison between V&V (blue line) and BPS (red line) of the required OSNR at a $BER = 3.8 \cdot 10^{-3}$ as a function of laser linewidth ($\Delta\theta$) times the duration of the symbol rate (Δt). For V&V the window length is $W = 16$ symbols and for BPS the resolution angle is $RA = 16$ with window length also $W = 32$. The performance in case of BPS are improved but with a higher cost in computational

complexity. For instance, with V&V we need $16 \cdot 8 = 128$ real multipliers and $4 \cdot 16 = 64$ real adders if it is assumed a 4th power of a complex number can be performed with 8 real multiplications and 4 adders. For BPS it is needed $32 \cdot 16 + 2 \cdot 32 \cdot 16 = 1536$ real multipliers and $2 \cdot 16 \cdot 32 - 32 + 3 = 995$ real adders. A trade-off between power penalty and computational complexity should be made for $\Delta\vartheta \cdot \Delta t / 2 > 3 \cdot 10^{-4}$. For $\Delta\vartheta \cdot \Delta t / 2 < 3 \cdot 10^{-4}$ V&V is by far more convenient.

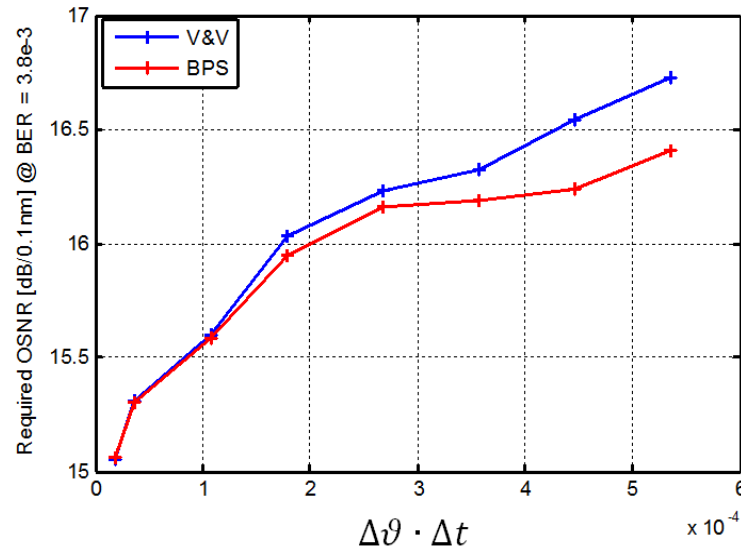


Figure 4-20: Required OSNR versus linewidth time symbol duration in case of V&V (blue line) and BPS (red line) algorithm are used.

In order to increase the transmission length, keeping $p \approx 0.1$ and $R = 28$ Gbaud, the total number of subcarriers N should increase as was shown in Figure 4-12(b). If the length of the fiber is $L_{SMF} = 1520$ km the number of subcarriers should be $N = 1024$, used subcarriers $N_{used} = 825$ and 199 are virtual subcarriers (20% of N). 2^5 symbols are simulated for each subcarrier. The link consists in 19 spans with each span 80 km. 5 channels spaced at 37 GHz are transmitted to account for all non-linear effects. A super Gaussian optical filter of 5 order and bandwidth $1.2 \cdot R$ is used to filter the center channel which shows the worst performance. 21 taps $\Delta t / 2$ spaced CMA is used for PMD compensation and a window length of 31 symbols is used for Viterbi & Viterbi algorithm. The results are shown in Figure 4-21. Three average power (P_{avg}) transmission per wavelength have been simulated. The performance are below the HD

FEC limit $3.8 \cdot 10^{-2}$ with an increase of 2.8 dB of power penalty in case of $P_{avg} = 2$ dBm due to the non-linear regime of operations.

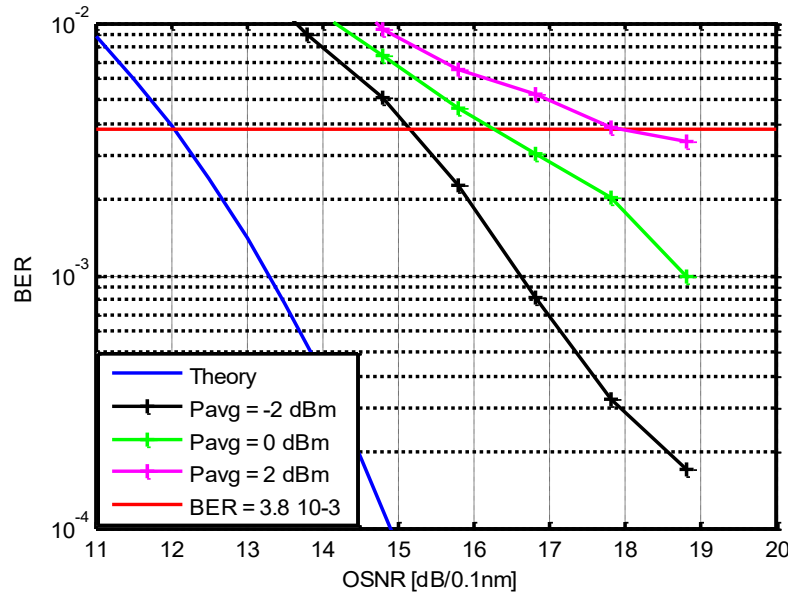


Figure 4-21: BER as a function of OSNR after 19span x 80 km = 1520 km fiber propagation with $R = 28$ Gbaud, $p = 0.1$ and $N = 1024$ for different average power transmission per wavelength (P_{avg}). In blue line is shown the theoretical curve..

In all the simulation performed a fixed length of SMF transmission was assumed. However in practice this length maybe not be fix. In Figure 4-22 are shown the results of a simulation with symbol rate $R = 56$ Gbaud, $N = 1024$, $N_{used} = 825$, $p = 0.1$, $\Delta\vartheta = 500$ kHz, $L_{SMF} = 380$ km. 13 taps $\Delta t/2$ spaced CMA and window length for V&V equal to 15 symbols. Δt is the new symbol rate (not the inverse of $1/R$) equal to $\Delta t = \frac{1}{\cos(0.1 \cdot \frac{\pi}{2}) * 56e9 \text{ GHz}} = 18.08$ ps. Blue is shown the theoretical curve; black line after 380 km fiber transmission with incident power equal to -2 dBm; green line after 382 km of SMF show an increased power penalty of 0.5 dB; cyan line after 385 km of SMF with performance not below the HD FEC. In this particular system configuration a tolerance of 2 km is supported with a power penalty of 0.5 dB.

In optical communications, the power consumptions arises from the ASIC module which account for more than 80% of the consumption in a

transceiver module. To allow reduction in power consumption, the size of the CMOS design must be reduced, too. Current ASIC is based on 40nm

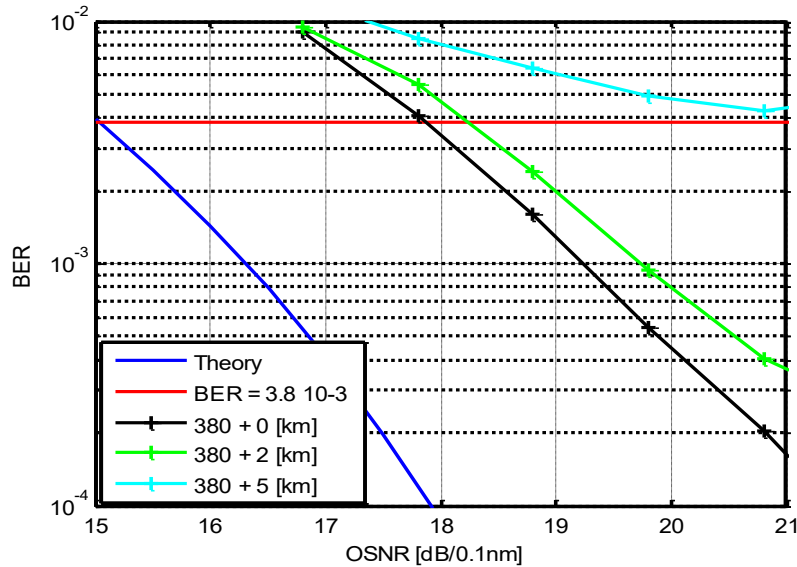


Figure 4-22: BER as a function of OSNR ; black line after 380km of SMF; green line after 382km and cyanine line after 385km.

CMOS technology [36], even though recently NTT announced that its second generation Low-Power DSP product, NLD0640 Gen2 LP-DSP, is available for manufacturers and ready for shipping [37].

This will reduce the power consumption of about 30% for 100G transmission solution. The power consumption is mainly originated by the DSP algorithm, which have the most significant weight, and in particular from the CD & PMD compensation algorithm.

Digital FrFT transmission is now compare to single/multicarrier carrier transmission (Square Root Raised Cosine /OFDM) in terms of CD & PMD power consumption based on the data given in [12] which consider a 40nm CMOS technology. The complexity of equalizers is determined by the number of taps, which is related to the bandwidth of the signal and to fiber length considered [38]. 28 Gbaud symbol rate is consider for a transmission length of 1520 km. To account for all order of PMD 9 taps can tolerate at least 22 ps of DGD if a 112 Gbit/s PM-QPSK modulation is consider [39]. The energy per bit consumption for CD compensation after 1520km transmission of SMF is

180pJ/bit as calculated in [35]. This leads to 18W power consumption for only CD compensation. For PMD the energy per bit is estimated approximately 100pJ/bit which result in 10W of power consumption. In digital FrFT there is no algorithm for CD compensation. OSNR penalty is higher in case of digital FrFT if compare to SRRC transmission. 3~3.5dB penalty was found in this section due to Nyquist optical waveform which has not a corresponding match filter to maximize the SNR. On the other hand SRRC has a match filter and the penalty after 1520km can is about 1.5~2dB which depend on the length of the filter. DSP cost depends on the size and power consumption. Here, if CD algorithm is not used it is estimated that the cost should go down of about one half in case of digital FrFT. Spectral efficiency for digital FrFT is decreased of 25% (20% are only virtual subcarriers and 5% the loss in symbol rate receiver) and for SRRC it is only decreased of 5%. In Figure 4-23 is shown the comparison between the two technology. The main drawback for digital FrFT is the fiber length which is fixed.

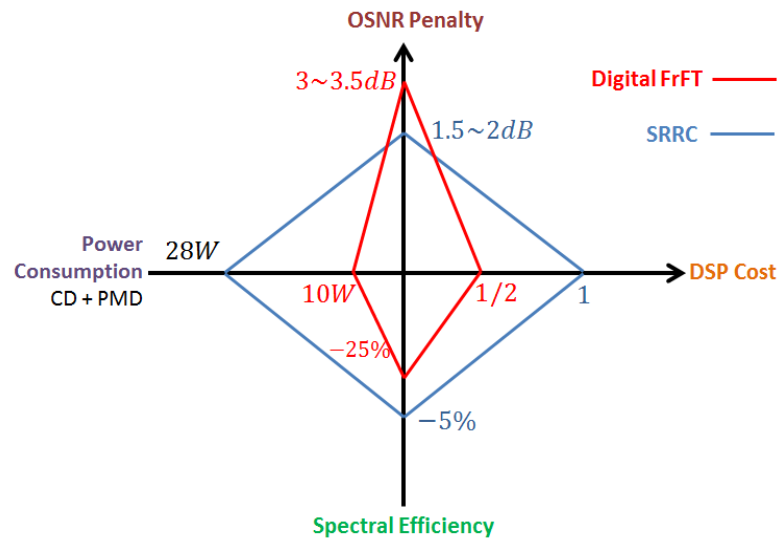


Figure 4-23: Comparison between digital FrFT (red line) and SRRC (blue line) single carrier transmission in terms of OSNR penalty, DSP cost, Spectral efficiency and Power consumption considering only CD&PMD.

4.5 Conclusions

A multicarrier transmission based on digital coherent FrFT is proposed for the first time in optical communications. The proposed transmission use the time lens effect and CD to convert a multicarrier signal to Nyquist OTDM signal at Rx side. It does not require cyclic prefix, a high number of preambles for channel estimation and pilot tone for phase noise estimation if compare to electrical OFDM. The main advantage is the reduced computational complexity at Rx side due to no CD compensation module. At Tx it has approximately equal complexity implementation as compare to electrical OFDM. The compressed optical time domain pulse obtained at Rx make the system more robust to phase noise due to local oscillator. The proposed FrFT take the best propriety from both traditional transmission but without the need for a CD compensation module.

This novel multicarrier transmission for optical communications is shown feasible for polarization multiplexing transmission with a high data rate confirmed by good performance results. Cost and power consumption are drastically reduced if compared to other system trasmission performance.

References

- [1] V. Namias, "The fractional order Fourier transform and its application in quantum mechanics," *J. Inst. Math. Appl.*, 25:241,265, 1980.
- [2] A. C. McBride and F. H. Kerr , "On Namias's Fractional Fourier Transforms," *IMA J. Appl. Math.* (1987) 39 (2): 159-175
- [3] H.M. Ozaktas, Z. Zalevsky, and M.A. Kutay. *The fractional Fourier transform*. Wiley, Chichester, 2001.
- [4] F. Gori, M. Santarsiero, and V. Bagini, " Fractional Fourier transform and Fresnel transform" *Atti Fondazione Giorgio Ronchi*.
- [5] L. B. Almeida, "The fractional Fourier transform and time-frequency representations," *IEEE Trans. Signal Processing*, vol. 42, pp. 3084–3091, Nov. 1994.
- [6] G. Cariolaro, T. Erseghe, P. Kraniuskauskas, and N. Laurenti. A untied framework for the fractional Fourier transform. *IEEE Trans. Sig. Proc.*, 46(12):3206{3212, 1998.
- [7] H.M. Ozaktas, Barshan B, Mendlovic D, Convolution, filtering, and multiplexing in fractional Fourier domains and their relationship to chirp and wavelet transforms. *J. Opt. Soc. Amer. A*, 1994, 11: 547—559
- [8] M. A. Kutay, H. M. Ozatakas, O. Arikan, and L. Onural, "Optimal filtering in fractional Fourier domains," *IEEE Trans. Signal Processing*, vol. 45, pp. 1129–1143, May 1997.
- [9] Adolf W. Lohmann, "Image rotation, Wigner rotation, and the fractional Fourier transform," *J. Opt. Soc. Am. A* 10, 2181-2186 (1993).
- [10] R. Schmogrow, M. Winter, M. Meyer, D. Hillerkuss, S. Wolf, B. Baeuerle, A. Ludwig, B. Nebendahl, S. Ben-Ezra, J. Meyer, M. Dreschmann, M. Huebner, J. Becker, C. Koos, W. Freude, and J. Leuthold, "Real-time Nyquist pulse generation beyond 100 Gbit/s and its relation to OFDM," *Opt. Express* 20, 317-337 (2012).
- [11] Crivelli, D.E.; Hueda, M.R.; Carrer, H.S.; del Barco, M.; Lopez, R.R.; Gianni, P.; Finochietto, J.; Swenson, N.; Voois, P.; Agazzi, O.E, "Architecture of a Single-Chip 50 Gb/s DP-QPSK/BPSK Transceiver With Electronic Dispersion Compensation for Coherent Optical Channels," in *Circuits and Systems I: Regular Papers, IEEE Transactions on* , vol.61, no.4, pp.1012-1025, April 2014
- [12] B. S. G. Pillai, B. Sedighi, K. Guan, N. P. Anthapadmanabhan, W. Shieh, K. J. Hinton, R. S. Tucker, "End-to-End Energy Modeling and Analysis of Long-Haul Coherent Transmission Systems," *J. Lightw. Technol.* 32 (18), 3093-3111 (2014).
- [13] P. Poggiolini, A. Carena, V. Curri, and F. Forghieri, "Evaluation of the computational effort for chromatic dispersion compensation in coherent optical PM-OFDM and PM-QAM systems," *Opt. Express* 17 (3), 1385-1403 (2009).
- [14] M. Martone, "A multicarrier system based on the fractional fourier transform for time-frequency-selective channels," *IEEE Trans. on Commmun.* 49(6) 1011-1020 (2001).
- [15] B.H. Kolner, "Space-time duality and the theory of temporal imaging,". *IEEE Journal of Quantum Electronics*, 30(8):1951–1963, 1994
- [16] G. Cincotti , S. Shimizu, T. Murakawa, T. Kodama, K. Hattori, M. Okuno, S. Mino, A. Himeno, T. Nagashima, M. Hasegawa, N. Wada, H. Uenohara, and T. Konishi, "Flexible power-efficient Nyquist-OTDM transmitter, using a WSS and time-lens effect," *Proc. OFC2015, W3C.5*.
- [17] G. Cincotti , "Enhanced Functionalities for AWGs" *J. Lightwave Technol.* 33(5), 998-1006, 2015.

- [18] N. Sambo, P. Castoldi, A. D'Errico, E. Riccardi, A. Pagano, M. S. Moreolo, J. M. Fabrega, D. Rafique, A. Napoli, S. Frigerio, E. H. Salas, G. Zervas, M. Nolle, J. K. Fischer, A. Lord, and J. P.-P. Gimenez, "Next generation sliceable bandwidth variable transponders," *IEEE Commun. Mag.*, vol. 53, no. 2, pp. 163–171, Feb. 2015.
- [19] S. C. Pei, M. H. Yeh, and T.-L. Luo, "Fractional Fourier series expansion for finite signals and dual extension to discrete-time fractional Fourier transform," *IEEE Trans. Signal Processing*, vol. 47, pp. 2883–2891, Oct. 1999.
- [20] S. A. Akhmanov, A. S. Chirkin, K. N. Drabovich, A. I. Kovrigin, R. V. Khokhlov, and A. P. Sukhorukov, "Non-stationary nonlinear optical effects and ultrashort light pulse formation," *IEEE J. Quantum Electron.* QE-4, 598–605 (1968).
- [21] José Azaña, Naum K. Berger, Boris Levit, and Baruch Fischer, "Spectral Fraunhofer regime: time-to-frequency conversion by the action of a single time lens on an optical pulse," *Appl. Opt.* 43, 483-490 (2004)
- [22] I. A. Walmsley and C. Dorrer, "Characterization of ultrashort electromagnetic pulses," *Adv. Opt. Photon.* 1, 308-437 (2009)
- [23] H. M. Ozatakas, B. Barshan, D. Mendlovic, and L. Onural, "Digital computation of the fractional Fourier transform," *IEEE Trans. Signal Processing*, vol. 44, pp. 2141–2150, Sept. 1996.
- [24] Savory, S.J., "Digital Coherent Optical Receivers: Algorithms and Subsystems," in *Selected Topics in Quantum Electronics, IEEE Journal of*, vol.16, no.5, pp.1164-1179, Sept.-Oct. 2010
- [25] Gardner, Floyd M., "A BPSK/QPSK Timing-Error Detector for Sampled Receivers," in *Communications, IEEE Transactions on*, vol.34, no.5, pp.423-429, May 1986.
- [26] G.J. Foschini and G. Vannucci. "Characterizing filtered light waves corrupted by phase noise," *IEEE Trans. Inf. Theory* 34(6), 1437-144 (1988).
- [27] D. N. Godard, "Self-recovering equalization and carrier tracking in two dimensional data communication systems," *IEEE Transactions on Communications*, vol. 28, no. 11, pp. 1867–1875, 1980.
- [28] G. Li, "Recent advances in coherent optical communication," *Advances in Optics and Photonics*, vol. 1, no. 2, pp. 279–307, 2009.
- [29] A. J. Viterbi and A. M. Viterbi, "Nonlinear estimation of PSK-modulated carrier phase with application to burst digital transmission," *IEEE Transactions on Information Theory*, vol. 29, no. 4, pp. 543–551, 1983.
- [30] T. Pfau et. al, "Hardware-Efficient Coherent Digital Receiver Concept With Feedforward Carrier Recovery for M-QAM Constellations," *J. of Lightwave Technol.*, vol. 27, no. 8, APRIL 15, 2009.
- [31] F. Rice, B. Cowley, B. Moran, and M. Rice, "Cramer-rao lower bounds for QAM phase and frequency estimation," *Communications, IEEE Transactions on*, vol. 49, no. 9, pp. 1582–1591, 2001.
- [32] S. K. Oh and S. Stapleton, "Blind phase recovery using finite alphabet properties in digital communications," *Electronics Letters*, vol. 33, no. 3, pp. 175–176, 1997.
- [33] Rene Schmogrow, Bernd Nebendahl, Marcus Winter, Arne Josten, David Hillerkuss, Swen Koenig, Joachim Meyer, Michael Dreschmann, Michael Huebner, Christian Koos, Juergen Becker, Wolfgang Freude, and Juerg Leuthold, "Error Vector Magnitude as a Performance Measure for Advanced Modulation Formats," *IEEE Photonics Technology Letters* 24, 61-63 (2012).

- [34] D. Marcuse, C. Manyuk, and P. Wai, "Application of the Manakov-PMD equation to studies of signal propagation in optical fibers with randomly varying birefringence," *J. Lightw. Technol.*, vol. 15, no. 9, pp. 1735–1746, Sep. 1997.
- [35] S. M. Bilal, G. Bosco, J. Cheng, A. P. T. Lau, and C. Lu, "Carrier Phase Estimation Through the Rotation Algorithm for 64-QAM Optical Systems," *J. Lightwave Technol.* 33, 1766-1773 (2015).
- [36] http://www.ntt-electronics.com/en/news/2012_02_29.html
- [37] <http://www.ntt-electronics.com/en/news/2015/3/20nm-low-power-coherent-dsp-shipping-in-volume.html>
- [38] B. Spinnler, "Equalizer design and complexity for digital coherent receivers," *IEEE J. Sel. Topics Quantum Electron.*, vol. 16, no. 5, pp. 1180–1192, Sep. 2010.
- [39] C. Xie, "Polarization-mode-dispersion impairments in 112-Gb/s PDMQPSK coherent systems," in *Proc. 36th Eur. Conf. Exhib. Opt. Commun.*, Sep. 2010, pp. 1–3, paper Th. 10. E. 6.

CHAPTER 5

CONCLUSION AND FUTURE WORK

In this chapter conclusion and future work are presented based on the results presented on this thesis.

5.1 Conclusions

Chapter 2

The use of adaptive DMT in access networks can fulfill the requirements of unbundling the local loop where different operator can transmit and receive on different assigned subcarrier. To lower the cost on the proposed DMT-PON a RSOA with 1.2GHz bandwidth is employed at the ONU side and in order to overcome the bandwidth limitation a Levin Campello algorithm is used.

Performance of the proposed DMT-PON was evaluated in up-stream scenario in case of a single wavelength and 16ONU over more than 45km of single mode fiber.

Chapter 3

AO-OFDM can run online at a high data rate maximizing the spectral efficiency with no need of DSP circuit. The IDFT/DFT filter can be integrated in a planar lightwave circuit which is mandatory for generation of high data rates superchannels, low power consumption and low cost production.

A WSS at the transmitter provide flexibility to AO-OFDM system. In AO-OFDM coherent detection it is not mandatory to compensate for CD before the demultiplexed, demonstrated both experimentally and by simulation.

In AO-OFDM there is no need for a DAC, fast adaptive filters for electrical OFDM demultiplexing and by using a frequency domain filter to compensate for CD there is no need for cyclic prefix/guard interval.

Experimental AO-OFDM results show that there is no need for an optical gating if a large bandwidth receiver is used.

The crosstalk performance of two optical filters for AO-OFDM demultiplexing were carefully investigated. The results show a better performance if AWG is used instead of a FBG.

Chapter 4

The novel multicarrier transmission based on digital FrFT reduces the DSP power consumption and receiver cost with no additional computational complexity added to the system if compared with traditional multicarrier transmission.

Polarization multiplexing doubles the spectral efficiency and common adaptive digital filters can mitigate the PMD effect as in single carrier traditional transmission.

Phase noise effects are relaxed due to short time domain sinc pulses received and no CP is used at the transmitter side.

5.2 Further work

Further areas for investigation are suggested as a result of the work carried out during this Ph.D.

WDM-PON is a promising approach for high speed access networks providing a high degree of flexibility. RSOA is one of the solutions to provide colorless ONU in a cost effective next generation PON. The modulation speed of RSOA depends on carrier lifetime and is limited to 10 Gbit/s. New generation of RSOA with shorter carrier lifetime would provide a larger 3 dB bandwidth and further numerical investigation will help to determine the physical RSOA parameter, e.g. active length, to be used for the next generation high speed access networks.

Regarding AO-OFDM, new experimental results are needed to evaluate higher order modulation formats with integrated optical IDFT/DFT Tx/Rx for a low power consumption. New experimental setup to validate the analytical formula for both direct and coherent detection schemes has never been done before and would be an interesting subject. Also,

implementation of low complexity DSP algorithm for ICI reduction would also be desirable.

To validate the simulation results regarding the novel multicarrier transmission based on digital FrFT for optical communications, experimental setup should be performed as this has never been performed before. Also, new DSP algorithm to reduce ISI&ICI should provide a lower OSNR penalty.

